“Charge self-consistency in an LDA+DMFT framework”

Dissertation

zur Erlangung des Doktorgrades
des Department Physik
der Universität Hamburg

vorgelegt von

Daniel Grieger

aus Göttingen

Hamburg

2013

Gutachter der Dissertation:	JProf. Dr. Frank Lechermann Prof. Dr. Michael Potthoff
Gutachter der Disputation:	JProf. Dr. Frank Lechermann Prof. Dr. Alexander Lichtenstein
Datum der Disputation:	16.01.2013
Vorsitzender des Prüfungsausschusses:	Dr. Alexander Chudnovskiy
Vorsitzender des Promotionsausschusses:	Prof. Dr. Peter Hauschildt
Dekan der Fakultät für Mathematik, Informatik und Naturwissenschaften:	Prof. Dr. Heinrich Graener

Kurzzusammenfassung

Gegenstand der vorliegenden Arbeit ist die Verbindung der Dichtefunktionaltheorie, speziell in ihrer lokalen-Dichte-Näherung (LDA), mit Methoden, die dazu dienen, explizit Vielteilcheneffekte zu beschreiben. Geeignete Methoden sind vorrangig die dynamische Molekularfeldtheorie (DMFT), für die ein Quanten-Monte-Carlo-Algorithmus zur numerischen Auswertung des einhergehenden Störstellenproblems verwendet wird, aber auch die rotationsinvariante Hilfsbosonen-Methode (RISB). Die Verbindung LDA+DMFT bzw. LDA+RISB der Methoden ist nichttrivial, da insbesondere Probleme bestehen, einen geeigneten korrelierten Unterraum aus der LDA-Rechnung zu extrahieren, sowie die Doppelzählung von Korrelationseffekten zu vermeiden. Das Hauptaugenmerk liegt jedoch auf der Ladungsselbstkonsistenz von LDA und DMFT, welche es erlaubt, die sich aus LDA und DMFT ergebenden Ladungsdichten zu einer selbstkonsistenten Ladungsdichte zu konvergieren. Auf diese Weise können die durch DMFT auftretenden Selbstenergieeffekte direkt auf die LDA-Rechnung und somit auf Bänder außerhalb des korrelierten Unterraums rückkoppeln. Besondere Bedeutung erhält dieser Formalismus ferner zur Berechnung von Gesamtenergien, welche zur Beurteilung von Phasenstabilitäten verwendet werden können. Konkret werden die dargestellten Methoden u. A. auf die Materialien Vanadiumsesquioxid (V_2O_3) und den Vergleich seiner paramagnetischen metallischen und isolierenden Phasen, sowie Bariumvanadiumtriselenid ($BaVSe_3$) und den Vergleich zu Bariumvanadiumtrisulfid ($BaVS_3$) angewendet.

Abstract

The subject of the work at hand is the combination of density functional theory, mainly in its local density approximation (LDA), with methods that describe many-particle effects explicitly. Suitable methods are in particular Dynamical Mean-Field Theory (DMFT), for which a quantum Monte-Carlo algorithm is used for the numerical evaluation of the impurity problem that is involved, and also the Rotationally Invariant Slave-Boson (RISB) technique. The combination LDA+DMFT or LDA+RISB, respectively, of the methods is nontrivial, notably, problems persist to extract a suitable correlated subspace from the LDA calculation, as well as to avoid double counting of correlation effects. However, the main focus is on the charge self-consistency of LDA and DMFT, which allows to converge the charge densities that emerge from LDA and DMFT to one self-consistently determined charge density. In this manner, self-energy effects that occur due to DMFT can directly couple back onto the LDA calculation and thus onto bands outside of the correlated subspace. Furthermore, this formalism obtains special importance for the calculation of total energies, which can be used for the estimation of phase stabilities. Concretely, the presented methods are applied, amongst others, to the material Vanadium sesquioxide (V_2O_3) and the comparison of its paramagnetic metallic and insulating phases, as well as to the material Barium Vanadium triselenide ($BaVSe_3$) and the comparison to Barium Vanadium trisulfide ($BaVS_3$).

Contents

One

Introduction

$$\hat{H}|\,\Psi\rangle = |\,\Psi\rangle E \tag{1.1}$$

This equation (the stationary Schrödinger equation, of course), as simple as it might look, is probably one of the most important equations in physics, or at least the most important equation in the description of the electronic properties of matter. Sure, there is an enormous zoo of phenomena that the Schrödinger equation does not describe properly. Anyway, the complexity of this simple-looking equation is revealed by looking at the Hamilton operator $\hat{H}$ of the standard model of solid state physics, which is a system consisting of M nuclei at positions $\underline{R}_\mu$ with masses M_μ and charges $Z_\mu \cdot e$ and of N electrons at positions $\underline{r}_\nu$ with masses m_e:

$$\begin{aligned}
\hat{H} &= \sum_{\mu=1}^{M} \frac{-\hbar^2}{2M_\mu} \underline{\nabla}_{\underline{R}_\mu}^2 + \sum_{\nu=1}^{N} \frac{-\hbar^2}{2m_\mathrm{e}} \underline{\nabla}_{\underline{r}_\nu}^2 \\
&+ \frac{1}{2} \sum_{\mu \neq \mu'}^{M} \frac{e^2 Z_\mu Z'_\mu}{4\pi\epsilon_0 |\underline{R}_\mu - \underline{R}_{\mu'}|} - \sum_{\nu=1}^{N} \sum_{\mu=1}^{M} \frac{e^2 Z_\mu}{4\pi\epsilon_0 |\underline{r}_\nu - \underline{R}_\mu|} \\
&+ \frac{1}{2} \sum_{\nu \neq \nu'}^{N} \frac{e^2}{4\pi\epsilon_0 |\underline{r}_\nu - \underline{r}_{\nu'}|}
\end{aligned} \tag{1.2}$$

And by judging the complexity of this problem, one still has to keep

in mind that it is supposed to describe an entire solid state body, which means that the numbers N and M of electrons and nuclei are in the order of magnitude of 10^{23}. And solving partial differential equations for such a number of variables is obviously hopeless. But even if one would limit oneself to molecules (to begin with), the many-particle wave function Ψ that is supposed to be calculated depends on typically at least 10 electronic coordinates. So to save this function on a computer, for instance if one changes the position of one of this electrons, one would have to store all the information how the other 9 electrons react. This leads to an exponentially increasing memory need which, as can easily be demonstrated, can not be handled even for small molecules. Presumably, in a few hundred years or so, a technology will exist that is able to solve all the above problems. But up to then, one definitely needs simplifications and approximations.

So what can be done to simplify the problem? In all sorts of electronic structure calculations, the first step is the approximation by Born and Oppenheimer [BO27], which allows to treat the kinetic energy of the cores individually, so that the resulting wave function for the electrons depends on the core positions only parametrically. However, the wave function still depends on all N electronic coordinates, so computational handling thereof is still impossible.

One approach to solve this problem is density functional theory (DFT), formulated by Hohenberg and Kohn in 1964 [HK64]. As described in section 2.1, this theory proves that all physical properties of a system of interacting electrons, especially its ground state energy, are functionals of the electron density only. The electron density is a function of real space position only and can therefore easily be saved on a computer. According to Kohn and Sham [KS65], the electron density can be obtained by solving effective one-electron Schrödinger equations for the electrons in the unit cell of a crystal (making use of Bloch's theorem), which reduces the problem size dramatically. But the largest problem of this theory is hidden in the innocent-looking word "effective". It is not known exactly how this effective potential for the one-particle Schrödinger equations looks like. Anyway, suc-

cessful approximations exist. There is only a small class of materials for which these fail.

One could now relax and be happy about this great solution. But of course physicists would not be physicists if they stopped working at this problem as long as this "small class" exists. And this "small class" is the main subject of the work at hand. Anyway, it shall not be underestimated that already "standard" density functional theory is a vivid and fruitful area of research.

So how can one tackle this "small class" of strongly correlated electron systems? The most intuitive way is probably to improve the approximations for the effective potential, which is still a vivid area of research. However, in this work, a totally different route is followed, which partially goes back to the original equation (1.1) (still in the Born-Oppenheimer approximation). Trying to solve it directly is still hopeless, but limiting oneself to the description of only few physically relevant electrons near the Fermi level (in the applications presented herein, "few" ranges from one to, at maximum, five orbitals, each occupied by up to two electrons) and finding suitable assumptions and parametrisations of the parameters that occur in the Hamilton operator (1.2), the problem gets a model-like character, which can well be expressed by the Hubbard model presented in section 2.2. In brief, the Hubbard model is a lattice model in which an electron can "hop" from one lattice site to the next, each time gaining a small amount t of energy. However, if the joyfully hopping electron arrives at the next lattice site, it might meet another electron there. Since electrons are extremely antisocial by nature, this will "cost" an energy U. So the interplay of the model parameters t and U can be understood as the most basic ingredient characterising this model, which is surprisingly successful and able to capture many different physical effects in spite of its simplicity.

Although no exact or analytic solution of the Hubbard model can be found in general, some very succesful and accurate approximative methods exist, from which, just to name them once, the very accurate but computationally demanding dynamical mean-field the-

ory (DMFT) with a hybridisation-expansion continuous-time quantum Monte Carlo (CTQMC) impurity solver (see section 2.2.1) and the faster rotationally invariant slave-boson technique (RISB, see section 2.2.2) are important for the present work. They all have in common that they are computationally demanding and thus, as mentioned, limited to, at maximum, five orbitals. However, they have proven to give reliable results and can account for virtually all effects of strong electronic correlations that the Hubbard model can describe.

So the question arises how the Hubbard model can help to improve the effective potentials of the approximations to DFT. The original idea, that has also proven to be quite successful, is to do first a DFT calculation (in a suitable approximation), and then take out a small set of one-particle bands from this calculation that are typically near the Fermi energy and thus most important for the physics of the system. Their dispersion relations are taken to build a suitable Hubbard model (more precisely the now $\underline{k}$-dependent model parameter $t(\underline{k})$) that is "solved" (with one of the methods named above) to take into account all electronic correlations in this subspace explicitly. Several of these quite sophisticated interfacing techniques exist and those who are important for this work are summarised in section 2.3.

A demonstration of the success of this combination of density functional theory in its local density approximation (LDA) and DMFT (LDA+DMFT in short) as well as RISB (LDA+RISB) is the starting point for the work at hand. For this purpose, the overall surprisingly similar Vanadium chalcogenide compounds $BaVS_3$ and $BaVSe_3$ are compared. Despite their similarity, their low-temperature phases are significantly different, notably an insulating charge-density wave ordering is observed in the sulfide compound, but no traces thereof have been found in the selenide compound. Since such an ordering is a clear sign of strong electronic correlations, the comparison of these compounds is a well-suited problem for LDA+DMFT and LDA+RISB and is presented in chapter 3.

However, one immediately gets aware of at least one problem of this approach: The two formalisms are applied in a purely consecutive

manner, or, how it will be called from here on, DMFT is used as a post-processing tool for LDA. This means that most output quantities of the two formalisms are almost independent of each other, for instance the charge density that one could calculate from the DMFT solution is not related to the charge density that has been mentioned as the basic quantity of DFT. In other words, the effects of strong electronic correlations onto most of the DFT output quantities are not taken into account. This is where the main part of the new developments presented in this work comes into play: The charge self-consistency (CSC) is, in brief, constructed in a way that the output charge density of DMFT is inserted back into the effective potentials of DFT, so that a large self-consistency cycle arises. The formal and technical developments that are required and have been done for this combination, together with some small sample applications, are described in chapter 4.

One of the main advantages of the charge self-consistency is the possibility to calculate total energies in the formalism: Although the total energy is a very natural output quantity of normal DFT, the usual LDA+DMFT post-processing schemes have no direct access (or at least only very approximate access) to it. However, with the more direct combination of LDA and DMFT due to CSC, the calculation of total energies can easily be motivated. A detailed study in which the advantages of this total energy calculation show up is documented in the final chapter 5 of this work. It deals with the prototypical strongly correlated electron compound V_2O_3. Calculating total energies, it is immediately possible to judge whether the paramagnetic metallic or the Mott insulating phase of V_2O_3 is stable at the temperature and pressure in question. This means that the calculation and mapping of entire phase diagrams of strongly correlated compounds becomes feasible.

Two

Basics

The following chapter is supposed to show some well-known methods concerning electron structure calculations and beyond, especially for strongly correlated electronic systems. None of these methods is new, but they form the basis of the developments shown hereafter and therefore provide an introduction to what is shown in the following. The starting point is density functional theory, which is the basis not only of this field, but of a very large part of contemporary electron structure calculations of realistic materials. The success thereof and even its enormous predictive power has been proven in numerous studies during the last decades.

2.1 Density functional theory

As mentioned in the introduction, the solution of the many-particle Schrödinger equation (1.1) with the Hamilton operator (1.2), applying the Born-Oppenheimer approximation which allows to seperate the core coordinates, reveals at least one big problem: The many-particle wave function $|\Psi\rangle$ that solves the Schrödinger equation depends on all electronic coordinates $\underline{r}_i$ (and of the electronic spin, which shall not be mentioned explicitely here). So for large systems, it will become impossible to deal with this quantity. A different function is therefore

needed, which depends on far less variables, but still allows to find the ground state energy E as accurately as possible.

An answer to this problem is given by density functional theory (DFT), introduced by Hohenberg and Kohn [HK64], which is briefly presented in the following section, basically in line with [PY89]. DFT states that the ground state electron density $n(\underline{r})$ uniquely determines the properties of the electronic ground state, particularly the ground state energy. The electron density $n(\underline{r})$ is related to the many particle wave function $\Psi(\underline{r}_1, \ldots, \underline{r}_N)$ by simple quadrature:

$$n(\underline{r}) = N \cdot \int \mathrm{d}^3 r_2 \cdots \int \mathrm{d}^3 r_N \, |\Psi(\underline{r}_1, \ldots, \underline{r}_N)|^2 \tag{2.1}$$

This implies that the electron density contains less information than the wave function, as phase information is deleted by the quadrature. The reason why the electron density is still sufficient to contain all ground state properties is given by the proof of Levy, which is sketched in the following section.

2.1.1 Levy constrained search formulation

According to (2.1), the electron density is uniquely specified by the wave function. However, the opposite way is not unique, arbitrarily many wave functions exist that all give the same electron density. So let $n(\underline{r})$ be the true ground state electron density of some many-electron system, $|\Psi\rangle$ be the true ground state wave function and $|\Psi'\rangle$ be a trial wave function that gives the same electron density. The variational principle states that the Hamilton operator expectation value of any trial wave function is larger than the one of the ground state wave function:

$$\langle \Psi' | \hat{H} | \Psi' \rangle \geq \langle \Psi | \hat{H} | \Psi \rangle = E \tag{2.2}$$

The Hamilton operator $\hat{H}$ of the Born-Oppenheimer approximation (without the kinetic energy of the nuclei) can be split, up to a constant,

as follows:

$$\hat{H} = \hat{T} + \hat{V}_{\mathrm{ee}} + \sum_{i=1}^{N} v(\underline{r}_i) \tag{2.3}$$

Here, $\hat{T}$ stands for the kinetic energy of the electrons, $\hat{V}_{\mathrm{ee}}$ for the electron-electron interaction and $v(\underline{r}_i)$ for the interaction of an electron and a nucleus. Since the latter is the same for $|\,\Psi\rangle$ and $|\,\Psi'\rangle$ giving the same electron density, (2.2) can be rewritten as follows:

$$\langle\,\Psi'|\hat{T} + \hat{V}_{\mathrm{ee}}|\,\Psi'\rangle \;\geq\; \langle\,\Psi|\hat{T} + \hat{V}_{\mathrm{ee}}|\,\Psi\rangle \tag{2.4}$$

This means that the ground state energy E can be obtained by minimizing the above expression over all normalised wave functions that give the correct electron density $n(\underline{r})$. For this purpose, the following functional is introduced:

$$F[n] := \min_{\Psi \to n} \langle\,\Psi|\hat{T} + \hat{V}_{\mathrm{ee}}|\,\Psi\rangle \tag{2.5}$$

The functional $F[n]$ is called universal density functional. It provides an extremely simple representation of the ground state energy which only depends on the ground state electron density:

$$E[n] = F[n] + \int \mathrm{d}^3 r\, v(\underline{r}) n(\underline{r}) \tag{2.6}$$

This is already the desired result. As the ground state electron density is normally not known in advance, the ground state energy E can be found by a two-step process: First, mimimize the above expression at a given trial density, then minimize the result over all trial densities with the constraint that the number of particles (the integral over the electron density) is N:

$$\begin{aligned} E \;=\; \min_{n} \Bigg[& \min_{\Psi \to n} \left(\langle\,\Psi|\hat{T} + \hat{V}_{\mathrm{ee}}|\,\Psi\rangle \right) + \int \mathrm{d}^3 r\, v(\underline{r}) n(\underline{r}) \\ & - \mu \left(\int \mathrm{d}^3 r\, n(\underline{r}) - N \right) \Bigg] \end{aligned} \tag{2.7}$$

The Lagrange multiplier μ is the chemical potential. The above procedure is called Levy constrained search.

2.1.2 The Kohn-Sham method

Although the Levy constrained search gives a surprisingly simple justification of density functional theory, it is not useful for the practical calculation of electron densities and ground state energies. For this purpose, the so-called Kohn-Sham method has been proven to be profitable. This method goes away from the description by the density only, but uses one-particle wave functions $|\psi_\nu\rangle$ that are eigenstates of a system of non-interacting electrons. The N-electron ground state wave function is then represented by a Slater-determinant $|\,\Psi_\mathrm{S}\rangle$ which gives the same electron density:

$$|\,\Psi_\mathrm{S}\rangle = \frac{1}{\sqrt{N!}}\det\left[|\psi_1\rangle|\psi_2\rangle\ldots|\psi_N\rangle\right] \tag{2.8}$$

So the electron density $n(\underline{r})$ is given as follows:

$$n(\underline{r}) = \sum_{\nu=1}^{N} |\psi_\nu(\underline{r})|^2 \tag{2.9}$$

The kinetic energy $T_\mathrm{S}[n]$ of a Slater determinant can be expressed as follows:

$$T_\mathrm{S}[n] = \langle\,\Psi_\mathrm{S}|\sum_{\nu=1}^{N}\frac{\hat{p}_\nu^2}{2m}|\,\Psi_\mathrm{S}\rangle = \sum_{\nu=1}^{N}\langle\psi_\nu|\frac{\hat{p}^2}{2m}|\psi_\nu\rangle \tag{2.10}$$

$\hat{p}_\nu$ are the one-particle momentum operators, $\hat{p}_\nu = \frac{\hbar}{i}\underline{\nabla}$ in real space representation. Note that this relation is only valid if the one particle wave functions $|\psi_\nu\rangle$ are orthonormal. The universal density functional is rewritten as follows:

$$F[n] = T_\mathrm{S}[n] + E_\mathrm{H}[n] + E_\mathrm{XC}[n] \tag{2.11}$$

In this equation, $E_\mathrm{H}[n]$ is the Hartree energy defined as follows:

$$E_\mathrm{H}[n] := \frac{1}{2}\int \mathrm{d}^3r_1 \int \mathrm{d}^3r_2\, \frac{e^2 n(\underline{r}_1)n(\underline{r}_2)}{4\pi\epsilon_0|\underline{r}_1 - \underline{r}_2|} \tag{2.12}$$

The last term, the exchange-correlation energy $E_{\mathrm{XC}}[n]$, is defined as the difference between the true universal density functional and the above sum. It collects the correction of the kinetic energy that occurs because the ground state energy in general cannot be expressed exactly as a Slater determinant, as well as the part of the electron-electron interaction that is not described by the Hartree energy, which gives the classical electrostatic interaction of N electrons with N other electrons. In principle, this partition is arbitrary, already the original publication [KS65] mentions that it is done "for convenience", but has proven to be useful and feasible.

The ground state energy, given by (2.6), is again minimized according to the variational principle. Additionally, a constraint has to be added that ensures that the one-particle wave functions $|\psi_\nu\rangle$ are orthogonal. So the variation leads to a Schrödinger equation for each one-particle wave function that has to be solved in an effective potential $v_{\mathrm{eff}}(\underline{r})$:

$$\left(-\frac{\hbar^2}{2m}\underline{\nabla}^2 + v_{\mathrm{eff}}(\underline{r})\right)\psi_\nu(\underline{r}) = \epsilon_\nu\psi_\nu(\underline{r}) \tag{2.13}$$

The effective potential $v_{\mathrm{eff}}(\underline{r})$ is given as follows:

$$v_{\mathrm{eff}}(\underline{r}) := v(\underline{r}) + \int \mathrm{d}^3r' \frac{e^2 n(\underline{r}')}{4\pi\epsilon_0|\underline{r}-\underline{r}'|} + \mu_{\mathrm{XC}}(\underline{r}) \tag{2.14}$$

It consists of three terms, resulting from the variation of the external potential $v(\underline{r})$, of the Hartree energy $E_{\mathrm{H}}[n]$ and of the exchange-correlation energy $E_{\mathrm{XC}}[n]$; the so-called exchange-correlation potential $\mu_{\mathrm{XC}}(\underline{r})$ is therefore defined as follows:

$$\mu_{\mathrm{XC}}(\underline{r}) := \frac{\delta E_{\mathrm{XC}}[n]}{\delta n(\underline{r})} \tag{2.15}$$

The equations (2.13) and (2.14) are the Kohn-Sham equations. Since the Kohn-Sham potential depends explicitly on the electron density (which is in principle the final output quantity of the formalism), they

have to be solved in a self-consistent cycle: One starts with an arbitrary input density $n_{\mathrm{in}}(\underline{r})$ (typically a linear combination of atomic charge densities), builds an effective potential according to equation (2.14) and solves equation (2.13) in this potential. This results in eigenfunctions that can be used to create an output density $n_{\mathrm{out}}(\underline{r})$. Applying a suitable minimisation (or mixing) procedure, e. g. Broyden's method [Bro65], a new $n_{\mathrm{in}}(\underline{r})$ is built and inserted into the beginning. The cycle is iterated until convergence, i. e. until, up to numerical accuracy, a fixed point of the cycle is reached.

It shall further be mentioned that the above derivations are written in the spirit of calculations for isolated atoms or molecules. Solid state bodies can be described as periodic crystals for which the one-particle wave function formulation allows for a very simple theory applying Bloch's theorem. In brief, this leads to Kohn-Sham Hamilton operators and one-particle wave functions having an additional $\underline{k}$-dependence ($\underline{k}$ being a wave vector from the first Brillouin zone of the crystal), which will be written explicitly from here on. Furthermore, all basic quantities, including the electron density, are related to one unit cell.

2.1.3 Exchange-correlation functionals

Density functional theory is, in principle, an exact theory. However, an exact expression of the exchange-correlation functional $E_{\mathrm{XC}}[n]$ and likewise of the potential $\mu_{\mathrm{XC}}(\underline{r})$ is generally unknown, as it is not given by the above derivation. In practice, approximations of the functional exist. A short overview of existing approximations, especially of those used in this work, is given in this section. It is intrinsically not possible to judge which of them is the "best" approximation. However, an attempt shall be made to find an ascending order of the "level of sophistication" of the methods, which, of course, does not guarantee an ascending quality of the results, even the simplest approximations can give reasonable answers (and sometimes even better answers than the more sophisticated ones).

- The Local Density Approximation (LDA) treats the functional as depending on the (local) electron density functional value for each real-space coordinate only, which means that the functional is cast into the following form:

$$E_{\mathrm{XC}}^{\mathrm{LDA}}[n] = \int \mathrm{d}^3 r \, \epsilon_{\mathrm{XC}}^{\mathrm{LDA}} \left(n(\underline{r}) \right) \cdot n(\underline{r}) \tag{2.16}$$

  In order to find an approximate expression for the function $\epsilon_{\mathrm{XC}}^{\mathrm{LDA}}$ (note that this is a simple function, not a functional), Quantum Monte Carlo data calculated by Ceperley and Alder [CA80] for the homogeneous interacting electron gas can be used. Parametrisations of this data have been done e. g. by Perdew and Zunger [PZ81], or, most important for this work, by Perdew and Wang [PW92].

- The procedure can be generalised to the Local Spin Density Approximation (LSDA), in which the functional retrieves an additional dependence on the magnetic charge density $n^{\uparrow}(\underline{r}) - n^{\downarrow}(\underline{r})$, where $\uparrow$ and $\downarrow$ indicate spin channels. This allows for magnetic solutions. Even the non-collinear LSDA is possible, in which not only the magnitude of spins, but also their "direction", can be calculated.

- The Generalised Gradient Approximation (GGA) includes the dependence on the gradient of the electron density:

$$E_{\mathrm{XC}}^{\mathrm{GGA}}[n] = \int \mathrm{d}^3 r \, \epsilon_{\mathrm{XC}}^{\mathrm{GGA}} \left(n(\underline{r}), \underline{\nabla} n(\underline{r}) \right) \cdot n(\underline{r}) \tag{2.17}$$

  The determination of $\epsilon_{\mathrm{XC}}^{\mathrm{GGA}}$ is in line with $\epsilon_{\mathrm{XC}}^{\mathrm{LDA}}$ as mentioned above, as well as its generalisation to magnetic formulations. A typical parametrisation has been done by Perdew, Burke and Ernzerhof [PBE96].

- The next step could be to include higher derivatives of $n(\underline{r})$ in the approximation, which leads to so-called meta-GGA func-

tionals. However, this approach is currently not of high practical relevance.

- Among the most promising, so-called hybrid functionals can be named, for example the B3LYP functional for the exchange energy given by Becke [Bec93]:

$$\begin{aligned} E_{\mathrm{X}}^{\mathrm{B3LYP}}[n] &= E_{\mathrm{X}}^{\mathrm{LSDA}}[n] \\ &+ 0.2\left(E_{\mathrm{X}}^{\mathrm{Fock}}[n] - E_{\mathrm{X}}^{\mathrm{LSDA}}[n]\right) + 0.72\Delta E_{\mathrm{X}}^{\mathrm{GGA}}[n] \end{aligned} \tag{2.18}$$

  In this equation, $E_{\mathrm{X}}^{\mathrm{Fock}}[n]$ is the exchange term given by the Hartree-Fock method (the "Fock" term). This illustrates the general nature of hybrid functionals, combining the Hartree-Fock method and the above-mentioned functionals. The prefactors are determined by empirical considerations, which in a way makes the method lose its full "ab-initio" character.

- Finally, the LDA+U (or GGA+U) method can be named. It is closely related to the methods presented in the following sections. Briefly, an additional parameter U is used, which mimics explicit electron-electron interaction in a static mean-field limit.

Which of the methods should be chosen is of course a matter of mainly physical intuition. As a general rule of thumb, systems for which a homogeneous electron gas is a good approximation (e.g. Aluminium) are described (few surprisingly) very well via the electron gas related approximations, whereas problems occur mainly for strongly localised systems, also including e.g. small molecules. However, this question shall not be of central interest for the rest of this work, since correlation effects beyond the simple approximations to the density functional shall be treated by the following more explicit methods.

2.1.4 Basis sets for Kohn-Sham wave functions

The (Bloch) Kohn-Sham wave functions $\psi_{\underline{k}\nu}(\underline{r})$ are subject to an essentially technical issue: If they are saved on a computer, a suitable

discretisation thereof has to be used, which is done by establishing a suitable finite basis set for these wave functions. The most natural choice would be plane waves with lattice vectors $\underline{G}$ commensurate to the original lattice of atoms:

$$\psi_{\underline{k}\nu}(\underline{r}) = \sum_{\underline{G}} \psi_{\underline{G}}^{\underline{k}\nu} \frac{1}{\sqrt{\Omega_c}} \mathrm{e}^{\mathrm{i}(\underline{k}+\underline{G})\underline{r}} \tag{2.19}$$

The vectors $\underline{G}$ thus correspond to points of the reciprocal lattice and Ω_C normalises each plane wave to the unit cell volume. This basis is made finite by restricting the set of vectors $\underline{G}$ to those with a kinetic energy smaller than a "plane-wave cutoff energy" E_{pw}:

$$\frac{\hbar^2}{2m_{\mathrm{e}}} \|\underline{k} + \underline{G}\|^2 \leq E_{\mathrm{pw}} \tag{2.20}$$

The severe disadvantage of this simple approach shows up in the structure of the Kohn-Sham wave functions: In the so-called interstitial region away from the nuclei, they can in general be approximated sufficiently well by plane waves, so that E_{pw} can be reasonably small. However, near the nuclei, the wave functions have a complex nodal structure, which can be attributed to the orthogonalisation to the "core" wave functions with smaller principal quantum number. Thus, they are difficult to be resolved by plane waves only, so that E_{pw} would adapt large values that are difficult to be handled numerically.

One simplification worth mentioning in this context is the "frozen-core" approximation which treats core electrons (typically all but those with the largest principal quantum number per angular momentum channel) as fixed ("frozen"), so that they are not included in the calculation explicitly. The main advantages of this approximation are a significant reduction of the problem size and thus the required calculation time and a decrease of the value of the total energy by (up to) orders of magnitudes, which reduces the demands for the required accuracy in order to calculate energy differences in a numerically stable way.

The following section tries to give a short overview of two possible approaches, important for the work at hand, to solve the cutoff energy problem as well as to incorporate the frozen-core approximation into DFT calculations.

The projector-augmented wave (PAW) method

The projector-augmented wave (PAW) method [Blö94] replaces the (true or "all-electron") wave functions $|\psi\rangle$ (indeces are dropped for readability for the moment) by auxiliary or "pseudo" wave functions $|\tilde{\psi}\rangle$ that can be saved in a plane wave basis more conveniently. The transformation from $|\tilde{\psi}\rangle$ to $|\psi\rangle$ is $\hat{\mathcal{T}}$:

$$|\psi\rangle = \hat{\mathcal{T}}|\tilde{\psi}\rangle \tag{2.21}$$

A suitable expression for $\hat{\mathcal{T}}$ is found by inquiring a set of properties thereof. First of all, $\hat{\mathcal{T}}$ is unity in the interstitial region (away from the nuclei), as a simple plane-wave expansion is assumed to be suitable there. $\hat{\mathcal{T}}$ thus consists of contributions $\hat{\mathcal{T}}_\mu$ that vanish outside of spheres around each nucleus at position $\underline{R}_\mu$:

$$\hat{\mathcal{T}} = 1 + \sum_\mu \hat{\mathcal{T}}_\mu \tag{2.22}$$

The transformations $\hat{\mathcal{T}}_\mu$ can be chosen for each sphere individually such that they map a set of atom-centered functions $|\tilde{\phi}_i\rangle$ (auxiliary or "pseudo" partial waves) that are conveniently representable in a plane-wave basis onto functions $|\phi_i\rangle$ ("true" partial waves) that form a good basis for the all-electron wave functions near the nuclei:

$$|\phi_i\rangle = (\hat{1} + \hat{\mathcal{T}}_\mu)|\tilde{\phi}_i\rangle \tag{2.23}$$

$$\Leftrightarrow \quad \hat{\mathcal{T}}_\mu|\tilde{\phi}_i\rangle = |\phi_i\rangle - |\tilde{\phi}_i\rangle \tag{2.24}$$

Typical choices for $|\phi_i\rangle$ are atomic eigenfunctions and for $|\tilde{\phi}_i\rangle$ are eigenfunctions of the radial Schrödinger equation in a suitably smoothened

potential, similar to pseudopotential methods described below. $|\phi_i\rangle$ and $|\tilde{\phi}_i\rangle$ are thus chosen to be equal beyond a given cutoff radius for each sphere. So in order to find a closed expression for $\mathcal{T}$, one has to find a representation of $|\tilde{\psi}\rangle$ in the basis of $|\tilde{\phi}_i\rangle$ inside one spere, defining the "projector functions" $\langle\tilde{p}_i|$:

$$|\tilde{\psi}\rangle = \sum_i |\tilde{\phi}_i\rangle\langle\tilde{p}_i|\tilde{\psi}\rangle \qquad \langle\tilde{p}_i|\tilde{\phi}_j\rangle = \delta_{ij} \tag{2.25}$$

The final expression for the PAW wave functions is obtained by inserting (2.22), (2.24) and (2.25) into (2.21):

$$\begin{aligned} |\psi\rangle &= \hat{\mathcal{T}}|\tilde{\psi}\rangle = |\tilde{\psi}\rangle + \sum_\mu \hat{\mathcal{T}}_\mu|\tilde{\psi}\rangle = |\tilde{\psi}\rangle + \sum_\mu \sum_{i\in\mu} \hat{\mathcal{T}}_\mu|\tilde{\phi}_i\rangle\langle\tilde{p}_i|\tilde{\psi}\rangle \\ \Rightarrow \quad |\psi\rangle &= |\tilde{\psi}\rangle + \sum_i \Big(|\phi_i\rangle - |\tilde{\phi}_i\rangle\Big)\langle\tilde{p}_i|\tilde{\psi}\rangle \end{aligned} \tag{2.26}$$

As the partial waves $|\phi_i\rangle$ and $|\tilde{\phi}_i\rangle$ remain fixed during the calculation, it is sufficient to save and calculate with the auxiliary wave functions $|\tilde{\psi}\rangle$ and the matrix elements $\langle\tilde{p}_i|\tilde{\psi}\rangle$. The transformation is in principle exact, however an approximation comes into play when the basis development of (2.25) is truncated. Typically, only one or two basis functions are used. In general, the back-transformation of (2.26) does not have to be done explicitly, because all expectation values of an operator $\hat{A}$ can be calculated from $|\tilde{\psi}\rangle$, $\langle\tilde{p}_i|\tilde{\psi}\rangle$ and the partial waves [BFS03] (restoring band and $\underline{k}$-point indices):

$$\begin{aligned} \langle\hat{A}\rangle &:= \sum_{\underline{k}\nu} \langle\psi_{\underline{k}\nu}|\hat{A}|\psi_{\underline{k}\nu}\rangle \\ &= \sum_{\underline{k}\nu} \langle\tilde{\psi}_{\underline{k}\nu}|\hat{A}|\tilde{\psi}_{\underline{k}\nu}\rangle + \sum_{i,j} \mathcal{D}_{ij}\Big(\langle\phi_j|\hat{A}|\phi_i\rangle - \langle\tilde{\phi}_j|\hat{A}|\tilde{\phi}_i\rangle\Big) \end{aligned} \tag{2.27}$$

The one-centre density matrix $\mathcal{D}_{ij}$ (for each atomic sphere at $\underline{R}_\mu$) that occurs in (2.27) is defined as follows:

$$\mathcal{D}_{ij} := \sum_{\underline{k}\nu} \langle\tilde{p}_i|\tilde{\psi}_{\underline{k}\nu}\rangle\langle\tilde{\psi}_{\underline{k}\nu}|\tilde{p}_j\rangle \tag{2.28}$$

Applying (2.27) to $\hat{A} = |\underline{r}\rangle\langle\underline{r}|$, one obtains an expression for the charge density $n(\underline{r})$:

$$n(\underline{r}) = \tilde{n}(\underline{r}) + \sum_{\mu} \left(n^1_\mu(\underline{r}) - \tilde{n}^1_\mu(\underline{r}) \right) \tag{2.29}$$

The three contributions therein are constructed as follows:

$$\tilde{n}(\underline{r}) = \sum_{\underline{k}\nu} \tilde{\psi}^*_{\underline{k}\nu}(\underline{r})\, \tilde{\psi}_{\underline{k}\nu}(\underline{r}) \tag{2.30}$$

$$n^1_\mu(\underline{r}) = \sum_{i,j\in\mu} \mathcal{D}_{ij}\, \phi^*_j(\underline{r})\, \phi_i(\underline{r}) \tag{2.31}$$

$$\tilde{n}^1_\mu(\underline{r}) = \sum_{i,j\in\mu} \mathcal{D}_{ij}\, \tilde{\phi}^*_j(\underline{r})\, \tilde{\phi}_i(\underline{r}) \tag{2.32}$$

Similar expressions can be written for other observables, such as total energies, forces or electric field gradients [PBBS98].

Actual calculations using the PAW method in the course of this work are done with the "original" implementation, the CP-PAW code by P. Blöchl, documented in [Blö94].

The mixed-basis pseudopotential (MBPP) method

The mixed-basis pseudopotential method [LHC79, FH83, ETH+90] is similar to the PAW formalism with respect to the idea that the original Kohn-Sham wave functions are modified to become more easily basis-representable functions. However, this is not done by an analytically known transformation of the wave-functions themselves, but by a modification of the underlying Kohn-Sham Schrödinger equation that has to be solved. The original basic idea [Ant59, PK59, KP59] can be understood as follows: Suppose $\phi_{\underline{k}\nu}(\underline{r})$ to be exact eigenfunctions with a complex nodal structure, which is caused by the orthogonalisation to core states $\phi_{\underline{k}\nu'}(\underline{r})$ with $\nu' < \nu$ (assuming only one atom per unit cell). So a sufficiently smooth wave function $\psi_{\underline{k}\nu}(\underline{r})$ is given by [AM76]:

$$\phi_{\underline{k}\nu}(\underline{r}) = \psi_{\underline{k}\nu}(\underline{r}) - \sum_{\nu'<\nu} \left(\int \mathrm{d}^3 r'\, \phi^*_{\underline{k}\nu'}(\underline{r}')\psi_{\underline{k}\nu}(\underline{r}') \right) \phi_{\underline{k}\nu'}(\underline{r}) \tag{2.33}$$

Inserting this into the original Kohn-Sham Schrödinger equation, of which the $\phi_{\underline{k}\nu}(\underline{r})$ are exact eigenfunctions with eigenvalues $\epsilon_{\underline{k}\nu}$

$$\begin{aligned} &\hat{H}\psi_{\underline{k}\nu}(\underline{r}) - \sum_{\nu'<\nu} \left(\int \mathrm{d}^3 r' \, \phi^*_{\underline{k}\nu'}(\underline{r}')\psi_{\underline{k}\nu}(\underline{r}') \right) \epsilon_{\underline{k}\nu'}\phi_{\underline{k}\nu'}(\underline{r}) \\ = \; &\epsilon_{\underline{k}\nu} \left(\psi_{\underline{k}\nu}(\underline{r}) - \sum_{\nu'<\nu} \left(\int \mathrm{d}^3 r' \, \phi^*_{\underline{k}\nu'}(\underline{r}')\psi_{\underline{k}\nu}(\underline{r}') \right) \phi_{\underline{k}\nu'}(\underline{r}) \right) \end{aligned} \tag{2.34}$$

one could understand the result as a normal Schrödinger equation for $\psi_{\underline{k}\nu}(\underline{r})$ in which the following artificially-looking non-local pseudopotential $\hat{v}^{\mathrm{PS}}$ is added to the Hamilton operator:

$$\hat{v}^{\mathrm{PS}}\psi_{\underline{k}\nu}(\underline{r}) = \sum_{\nu'<\nu} (\epsilon_{\underline{k}\nu} - \epsilon_{\underline{k}\nu'}) \left(\int \mathrm{d}^3 r' \, \phi^*_{\underline{k}\nu'}(\underline{r}')\psi_{\underline{k}\nu}(\underline{r}') \right) \phi_{\underline{k}\nu'}(\underline{r}) \tag{2.35}$$

Of course, one can immediately see some problems of this simple approach, like the energy transferability (the energy eigenvalues $\epsilon_{\underline{k}\nu}$, in principle, have to be known in advance) and nodes of the wave functions. For this reason, a large set of different pseudopotential construction schemes have been established. The one used here goes back to Vanderbilt [Van85]. It replaces the external part $v(\underline{r})$ of the original Kohn-Sham effective potential $v_{\mathrm{eff}}(\underline{r})$ by a sum of pseudopotentials $v_l^{\mathrm{PS}}(\underline{r})$ for each atom and angular momentum quantum number l that fulfill a number of postulations. Without going too far into details of the construction procedure, these postulations can be understood by investigating the solution of the radial Schrödinger equation $R_l^{\mathrm{PS}}(r)$ in the pseudopotential $v_l^{\mathrm{PS}}(r)$ in question and comparing to the original all-electron solution $R_l^{\mathrm{AE}}(r)$, ϵ_l^{AE} for a free atom:

$$\left(-\frac{\hbar^2}{2m_{\mathrm{e}}} \left(\frac{\mathrm{d}^2}{\mathrm{d}r^2} - \frac{l(l+1)}{r^2} \right) + v_l^{\mathrm{PS}}(r) \right) R_l^{\mathrm{PS}}(r) = \epsilon_l^{\mathrm{PS}} R_l^{\mathrm{PS}}(r) \tag{2.36}$$

As shown in [Mey98], the postulations can be summarised as follows:

1. $R_l^{\mathrm{PS}}(r)$ is *nodeless*.

2. $R_l^{\mathrm{PS}}(r) = R_l^{\mathrm{AE}}(r)$ for all values $r \geq r_{\mathrm{c},l}$

3. $\epsilon_l^{\mathrm{PS}} = \epsilon_l^{\mathrm{AE}}$

4. The *norm* $\int_0^{r_{\mathrm{c},l}} \mathrm{d}r |R_l^{\mathrm{PS}}(r)|^2 = \int_0^{r_{\mathrm{c},l}} \mathrm{d}r |R_l^{\mathrm{AE}}(r)|^2$ is *conserved*.

This set of postulations creates norm-conserving pseudopotentials. (Note that they are not yet uniquely determined). They can be shown to yield a continuous logarithmic derivative of the wave functions at the cutoff radius. Of course, the set can in general be modified, for instance by modifying the last one (norm-conservation), one could get to so-called ultrasoft pseudopotentials. Further steps of the construction procedure are "unscreening" (subtraction of the Hartree and exchange-correlation parts of the pseudopotential), a separation into a local and non-local parts and transforming the result to Fourier space.

In addition to the use of pseudopotentials and in order to reduce E_{pw} further, especially in view of wave functions with low principal quantum numbers (like $3d$) for which the pseudo wave functions and the original ones hardly differ, the MBPP formalism represents the wave functions not only in terms of plane waves (2.19), but uses a mixed basis of plane waves and few localised functions:

$$\psi_{\underline{k}\nu}(\underline{r}) = \frac{1}{\sqrt{\Omega_{\mathrm{C}}}} \sum_{\underline{G}} \psi_{\underline{G}}^{\underline{k}\nu} \mathrm{e}^{\mathrm{i}(\underline{k}+\underline{G})\underline{r}} + \sum_{\mu l m} \beta_{\mu l m}^{\underline{k}\nu} \phi_{\mu l m}^{\underline{k}}(\underline{r}) \tag{2.37}$$

The localised functions $\phi_{\mu l m}^{\underline{k}}(\underline{r})$ with indices μ (atom), l and m (angular momentum and magnetic quantum number) are Bloch transforms of functions with a localised radial part $f_{\mu l}(r)$ and an angular-dependent part of cubic harmonics $\mathrm{K}_{lm}(\hat{\underline{r}})$:

$$\phi_{\mu l m}^{\underline{k}}(\underline{r}) = \sum_{\underline{T}} \mathrm{e}^{\mathrm{i}\underline{k}(\underline{T}+\underline{R}_\mu)} \, \phi_{\mu l m}(\underline{r} - \underline{T} - \underline{R}_\mu) \tag{2.38}$$

$$\phi_{\mu l m}(\underline{r}) = f_{\mu l}(r) \, \mathrm{i}^l \, \mathrm{K}_{lm}(\hat{\underline{r}}) \tag{2.39}$$

For the choice of $f_{\mu l}(r)$, it has proven to be reliable to use the functions $R_{\mu l}^{\mathrm{PS}}(r)$ that are solutions of (2.36) with the constraint that they vanish outside of a sphere with a cutoff radius chosen so that the spheres (ideally) touch, but do not overlap (so that the evaluation of two-centre integrals can be avoided). The constraint is enforced either by multiplication with a suitable cutoff function or by substracting a Bessel function.

The calculation of expectation values in this mixed basis is again shown exemplarily for the charge density, as this observable will be important for the later parts of this work. Inserting (2.37) into (2.9), one obtains three parts $n(\underline{r}) = n_{(1)}(\underline{r}) + n_{(2)}(\underline{r}) + n_{(3)}(\underline{r})$ by regrouping the contributions of plane waves, localised functions and the mixed terms:

$$
\begin{aligned}
n_{(1)}(\underline{r}) &= \frac{1}{\Omega_{\mathrm{C}}} \sum_{\underline{k}\nu} \sum_{\underline{G}} \left| \psi_{\underline{G}}^{\underline{k}\nu} \, \mathrm{e}^{\mathrm{i}(\underline{k}+\underline{G})\underline{r}} \right|^2 \qquad (2.40) \\
n_{(2)}(\underline{r}) &= \frac{2}{\sqrt{\Omega_{\mathrm{C}}}} \sum_{\underline{k}\nu} \Re \left[\sum_{\underline{G}} \psi_{\underline{G}}^{\underline{k}\nu} \, \mathrm{e}^{\mathrm{i}(\underline{k}+\underline{G})\underline{r}} \sum_{\mu l m} \left(\beta_{\mu l m}^{\underline{k}\nu} \right)^* \left(\phi_{\mu l m}^{\underline{k}}(\underline{r}) \right)^* \right] \\
n_{(3)}(\underline{r}) &= \sum_{\underline{k}\nu} \left| \sum_{\mu l m} \beta_{\mu l m}^{\underline{k}\nu} \phi_{\mu l m}^{\underline{k}}(\underline{r}) \right|^2
\end{aligned}
$$

In brief, the first term can be evaluated directly by Fourier transformation of the wave functions to real space. The second and third term, which are zero in the interstitial region due to the choice of non-overlapping spheres, are calculated in a straightforward way in an atom-centered basis. Some more details about the calculation of these terms are given in section 4.2.2.

Actual calculations using the MBPP method in the course of this work are done using an implementation written by B. Meyer, C. Elsässer, F. Lechermann and M. Fähnle [MELFed].

2.1.5 Deficiencies of DFT and its approximations

It cannot be overemphasized that DFT is an extremely successful theory and its groud state expectation values are exact. Anyway, there are weaknesses of the theory, some of which shall be named here.

- As elaborated in section 2.1.3, the exact exchange-correlation potential is generally unknown. The class of systems for which this might lead to problems consists of strongly correlated systems, which are often characterized by strongly localised electrons. A large zoo of phenomena can result from strong correlations, which is too large to be listed here in full detail. Strong electronic correlations are the main point of interest in this work.

- The only state for which DFT is exact is the electronic ground state, exited states are in principle not accessible. Extensions to elevated temperature can be done with the Mermin approach [Mer65], in which basically occupation numbers $n_{\underline{k}\nu}$ corresponding to a Fermi distribution function of the desired temperature are added in (2.9):

$$n(\underline{r}) = \sum_{\underline{k}} \sum_{\nu=1}^{\infty} n_{\underline{k}\nu} |\psi_{\underline{k}\nu}(\underline{r})|^2 \tag{2.41}$$

  Although this is not the main focus of this work, the formalism developed in this work shall have an intrinsic temperature dependence.

- The spectrum of Kohn-Sham energy eigenvalues $\epsilon_{\underline{k}\nu}$, which is often (and again successfully) considered as an approximation to the spectral density of states (DOS) of the system in question, must not be over-interpreted. Strictly speaking, the Kohn-Sham eigenvalues have no physical interpretation and are pure auxiliary quantities. A famous example for a mismatch of Kohn-Sham DOS and true spectra is the Mott insulator, which has a metallic

Kohn-Sham DOS. At least partially, also the band-gap problem is related: In the Kohn-Sham DOS, the size of band gaps is typically largely underestimated.

The aim of the following sections is to describe a method that is able to deal with electronic correlations intrinsically, ideally also being temperature-dependent and providing spectral data. For this purpose, an almost completely different approach to describe a solid-state body is presented to start from, which is the Hubbard model.

2.2 The Hubbard model

It might be a general concept in physics that if one encounters a problem that cannot be solved exactly (here the standard model of solid state physics (1.2)), one may choose between two approaches. The first one, which has been applied in the previous section 2.1, is to find suitable approximations of its solution. The second one is to replace the problem itself by a simpler problem (or model) that still allows to gain insight into the properties of the original problem. The "simpler problem" of this work is the Hubbard model [Hub63,Hub64a,Hub64b].

The aim is to model a solid state body by a lattice model. In its simplest formulation (the one-band Hubbard model), at maximum two electrons can be located on one lattice site j. However, to model the electron-electron interaction (since electrons do not like each other), an energy "cost" of U is introduced if two electrons are at the same site. Luckily, electrons can hop away to a neighbouring site i, which gives an energy "gain" of t_{ij}. (Unfortunately, the electron is not welcome there either.) For a mathematical description of these general ideas, it is instructive to look at the general form of a one-band lattice model in second quantisation [Nol02] (assuming interactions that are not explicitly spin-dependent):

$$\hat{H}^{\text{lattice}} = -\sum_{ij\,\sigma} t_{ij}\,\hat{c}^{\dagger}_{i\sigma}\hat{c}_{j\sigma} + \frac{1}{2}\sum_{ijkl\,\sigma\sigma'} U_{ijkl}\,\hat{c}^{\dagger}_{i\sigma}\hat{c}^{\dagger}_{j\sigma'}\hat{c}_{l\sigma'}\hat{c}_{k\sigma} \tag{2.42}$$

Here, $\hat{c}^\dagger_{i\sigma}$ is the creation operator for an electron at lattice site i with spin σ and $\hat{c}_{i\sigma}$ is the respective annihilation operator. The ideas by Hubbard can be included by restricting t_{ij} to i and j from nearest neighbour lattice sites only, which is denoted by the symbol $\langle ij \rangle$. Furthermore, the electron-electron interaction is restricted to electrons on the same lattice site:

$$U \equiv U_{ijkl}\, \delta_{ji} \delta_{jk} \delta_{jl} \tag{2.43}$$

Due to translational invariance of the lattice model, the remaining index j of U in (2.43) can be dropped. This leads to the Hubbard model:

$$\hat{H}^{\mathrm{Hubbard}} = -\sum_{\langle ij \rangle\, \sigma} t_{ij} \hat{c}^\dagger_{i\sigma} \hat{c}_{j\sigma} + U \sum_j \hat{n}_{j\uparrow} \hat{n}_{j\downarrow} \tag{2.44}$$

In this equation, $\hat{n}_{j\sigma}$ is the density operator, given by:

$$\hat{n}_{j\sigma} \equiv \hat{c}^\dagger_{j\sigma} \hat{c}_{j\sigma} \tag{2.45}$$

The first, two-operator, summand of (2.44) will be denoted as the kinetic term $\hat{H}^{\mathrm{kin}}$, the second four-operator summand is the interacting term $\hat{H}^{\mathrm{int}}$. The limitation of the kinetic term to nearest-neighbour hopping processes is, of course, not necessary and will hardly be used during this work. Instead of using real-space hopping energies directly, it is useful to Fourier-transform the hopping energies t_{ij} to a dispersion relation $H^{\mathrm{kin}}(\underline{k})$ in reciprocal $\underline{k}$-space, again exploiting translational symmetry:

$$\hat{H}^{\mathrm{kin}} = \sum_{\underline{k}\sigma} H^{\mathrm{kin}}(\underline{k})\, \hat{c}^\dagger_{\underline{k}\sigma} \hat{c}_{\underline{k}\sigma} \qquad \text{with} \quad H^{\mathrm{kin}}(\underline{k}) \equiv -\sum_j t_{0j}\, \mathrm{e}^{-\mathrm{i}\underline{k}\cdot(\underline{R}_0 - \underline{R}_j)} \tag{2.46}$$

Thus, $H^{\mathrm{kin}}(\underline{k})$ contains the hopping energies as well as the shape of the lattice that is used. A generalisation thereof to a multi-band lattice model in terms of a matrix $\underline{\underline{H}}^{\mathrm{kin}}(\underline{k})$ in orbital space is straightforward. In analogy, the interacting term $\hat{H}^{\mathrm{int}}$ of a multi-band problem would consist of operators with four orbital indices m_1 to m_4 (the lattice site

index j is dropped for readability since the operator is still assumed to be purely local on one lattice site and translational invariance holds):

$$\hat{H}^{\text{int}} = \frac{1}{2} \sum_{m_1 m_2 m_3 m_4 \, \sigma\sigma'} U_{m_1 m_2 m_3 m_4} \, \hat{c}^{\dagger}_{m_1\sigma} \hat{c}^{\dagger}_{m_2\sigma'} \hat{c}_{m_4\sigma'} \hat{c}_{m_3\sigma} \tag{2.47}$$

During this work, the number of parameters will be reduced significantly by assuming that $U_{m_1 m_2 m_3 m_4}$ is nonzero only if at maximum two different orbital indices occur in each summand. With the density operator (2.45), $\hat{H}^{\text{int}}$ becomes:

$$\begin{aligned} \hat{H}^{\text{int}} &= \frac{1}{2} \sum_{m} \sum_{\sigma\sigma'} U_{mmmm} \;\; \hat{n}_{m\sigma} \hat{n}_{m\sigma'} \\ &+ \frac{1}{2} \sum_{m \neq m'} \sum_{\sigma\sigma'} U_{mm'mm'} \, \hat{n}_{m\sigma} \hat{n}_{m'\sigma'} \\ &+ \frac{1}{2} \sum_{m \neq m'} \sum_{\sigma\sigma'} U_{mm'm'm} \, \hat{c}^{\dagger}_{m\sigma} \hat{c}^{\dagger}_{m'\sigma'} \hat{c}_{m\sigma'} \hat{c}_{m'\sigma} \\ &+ \frac{1}{2} \sum_{m \neq m'} \sum_{\sigma\sigma'} U_{mmm'm'} \, \hat{c}^{\dagger}_{m\sigma} \hat{c}^{\dagger}_{m\sigma'} \hat{c}_{m'\sigma'} \hat{c}_{m'\sigma} \end{aligned} \tag{2.48}$$

With a rearrangement of the spin sums ($\bar{\sigma}$ means the opposite spin than σ) and some creation/annihilation operator arithmetics, this be-

comes:

$$\begin{aligned}
\hat{H}^{\text{int}} &= \frac{1}{2}\sum_{m}\sum_{\sigma} U_{mmmm}\ \hat{n}_{m\sigma}\hat{n}_{m\bar{\sigma}} \\
&+ \frac{1}{2}\sum_{m\neq m'}\sum_{\sigma} U_{mm'mm'}\,\hat{n}_{m\sigma}\hat{n}_{m'\bar{\sigma}} \\
&+ \frac{1}{2}\sum_{m\neq m'}\sum_{\sigma} (U_{mm'mm'} - U_{mm'm'm})\,\hat{n}_{m\sigma}\hat{n}_{m'\sigma} \\
&+ \frac{1}{2}\sum_{m\neq m'}\sum_{\sigma} U_{mm'm'm}\,\hat{c}^{\dagger}_{m\sigma}\hat{c}^{\dagger}_{m'\bar{\sigma}}\hat{c}_{m\bar{\sigma}}\hat{c}_{m'\sigma} \\
&+ \frac{1}{2}\sum_{m\neq m'}\sum_{\sigma} U_{mmm'm'}\,\hat{c}^{\dagger}_{m\sigma}\hat{c}^{\dagger}_{m\bar{\sigma}}\hat{c}_{m'\bar{\sigma}}\hat{c}_{m'\sigma}
\end{aligned} \tag{2.49}$$

One can now make the further simplification to average the interaction parameters over all orbitals, which seems to be a good approximation since for most of the systems in question, the orbitals one takes into account correspond to e. g. one d-shell. With this approximation, one can define:

$$\begin{aligned}
U_{mmmm} &\equiv U \\
U_{mm'mm'} &\equiv U' \\
U_{mm'm'm} &\equiv J \\
U_{mmm'm'} &\equiv J_{\text{C}}
\end{aligned}$$

Like this, one obtains the Slater-Kanamori parametrisation of the interacting Hamilton operator term by four parameters [Kan63]:

$$\begin{aligned}
\hat{H}^{\text{int}} &= U\sum_{m}\hat{n}_{m\uparrow}\hat{n}_{m\downarrow} \\
&+ \frac{1}{2}\sum_{m\neq m'}\sum_{\sigma}\left[U'\,\hat{n}_{m\sigma}\hat{n}_{m'\bar{\sigma}} + (U'-J)\,\hat{n}_{m\sigma}\hat{n}_{m'\sigma}\right] \\
&+ \frac{1}{2}\sum_{m\neq m'}\sum_{\sigma}\left[J\,\hat{c}^{\dagger}_{m\sigma}\hat{c}^{\dagger}_{m'\bar{\sigma}}\hat{c}_{m\bar{\sigma}}\hat{c}_{m'\sigma} + J_{\text{C}}\,\hat{c}^{\dagger}_{m\sigma}\hat{c}^{\dagger}_{m\bar{\sigma}}\hat{c}_{m'\bar{\sigma}}\hat{c}_{m'\sigma}\right]
\end{aligned} \tag{2.50}$$

A frequent choice of the interaction parameters is $U' = U - 2J$ and $J_C = J$, which makes the problem rotationally invariant [Kan63, Bra77, MF95], i. e. invariant under a unitary transformation, and can be motivated by symmetry arguments of a t_{2g} manifold. A further, historically motivated approximation, is to neglect all terms that cannot be written in terms of density operators only, namely the spin-flip (with coefficient J) and pair-hopping (with coefficient J_C) terms. This leads to the following operator:

$$\begin{aligned} \hat{H}^{\text{int}} &= U \sum_m \hat{n}_{m\uparrow}\hat{n}_{m\downarrow} \\ &+ \frac{1}{2} \sum_{m \neq m'} \sum_\sigma \left[U' \, \hat{n}_{m\sigma}\hat{n}_{m'\bar{\sigma}} + (U' - J) \, \hat{n}_{m\sigma}\hat{n}_{m'\sigma} \right] \end{aligned} \tag{2.51}$$

Like this, a strict rotationally invariant formulation is impossible. However, this formulation has advantages for some of the solution methods shown later in terms of calculation time and simplicity of the formulation. In chapter 3, it will be demonstrated exemplarily that the approximation is good at least for nonmagnetic systems where spin-flip and pair-hopping processes have little influence.

Although the Hubbard model generally looks very simple, it still allows to describe many of the most interesting electronic features, especially due to strong electronic correlations. However, no analytic solution of the Hubbard model exists, except for the most simple case of a one-dimensional lattice, in which the Bethe ansatz [LW68, LW03] can be applied. Therefore, several approximative techniques exist, from which the two that are important for the work at hand, are presented in the following.

2.2.1 Dynamical Mean-Field Theory (DMFT)

First of all, it shall be mentioned that Dynamical Mean-Field Theory (DMFT) is, like most explicit many-particle methods, expressed in terms of Green's functions as basic quantities, instead of many-

particle wave functions (that carry too much information, as mentioned above) or other auxiliary quantities like charge densities. The correct expression of the respective basic quantities in terms of the other ones is actually the most important point for the charge self-consistency discussed in chapter 4. For a detailed introduction of Green's functions, see e. g. [Mat76, Nol02]. Green's functions are used as finite-temperature propagators, depending on imaginary times $\mathrm{i}\tau$, $0 < \tau < \beta$, where

$$\beta = \frac{1}{k_\mathrm{B} T}$$

is the inverse temperature. The Green's functions can be continued in a periodic way, so that they can be Fourier-transformed to discrete Matsubara frequencies ω_n with

$$\omega_n = \frac{(2n+1)\pi}{\beta} \qquad n \in \mathbb{Z}$$

The starting point for DMFT has been found in 1989 [MV89], when Metzner and Vollhardt discovered that the self-energy of a fermionic lattice model with infinite coordination number is purely local, i. e. has no $\underline{k}$-dependence. So the basic idea of DMFT is to use a local self-energy also for lattice models with coordination numbers less than infinity, which has proven to be a reliable approximation except, of course, for one-dimensional lattices (i. e. chains).

But why is this approximation helpful for the actual calculations? The idea is that due to the locality of the self-energy it is possible to pick out one lattice site and treat the coupling to the rest of the lattice on a mean-field like level [GK92]. This can most easily be understood in an effective action formalism [GKKR96] (see e. g. [NO88] for an introduction). For simplicity, it is written for the single-band Hubbard model (2.44):

$$S_\mathrm{eff} = -\int_0^\beta \mathrm{d}\tau \int_0^\beta \mathrm{d}\tau' \sum_\sigma c_\sigma^\dagger(\tau) \mathcal{G}_0^{-1}(\tau - \tau') c_\sigma(\tau') + U \int_0^\beta \mathrm{d}\tau \, n_\uparrow(\tau) n_\downarrow(\tau) \tag{2.52}$$

So the coupling to the lattice is incorporated into a purely local Green's function-like quantity $\mathcal{G}_0(\mathrm{i}\omega_n)$ on the two-operator level. Due to formal analogies with mean-field theories of an Ising model, it is frequently called the Weiss field. Alternatively, the hybridisation function $\Delta(\mathrm{i}\omega_n)$ can be used:

$$\mathcal{G}_0^{-1}(\mathrm{i}\omega_n) = \mathrm{i}\omega_n + \mu - \Delta(\mathrm{i}\omega_n) \tag{2.53}$$

Furthermore, due to the construction scheme as a two-c-operator term, one can write down Dyson's equation for $\mathcal{G}_0$ (written in matrix-form to account for e. g. spin, orbital, cluster site, ...)

$$\underline{\underline{\Sigma}}^{\mathrm{imp}}(\mathrm{i}\omega_n) = \underline{\underline{\mathcal{G}_0}}^{-1}(\mathrm{i}\omega_n) - (\underline{\underline{G}}^{\mathrm{imp}})^{-1}(\mathrm{i}\omega_n) \tag{2.54}$$

The impurity Green's function $\underline{\underline{G}}^{\mathrm{imp}}$ evolves by evaluating the effective action S_{eff}, which defines the impurity self-energy $\underline{\underline{\Sigma}}^{\mathrm{imp}}$. So the DMFT approximation can be summarised by the assumption that this (local) impurity self-energy is equal to the original lattice self-energy. Of course, the problem of the theory up to now is that $\mathcal{G}_0$ is not known. So the DMFT evaluation is done via a self-consistency cycle:

1. Start from an arbitrary local self-energy $\underline{\underline{\Sigma}}^{\mathrm{imp}}$.

2. Construct a lattice Green's function by setting its self-energy $\underline{\underline{\Sigma}}(\mathrm{i}\omega_n)$ to the impurity self-energy $\underline{\underline{\Sigma}}^{\mathrm{imp}}(\mathrm{i}\omega_n)$. Extract its local part by $\underline{k}$-summation:

$$\underline{\underline{G}}^{\mathrm{loc}}(\mathrm{i}\omega_n) = \sum_{\underline{k}} \left[(\mathrm{i}\omega_n + \mu)\underline{\underline{1}} - \underline{\underline{H}}^{\mathrm{kin}}(\underline{k}) - \underline{\underline{\Sigma}}(\mathrm{i}\omega_n)\right]^{-1} \tag{2.55}$$

3. Construct a trial Weiss field $\underline{\underline{\mathcal{G}_0}}$ using the inverse of (2.54):

$$\underline{\underline{\mathcal{G}_0}}^{-1}(\mathrm{i}\omega_n) = \underline{\underline{\Sigma}}^{\mathrm{imp}}(\mathrm{i}\omega_n) + (\underline{\underline{G}}^{\mathrm{imp}}(\mathrm{i}\omega_n))^{-1} \tag{2.56}$$

4. Evaluate (2.52) to obtain $\underline{\underline{G}}^{\mathrm{imp}}$ via one of the "impurity solvers" sketched below.

5. Construct a new impurity self-energy using (2.54).

6. Mix the new impurity self-energy with the input self-energy. This is usually done with a simple linear mixing scheme. More sophisticated techniques like Broyden's mixing are useful only for data that contains virtually no noise [SSG+11].

7. Start from the beginning until a fix-point of the impurity self-energy is reached.

The main difference to standard mean-field theories is the full frequency dependence of $\mathcal{G}_0$, hence the name "dynamical". Therefore the theory does allow for local quantum fluctuations and full temperature dependence. Sometimes it is useful to write the formalism not only via an effective action, but to find a Hamilton operator formulation. This is typically done using an Anderson impurity model, which contains a "bath" degree of freedom to describe the coupling to the lattice and the "impurity", which is the selected lattice site:

$$\hat{H}^{\mathrm{AIM}} = \hat{H}^{\mathrm{imp}} + \hat{H}^{\mathrm{bath}} + \hat{H}^{\mathrm{hyb}} + \left(\hat{H}^{\mathrm{hyb}}\right)^{\dagger} \tag{2.57}$$

So the impurity part $\hat{H}^{\mathrm{imp}}$ incorporates all local terms of the Hubbard model (especially the four-c-operator interactions). The bath part $\hat{H}^{\mathrm{bath}}$ is defined via non-interacting bath states $\hat{a}^{\dagger}_{l\sigma}$

$$\hat{H}^{\mathrm{bath}} = \sum_{l\sigma} \tilde{\epsilon}_l \hat{a}^{\dagger}_{l\sigma} \hat{a}_{l\sigma} \tag{2.58}$$

and the hybridisation part $\hat{H}^{\mathrm{hyb}}$ is the coupling of the two:

$$\hat{H}^{\mathrm{hyb}} = \sum_{lm\sigma} \tilde{V}_{lm} \hat{a}^{\dagger}_{l\sigma} \hat{c}_{m\sigma} \tag{2.59}$$

The parameters $\tilde{\epsilon}_l$ and $\tilde{V}_{lm}$, in this formulation, form the above-mentioned hybridisation function $\Delta(\mathrm{i}\omega_n)$:

$$\Delta_{mm'}(\mathrm{i}\omega_n) = \sum_{l} \frac{\tilde{V}^{*}_{lm} \tilde{V}_{lm'}}{\mathrm{i}\omega_n - \tilde{\epsilon}_l} \tag{2.60}$$

Impurity Solvers

The evaluation of (2.52) or the Anderson impurity model is still a highly non-trivial problem, although significantly simplified compared to the original lattice problem. This evaluation is the task of "impurity solvers". The basic ideas of some existing solution schemes shall be sketched in this section.

Probably the most straightforward scheme is to diagonalise the Anderson impurity Hamilton operator (2.57) directly using a suitable discrete set of bath energies $\tilde{\epsilon}_l$ and couplings $\tilde{V}_{lm}$. This is the basic idea of the **Exact Diagonalisation (ED)** approach. The name might be misleading since it does not provide an exact solution of the Anderson impurity model, but only of the auxiliary model with discrete energies, whose number is computationally limited.

Also the **RISB** technique sketched in the following section can be formulated to solve the Anderson impurity model. However, this is not done here, RISB is only applied in a lattice implementation.

To obtain (numerically) exact solutions of the Anderson impurity model, **Continuous-Time Quantum Monte-Carlo (CT-QMC)** techniques can be used. The basic idea thereof is to split the effective action S_{eff} into an exactly solvable part S_0 and a not necessarily small part ΔS (or the equivalent in a Hamilton operator formulation), so that its path-integral evaluation to find the partition function Z can be done in a perturbative way using a power series expansion:

$$Z = \int \mathcal{D}[c^\dagger c]\, \mathrm{e}^{-S_0 - \Delta S} \tag{2.61}$$

$$= \int \mathcal{D}[c^\dagger c]\, \mathrm{e}^{-S_0} \sum_k \frac{(-1)^k}{k!} (\Delta S)^k \tag{2.62}$$

A possible decomposition can be seen already in (2.52) (written for

the one-band case to simplify notations):

$$S_0 = -\int_0^\beta \mathrm{d}\tau \int_0^\beta \mathrm{d}\tau' \sum_\sigma c_\sigma^\dagger(\tau)\mathcal{G}_0^{-1}(\tau-\tau')c_\sigma(\tau') \tag{2.63}$$

$$\Delta S = U\int_0^\beta \mathrm{d}\tau\, n_\uparrow(\tau)n_\downarrow(\tau) \tag{2.64}$$

This is the basic idea of interaction-expansion or "weak-coupling" CT-QMC [RL04]. It basically leads to the following expansion [GML+11] of the partition function Z (knowing the exact part Z_0):

$$Z = Z_0\sum_{k=0}^\infty \frac{(-U)^k}{k!}\int_0^\beta \mathrm{d}\tau_1\cdots\mathrm{d}\tau_k\left(\prod_\sigma \det \underline{\underline{D}}_k^\sigma\right) \tag{2.65}$$

$$(\underline{\underline{D}}_k^\sigma)_{ij} \equiv \mathcal{G}_0^\sigma(\tau_i-\tau_j) \tag{2.66}$$

Some further tricks are required to avoid sign problems. So this approach leads to small perturbation orders especially for small interactions U. A complementary approach attempts the opposite, namely being particularly efficient for large interactions U. This hybridisation-expansion or "strong-coupling" CT-QMC [WCdM+06, WM06] idea makes an expansion in the hybridisation parts $\hat{H}^{\mathrm{hyb}}$ and $(\hat{H}^{\mathrm{hyb}})^\dagger$ of the Anderson impurity Hamilton operator (2.57). In the effective action formalism, this corresponds to the hybridisation function $\Delta(\tau)$ (written in super-indices α for spin, orbital, ...) [Hau07]:

$$\Delta S = \int_0^\beta \mathrm{d}\tau \int_0^\beta \mathrm{d}\tau' \sum_\sigma c_\alpha^\dagger(\tau)\Delta_{\alpha\alpha'}(\tau-\tau')c_{\alpha'}(\tau') \tag{2.67}$$

The resulting partition function is similar to the interaction expansion

approach (with the bath partition function Z_{bath}) [GML+11]:

$$\begin{aligned} Z &= Z_{\text{bath}} \sum_k \int \mathrm{d}\tau_1 \cdots \mathrm{d}\tau_k \sum_{\alpha_1 \ldots \alpha_k} \sum_{\alpha'_1 \ldots \alpha'_k} \mathrm{Tr}_c \left[T_\tau \mathrm{e}^{-\beta \hat{H}^{\text{imp}}} \right. \\ &\cdot \left. c_{\alpha_k}(\tau_k) c_{\alpha'_k}(\tau'_k) \cdots c_{\alpha_1}(\tau_1) c_{\alpha'_1}(\tau'_1) \right] \det \underline{\underline{M}}^{-1} \qquad (2.68) \\ \left(\underline{\underline{M}}^{-1}\right)_{lm} &\equiv \Delta_{j_l j_m}(\tau_l - \tau_m) \qquad (2.69) \end{aligned}$$

So it is the task of a Monte-Carlo algorithm to evaluate the integrands. The procedure shall not be described in full detail here, for details see [GML+11]. Just to name the basic steps, by starting from an initial configuration, it is necessary to define Monte-Carlo moves that

- insert a creation-annihilation-operator pair at times (τ_s, τ'_s), thus enlarging the perturbation order k,
- remove a creation-annihilation-operator pair, thus lowering k.

Further moves, e. g. leaving k fixed, are possible. As introduced e. g. by the Metropolis-Hastings-algorithm [MRR+53, Has70], the probability to accept such a move differs from its proposal probability. Finally, the desired observables (most notably Green's functions) are measured with the new configuration (or the old one, if the new one is rejected) and Monte-Carlo averaged.

As mentioned, the advantage of the Monte-Carlo algorithms is that they are "numerically" exact. However, the big disadvantages are the large computational requirements of the schemes and the Monte-Carlo noise that is introduced. In the present thesis, the applied Monte-Carlo scheme is the hybridisation-expansion CT-QMC scheme as implemented in the TRIQS code [FP].

2.2.2 Rotationally Invariant Slave-Bosons (RISB)

The introduction into the RISB methodology is kept very brief, because it is used only for small applications. For a more detailed in-

troduction, [Pie10] is highly recommendable. The concept of slave-bosons has first been applied in this context by Kotliar and Ruckenstein [KR86], concentrating on the one-band Hubbard model (2.44). The slave-boson creation operators can be understood as projection operators creating an empty state at site j ($\hat{e}_j^\dagger$), one particle with spin σ ($\hat{p}_{j\sigma}^\dagger$) or a double occupied state ($\hat{d}_j^\dagger$). They fulfill bosonic commutation rules and act on an enlarged Hilbert space with the vacuum state $|\text{vac}\rangle$. The elements of this enlarged Hilbert space can be represented as outer products of a bosonic part created by the slave-bosons and a fermionic quasi-particle part created by operators $\hat{f}_{j\sigma}^\dagger$. In total, the following mapping can be done between the original (physical) Hilbert space of operators $\hat{c}_{j\sigma}^\dagger$ acting on $|0\rangle$ and the enlarged Hilbert space [Pie10]:

$$\begin{aligned} |0\rangle &\rightarrow \hat{e}_j^\dagger\ |\text{vac}\rangle \\ \hat{c}_{j\sigma}^\dagger|0\rangle &\rightarrow \hat{f}_{j\sigma}^\dagger\hat{p}_{j\sigma}^\dagger|\text{vac}\rangle \\ \hat{c}_{j\uparrow}^\dagger\hat{c}_{j\downarrow}^\dagger|0\rangle &\rightarrow \hat{f}_{j\uparrow}^\dagger\hat{f}_{j\downarrow}^\dagger\hat{d}_j^\dagger\ |\text{vac}\rangle \end{aligned} \tag{2.70}$$

This enlarged Hilbert space contains more states than the physical Hilbert space. Therefore, one has to add constraints in order not to leave the latter. The necessary constraints are a completeness relation [KR86]

$$\sum_\sigma \hat{p}_{j\sigma}^\dagger\hat{p}_{j\sigma} + \hat{e}_j^\dagger\hat{e}_j + \hat{d}_j^\dagger\hat{d}_j = 1 \tag{2.71}$$

that takes care of the fact that exactly one of the four possible states can be occupied and a constraint that ensures the correct occupation per spin:

$$\hat{p}_{j\sigma}^\dagger\hat{p}_{j\sigma} + \hat{d}_j^\dagger\hat{d}_j = \hat{f}_{j\sigma}^\dagger\hat{f}_{j\sigma} \tag{2.72}$$

Assuming that both constraints are fulfilled exactly, one can reformulate the Hubbard model (2.44) by using a renormalisation operator $\hat{z}_{j\sigma}$:

$$\hat{z}_{j\sigma} \equiv \hat{e}_j^\dagger\hat{p}_{j\sigma} + \hat{p}_{j\bar{\sigma}}^\dagger\hat{d}_j \tag{2.73}$$

So the Hubbard model Hamilton operator $\underline{\hat{H}}^{\text{Hubbard}}$ of the enlarged Hilbert space becomes:

$$\underline{\hat{H}}^{\text{Hubbard}} = -\sum_{\langle ij\rangle\,\sigma} t_{ij}\hat{f}^{\dagger}_{i\sigma}\hat{f}_{j\sigma}\hat{z}^{\dagger}_{i\sigma}\hat{z}_{j\sigma} + U\sum_{j}\hat{d}^{\dagger}_{j}\hat{d}_{j} \tag{2.74}$$

From this picture, one can nicely see the general mode of operation of the slave-boson theory: The original fermions are replaced by quasi-particle degrees of freedom which are renormalised by the bosonic degrees of freedom. The interactions of the fermions are mapped onto the slave-bosons, so that the interaction term no longer contains four fermionic operators, but two bosonic operators only. Furthermore, one can directly see that this reformulation is possible only for density-density interactions, which are in general not rotationally invariant. The generalisation to non-density-density interactions (RISB), including multi-band models, has been shown in [LGKP07], based on the ideas of [LWH89]. In this context, slave-bosons $\hat{\phi}^{\dagger}_{An}$ are introduced for each pair of physical electron state A (empty, particle and double-occupied in the Kotliar-Ruckenstein formulation, any atomic multiplet in the generalisation to multi-orbital models) and quasi-particle state n. The basis states of the enlarged Hilbert space thus become:

$$|\underline{A}\rangle \equiv \frac{1}{\sqrt{D_A}}\sum_{n}\hat{\phi}^{\dagger}_{An}|\text{vac}\rangle \otimes |n\rangle_{\text{f}} \tag{2.75}$$

In this expression, D_A serves as a normalisation factor corresponding to the dimension of the subspace with the same particle number as A. $|n\rangle_{\text{f}}$ is the quasi-particle part of the state. The required constraints are:

$$\sum_{An}\hat{\phi}^{\dagger}_{An}\hat{\phi}_{An} = 1 \tag{2.76}$$

$$\sum_{A}\sum_{nn'}\hat{\phi}^{\dagger}_{An'}\hat{\phi}_{An}\langle n|\hat{f}^{\dagger}_{\alpha}\hat{f}_{\alpha'}|n'\rangle = \hat{f}^{\dagger}_{\alpha}\hat{f}_{\alpha'} \tag{2.77}$$

This formulation allows to express the multi-orbital Hubbard Hamilton operator as follows:

$$\begin{aligned} \underline{\hat{H}}^{\text{Hubbard}} &= \sum_{\underline{k}} \sum_{\alpha\beta} \{\underline{\underline{R}}^{\dagger} \cdot \underline{\underline{H}}^{\text{kin}}(\underline{k}) \cdot \underline{\underline{R}}\}_{\alpha\beta} \hat{f}^{\dagger}_{\underline{k}\alpha} \hat{f}_{\underline{k}\beta} \\ &+ \sum_{AB} \langle A|\hat{H}^{\text{int}}|B\rangle \sum_{n} \hat{\phi}^{\dagger}_{An} \hat{\phi}_{Bn} \end{aligned} \tag{2.78}$$

Details on how to calculate the renormalisation matrices $\underline{\underline{R}}$ from the slave-bosons can be found in [LGKP07], [Pie10] or [Sch12].

Up to this point, only an exact reformulation of the original problem has been done. Approximations come into play when evaluating the RISB problem numerically. Here, this is done on a mean-field level, using the path-integral formalism. The contribution due to the free fermionic quasi-particles can be integrated out directly. The remaining slave-bosons are "condensed" in a mean-field way to their time-independent expectation values, which are complex numbers:

$$\hat{\phi}_{An} \to \langle \hat{\phi}_{An} \rangle \equiv \varphi_{An} \in \mathbb{C} \tag{2.79}$$

So this approach cannot directly take into account a temperature dependence, Hubbard bands or local quantum fluctuations, which are one of the strengths of DMFT. The constraints mentioned above are satisfied by Lagrange multipliers $\underline{\underline{\Lambda}}$ and λ_0. So the following energy functional Ω can be found from the path integral [Pie10]:

$$\begin{aligned} \Omega[\{\varphi_{An}\}, \underline{\underline{\Lambda}}, \lambda_0] &= -\frac{1}{\beta} \sum_{\underline{k}} \operatorname{Tr} \ln \left[1 + \mathrm{e}^{-\beta \underline{\underline{H}}^{C}(\underline{k})} \right] - \lambda_0 \\ &+ \sum_{ABnn'} \varphi^{*}_{An} \Bigg[\delta_{nn'} \delta_{AB'} \lambda_0 + \delta_{nn'} \langle A|\hat{H}^{\text{int}}|B\rangle \\ &- \delta_{AB} \sum_{\alpha\beta} \Lambda_{\alpha\beta} \langle n|\hat{f}^{\dagger}_{\alpha} \hat{f}_{\beta}|n'\rangle \Bigg] \varphi_{Bn} \end{aligned} \tag{2.80}$$

In this equation, the RISB renormalised free Hamilton operator $\underline{\underline{H}}^{\mathrm{C}}$ is defined as follows:

$$\underline{\underline{H}}^{\mathrm{C}}(\underline{k}) \equiv \underline{\underline{R}}^{\dagger} \cdot \underline{\underline{H}}^{\mathrm{kin}}(\underline{k}) \cdot \underline{\underline{R}} + \underline{\underline{\Lambda}} \tag{2.81}$$

So the practical evaluation is done by minimising Ω with respect to the (condensed) slave-bosons and Lagrange multipliers, e. g. by Broyden's algorithm [Bro65]. This is a task which is numerically demanding, especially for systems with large numbers of degrees of freedom, but significantly faster than the quantum Monte-Carlo calculations that are required in the context of DMFT. So the main strength of RISB is the possibility of doing large scans, e. g. of entire phase diagrams as demonstrated in [SPL12, Sch12], reasonably fast. The main output quantities are the renormalisation matrices, which can be written more intuitively as the quasi-particle weight $\underline{\underline{Z}}$:

$$\underline{\underline{Z}} = \underline{\underline{R}}^{\dagger} \cdot \underline{\underline{R}} \tag{2.82}$$

Furthermore, the quasi-particle weight is connected to the frequency derivative of the self-energy at $\omega = 0$:

$$\underline{\underline{Z}} = \left(\underline{\underline{1}} - \left. \frac{\partial \underline{\underline{\Sigma}}}{\partial \omega} \right|_{\omega=0} \right)^{-1} \tag{2.83}$$

So the Green's functions of RISB in the saddle-point approximation would comprise self-energies that are linear in ω, as opposed to the full frequency dependence of DMFT.

2.3 The Interface

At this point, the question arises how the Hubbard model described in section 2.2 can help to improve density functional theory (or at least the approximations thereof) as described in section 2.1. The answer seems surprisingly simple: The idea is to take the $\underline{k}$-dependent Kohn-Sham Hamilton operator of (2.13), express it in a suitable basis set

(the correlated subspace $\mathcal{C}$), use the resulting matrix as the up-to-now undetermined kinetic part $\underline{\underline{H}}^{\mathrm{kin}}(\underline{k})$ of the Hubbard model Hamilton operator and solve the Hubbard model with this input.

At first glance, this approach might look like nonsense. One has to keep in mind that DFT is, in principle, an exact theory, only the approximations to the density functional (like LDA) make it in total an approximation. This, in turn, means that if the correct density functional was known (which is obviously not the case), DFT would take into account all electronic correlations exactly. However, using the Kohn-Sham Hamilton operator as an input for the kinetic part of the Hubbard model would imply that it contains no electronic correlations at all and is a pure non-interacting one-particle theory. Of course, both extremes are not true, but the underlying problem is known as the double counting problem sketched in section 2.3.3.

A second problem that one might notice is that it has been emphasized that the Kohn-Sham one-particle wave functions that form the Kohn-Sham Hamilton operator (or vice versa) have no physical meaning themselves. However, it has proven to be practical to look at these one-particle quantities to describe physical properties like band structures and densities of states, so that this approach seems to be well suited.

One might further object that the approach as it is sketched above does not truly improve density functional theory, but merely makes DFT a prelude for the determination of parameters for a model-like theory, or, vice versa, the Hubbard model is used only as a post-processing tool for DFT to make some of the observables look more suitable. (Note further that the other parameters of the Hubbard model like U and J are still to be determined, either by a different calculational approach or by physical arguments like the comparison to other materials.) However, the further intertwining of DFT and the Hubbard model in terms of the charge self-consistency of the DFT and (mostly) DMFT output charge densities will be the main topic of the work at hand and is presented in detail in chapter 4. Here, to start with, an overview of the state-of-the-art post-processing (or

single-shot) scheme shall be given.

The most important remaining question is, of course, how exactly the interface between DFT and the Hubbard model looks like. It has been mentioned in a sloppy way that the Kohn-Sham Hamilton operator has to be expressed in a suitable basis set. One has to keep in mind that this basis set may contain at most five basis functions (the fewer the better), but anyway has to describe the entire low-energy physics (near the Fermi level) and thus has to reproduce the one-particle band structure of DFT as accurately as possible. The two construction scheme candidates for a suitable basis that are used in this work are presented in the following sections.

2.3.1 Maximally Localised Wannier Functions

Maximally Localised (generalised) Wannier Functions have been introduced by Marzari and Vanderbilt in 1997 [MV97]; the implementation that is put into practice for this work is described in [MYL+08]. Wannier functions $w_\nu(\underline{r}-\underline{R})$ are simply the Fourier (or Bloch) transforms of the Bloch wave functions $\psi_{\underline{k}\nu}(\underline{r})$ that are the output of DFT:

$$w_\nu(\underline{r}-\underline{R}) = \frac{V}{(2\pi)^3}\int \mathrm{d}\underline{k}\,\psi_{\underline{k}\nu}(\underline{r})\,\mathrm{e}^{-\mathrm{i}\underline{k}\cdot\underline{R}} \tag{2.84}$$

The normalisation factor of this Brillouin zone integral corresponds to the real space unit cell volume V. Thus, Wannier functions are the natural basis for quantum lattice models. Rewriting the Bloch wave functions they stem from as a sum of a lattice periodic part $u_{\underline{k}\nu}(\underline{r})$ and an exponential factor

$$\psi_{\underline{k}\nu}(\underline{r}) = u_{\underline{k}\nu}(\underline{r})\cdot\mathrm{e}^{-\mathrm{i}\underline{k}\cdot\underline{r}} \tag{2.85}$$

it is easy to see that functions $u_{\underline{k}\nu}(\underline{r})$ are not uniquely determined, but only up to a phase factor or, for multi-band problems, a unitary rotation:

$$u_{\underline{k}\nu}(\underline{r}) \quad\longrightarrow\quad \sum_{\nu'} U_{\nu'\nu}(\underline{k})\cdot u_{\underline{k}\nu'}(\underline{r}) \tag{2.86}$$

The idea by Marzari and Vanderbilt for the maximal localisation is to use the arbitrary $\underline{k}$-dependent unitary matrix $U_{\nu'\nu}(\underline{k})$ in order to maximise the localisation of the resulting Wannier functions. This is, of course, desirable for the motivation of the theories presented in this work. This sloppy definition of "maximal localisation" can be quantified via the delocalisation or "spread" functional Ω [FB60, Boy66]:

$$\Omega \equiv \sum_{\nu} \left[\langle r^2 \rangle_\nu - \bar{\underline{r}}_\nu^2 \right] \tag{2.87}$$

In this definition, $\langle r^2 \rangle_\nu$ is simply the expectation value of the squared position operator r^2 in the νth Wannier function, $\bar{\underline{r}}_\nu$ is the expectation value of the position operator, which can be understood as the centroid of the Wannier function, frequently called the Wannier centre. Note that this is not necessarily the position of the atomic nucleus. So the whole expression resembles a standard deviation. It can be shown that this functional can equivalently be written as the sum of the quadratic repulsions of the Wannier functions with themselves [Boy66]. In the end, the only quantities that enter the calculation of the functional Ω are the overlap matrix elements $M_{\nu\nu'}(\underline{k}, \underline{b})$:

$$M_{\nu\nu'}(\underline{k}, \underline{b}) \equiv \int \mathrm{d}^3 r \; u^*_{\underline{k}\nu}(\underline{r}) \cdot u_{\underline{k}+\underline{b},\nu'}(\underline{r}) \tag{2.88}$$

The mimimisation of Ω is done via a steepest-descent minimisation algorithm and is described in detail in the original publication [MV97].

One might notice that the above construction scheme is valid only if the number of constructed Wannier functions is equal to the number of input Bloch functions. So this requires a certain isolated set of Bloch bands to be able to build a suitably-sized correlated subspace. However, for systems in which the desired bands near the Fermi level are mixed with or attatched to other bands, a special "disentanglement" scheme has been proposed [SMV01]. In this scheme, the effective dispersion relation of the resulting Wannier functions does not necessarily correspond to the original Bloch band structure (except in

a previously defined "inner window"), but rather extrapolates between the original bands. An example for this scheme is shown in chapter 3.

2.3.2 Projections onto Localised Orbitals

Although the maximally localised Wannier functions provide a very accurate and well-suited basis for a correlated subspace, they have one severe disadvantage: They depend heavily on the shape of the Bloch functions that are the result of the underlying DFT calculation. Besides some technical complications, this yields some problems e. g. for the charge self-consistency for which the result of the Hubbard model calculation is put back into the DFT equations. In this cycle, the Wannier function basis would vary from iteration to iteration, so that an additional degree of freedom would be introduced that is difficult to describe in a variational way. For this reason, a different framework is used in this context, which are the projections onto localised orbitals (PLO), which are presented in [ALG+08].

As the name suggests, the principal idea of the formalism is to project the Bloch wave functions $|\psi_{\underline{k}\nu}\rangle$, Green's functions as well as all other relevant quantities onto previously defined "localised" functions $|\chi_{\underline{T}m}\rangle$ at lattice vector $\underline{T}$, or the Bloch transform $|\chi_{\underline{k}m}\rangle$ thereof, respectively. The index m is supposed to be a combined orbital and, since more than one atom per unit cell is possible, atomic index. This is not yet the basis in which the Hamilton operator $\underline{\underline{H}}^{\mathrm{kin}}(\underline{k})$ is expressed. Suppose that the basis in which $\underline{\underline{H}}^{\mathrm{kin}}(\underline{k})$ is expressed is $|B_{\underline{k}\alpha}\rangle$. (Note that the number of functions $|\chi_{\underline{k}m}\rangle$ and $|B_{\underline{k}\alpha}\rangle$ does not necessarily coincide.) Then it is possible to rewrite the basic quantity of DMFT, which is the local Green's function $\underline{\underline{G}}^{\mathrm{loc}}(i\omega_n)$, as follows, as it has been shown in [LGP+06]:

$$G^{\mathrm{loc}}_{mm'}(\mathrm{i}\omega_n) = \sum_{\underline{k}} \sum_{\alpha\alpha'} \langle \chi_{\underline{k}m} | B_{\underline{k}\alpha} \rangle \langle B_{\underline{k}\alpha'} | \chi_{\underline{k}m'} \rangle \cdot \left(\left[(\mathrm{i}\omega_n + \mu)\underline{\underline{1}} - \underline{\underline{H}}^{\mathrm{kin}}(\underline{k}) - \Delta\underline{\underline{\Sigma}}(\underline{k}, \mathrm{i}\omega_n) \right]^{-1} \right)_{\alpha\alpha'} \tag{2.89}$$

In this equation, $\Delta\underline{\underline{\Sigma}}(\underline{k}, \mathrm{i}\omega_n)$ can be upfolded from the impurity self energy $\underline{\underline{\Sigma}}^{\mathrm{imp}}(\mathrm{i}\omega_n)$ from DMFT as follows:

$$\Delta\Sigma_{\alpha\alpha'}(\underline{k}, \mathrm{i}\omega_n) = \sum_{mm'} \langle B_{\underline{k}\alpha} | \chi_{\underline{k}m} \rangle \left[\Sigma^{\mathrm{imp}}_{mm'}(\mathrm{i}\omega_n) - \Sigma^{\mathrm{dc}}_{mm'} \right] \langle \chi_{\underline{k}m'} | B_{\underline{k}\alpha'} \rangle \tag{2.90}$$

The double-counting correction $\underline{\underline{\Sigma}}^{\mathrm{dc}}$ will be discussed in the following section. In order to recreate the "standard" formalism involving (e. g.) the maximally localised Wannier functions of section 2.3.1, one could use these both for the functions $|\chi_{\underline{k}m}\rangle$ and $|B_{\underline{k}\alpha}\rangle$ and (2.89) would become the original (2.55). However, the idea of the present projection scheme is to make a very simple choice for $|B_{\underline{k}\alpha}\rangle$, namely a subset $\mathcal{W}$ of the original Bloch wave functions $|\psi_{\underline{k}\nu}\rangle$, so that the kinetic part of the Hamilton operator $\underline{\underline{H}}^{\mathrm{kin}}(\underline{k})$ becomes diagonal:

$$H^{\mathrm{kin}}_{\nu\nu'}(\underline{k}) = \epsilon_{\underline{k}\nu}\, \delta_{\nu\nu'} \tag{2.91}$$

$\epsilon_{\underline{k}\nu}$ are simply the Kohn-Sham energy eigenvalues defined in (2.13). The "magic" of this approach is thus hidden in the choice of suitable localised functions $|\chi_{\underline{k}m}\rangle$, which is described later in this section for the different DFT basis sets in question. The $|\chi_{\underline{k}m}\rangle$ form the basis of the "correlated subspace" $\mathcal{C}$. One can define the projection matrix elements that occur in (2.89) as follows:

$$\begin{aligned} \tilde{P}_{m\nu}(\underline{k}) &\equiv \langle \chi_{\underline{k}m} | \psi_{\underline{k}\nu} \rangle \\ \tilde{P}^{*}_{\nu m}(\underline{k}) &= \langle \psi_{\underline{k}\nu} | \chi_{\underline{k}m} \rangle \end{aligned} \tag{2.92}$$

It is important to note that the matrix $\underline{\underline{\tilde{P}}}(\underline{k})$ is, in general, not quadratic, since the subspace $\mathcal{W}$ of Bloch bands is, in general, larger than the correlated subspace $\mathcal{C}$. Only in the case of systems with well seperated low-energy bands, $\mathcal{C}$ can occasionally be chosen equally large as $\mathcal{W}$.

The localised orbitals $|\chi_{\underline{k}m}\rangle$ can be expressed in terms of the Bloch wave functions $|\psi_{\underline{k}\nu}\rangle$ as usual:

$$|\chi_{\underline{k}m}\rangle = \sum_{\nu} \langle \psi_{\underline{k}\nu} | \chi_{\underline{k}m} \rangle | \psi_{\underline{k}\nu} \rangle \tag{2.93}$$

However, if one actually uses the projection matrices of (2.92), the sum does not run over the whole Bloch space (which would be computationally impossible), so that one obtains different functions $|\tilde{\chi}_{\underline{k}m}\rangle$:

$$|\tilde{\chi}_{\underline{k}m}\rangle = \sum_{\nu\in\mathcal{W}} \tilde{P}^*_{\nu m}(\underline{k})\,|\psi_{\underline{k}\nu}\rangle = \sum_{\nu\in\mathcal{W}} \langle\psi_{\underline{k}\nu}|\chi_{\underline{k}m}\rangle|\psi_{\underline{k}\nu}\rangle \tag{2.94}$$

The functions $|\tilde{\chi}_{\underline{k}m}\rangle$ have the disadvantage that they are, in general, not normalised, but have a non-diagonal overlap $\underline{\underline{O}}(\underline{k})$:

$$O_{mm'}(\underline{k}) \equiv \langle\tilde{\chi}_{\underline{k}m}|\tilde{\chi}_{\underline{k}m'}\rangle = \sum_{\nu\in\mathcal{W}} \tilde{P}_{m\nu}(\underline{k})\,\tilde{P}^*_{\nu m'}(\underline{k}) \tag{2.95}$$

So, in order to obtain a suitable basis set, one can orthormalise the functions $|\tilde{\chi}_{\underline{k}m}\rangle$ to true Wannier functions $|w_{\underline{k}m}\rangle$:

$$|w_{\underline{k}m}\rangle = \sum_{m'} S_{m'm}(\underline{k})\,|\tilde{\chi}_{\underline{k}m'}\rangle \tag{2.96}$$

Therefore, the orthonormalisation matrix $\underline{\underline{S}}(\underline{k})$ is the inverse square root of the overlap matrix $\underline{\underline{O}}(\underline{k})$:

$$\underline{\underline{S}}(\underline{k}) \equiv \big(\underline{\underline{O}}(\underline{k})\big)^{-\frac{1}{2}} \tag{2.97}$$

Technically, $\underline{\underline{S}}(\underline{k})$ can be evaluated by diagonalising $\underline{\underline{O}}(\underline{k})$, computing the inverse square root of the eigenvalues and rotating the result back to the original basis. Comparing with (2.89), it is appropriate to define the following normalised projection matrices:

$$\begin{aligned} P_{m\nu}(\underline{k}) &\equiv \sum_{m'} S_{mm'}(\underline{k})\,\tilde{P}_{m'\nu}(\underline{k}) = \sum_{m'} S_{mm'}(\underline{k})\,\langle\chi_{\underline{k}m'}|\psi_{\underline{k}\nu}\rangle \\ P^*_{\nu m}(\underline{k}) &= \sum_{m'} S_{m'm}(\underline{k})\,\tilde{P}_{\nu m'}(\underline{k}) = \sum_{m'} S^*_{m'm}(\underline{k})\,\langle\psi_{\underline{k}\nu}|\chi_{\underline{k}m'}\rangle \end{aligned} \tag{2.98}$$

Due to the orthonormalisation, a unitarity relation can be found:

$$\big(\underline{\underline{P}}(\underline{k})\cdot\underline{\underline{P}}^\dagger(\underline{k})\big)_{mm'} = \sum_{\nu} P_{m\nu}(\underline{k})\cdot P^*_{\nu m'}(\underline{k}) = \delta_{mm'} \tag{2.99}$$

However, $\underline{\underline{P}}(\underline{k})$ cannot be denoted as unitary, since it is in general not quadratic. In particular, the transpose of (2.99) is not valid:

$$\underline{\underline{P}}^{\dagger}(\underline{k}) \cdot \underline{\underline{P}}(\underline{k}) \neq \underline{\underline{1}} \tag{2.100}$$

An exception to this is the case of quadratic projections, in which $\mathcal{C}$ and $\mathcal{W}$ have the same size. In this case, the projection matrices are really unitary, so that the validity of (2.100) follows directly from (2.99).

In summary, by inserting (2.98) into (2.89), the following expression is obtained for the local Green's function that enters DMFT in the projection onto localised orbitals formalism:

$$G^{\mathrm{loc}}_{mm'}(\mathrm{i}\omega_n) = \sum_{\underline{k}} \sum_{\nu\nu'} P_{m\nu}(\underline{k}) \cdot G^{\mathrm{bl}}_{\nu\nu'}(\underline{k}, \mathrm{i}\omega_n) \cdot P^{*}_{\nu' m'}(\underline{k}) \tag{2.101}$$

The Bloch Green's function $G^{\mathrm{bl}}_{\nu\nu'}(\underline{k}, \mathrm{i}\omega_n)$ occuring therein is defined as follows:

$$G^{\mathrm{bl}}_{\nu\nu'}(\underline{k}, \mathrm{i}\omega_n) = \left(\left[(\mathrm{i}\omega_n + \mu)\, \underline{\underline{1}} - \underline{\underline{\epsilon}}_{\underline{k}} - \Delta \underline{\underline{\Sigma}}^{\mathrm{bl}}(\underline{k}, \mathrm{i}\omega_n) \right]^{-1} \right)_{\nu\nu'} \tag{2.102}$$

$\Delta \underline{\underline{\Sigma}}^{\mathrm{bl}}(\underline{k}, \mathrm{i}\omega_n)$, which is the self-energy upfolded to Bloch space, is calculated from the impurity self-energy of DMFT according to (2.90):

$$\Delta \Sigma^{\mathrm{bl}}_{\nu\nu'}(\underline{k}, \mathrm{i}\omega_n) = \sum_{mm'} P^{*}_{\nu m}(\underline{k}) \left[\Sigma^{\mathrm{imp}}_{mm'}(\mathrm{i}\omega_n) - \Sigma^{\mathrm{dc}}_{mm'} \right] P_{m'\nu'}(\underline{k}) \tag{2.103}$$

Note that, due to (2.100), quantities from the small correlated subspace $\mathcal{C}$, in general, cannot be upfolded to the Bloch space $\mathcal{W}$, except for the quadratic case and, by construction, for self-energies. This requires that all relevant observables, like spectral functions or charge densities, have to be calculated directly in the Bloch space $\mathcal{W}$, e. g. from the Bloch Green's function $G^{\mathrm{bl}}_{\nu\nu'}(\underline{k}, \mathrm{i}\omega_n)$. This includes the chemical potential, which is calculated from $G^{\mathrm{bl}}_{\nu\nu'}(\underline{k}, \mathrm{i}\omega_n)$ for the total number of electrons in all bands of $\mathcal{W}$. This allows the subspace $\mathcal{C}$ to have

a larger total occupation than one would expect in a more straightforward Wannier function formalism. Details on how to adjust the chemical potential can be found in section 4.3.

Finally, if the projection matrices are quadratic (and only in this case), they have an inverse matrix (which is simply the Hermitian conjugate due to unitarity). Therefore, (2.101) can be cast into a shape that is identical to the more common definition (2.55):

$$\begin{aligned}
\underline{\underline{G}}^{\mathrm{loc}}(\mathrm{i}\omega_n) &= \sum_{\underline{k}} \left(\underline{\underline{P}}^{\dagger}(\underline{k})\right)^{-1} \cdot \underline{\underline{G}}^{\mathrm{bl}}(\underline{k}, \mathrm{i}\omega_n) \cdot \left(\underline{\underline{P}}(\underline{k})\right)^{-1} \qquad (2.104)\\
&= \sum_{\underline{k}} \left(\underline{\underline{P}}(\underline{k}) \left[(\mathrm{i}\omega_n + \mu)\,\underline{\underline{1}} - \underline{\underline{\epsilon}}_{\underline{k}} - \Delta\underline{\underline{\Sigma}}^{\mathrm{bl}}(\underline{k}, \mathrm{i}\omega_n)\right] \underline{\underline{P}}^{\dagger}(\underline{k})\right)^{-1}\\
&= \sum_{\underline{k}} \left[(\mathrm{i}\omega_n + \mu)\,\underline{\underline{1}} - \underline{\underline{P}}(\underline{k})\,\underline{\underline{\epsilon}}_{\underline{k}}\,\underline{\underline{P}}^{\dagger}(\underline{k}) - \underline{\underline{\Sigma}}^{\mathrm{imp}}(\mathrm{i}\omega_n) + \underline{\underline{\Sigma}}^{\mathrm{dc}}\right]^{-1}
\end{aligned}$$

So, for the quadratic case, one obtains an expression in which the projected energy eigenvalues $\underline{\underline{P}}(\underline{k})\,\underline{\underline{\epsilon}}_{\underline{k}}\,\underline{\underline{P}}^{\dagger}(\underline{k})$ formally play the role of the kinetic Hamilton operator $\underline{\underline{H}}^{\mathrm{kin}}(\underline{k})$.

Choice of $|\chi_{\underline{k}m}\rangle$ for the PAW formalism

Up to this point, the question has been left open how the functions $|\chi_{\underline{k}m'}\rangle$ are chosen. The requirements for these are in principle similar to the direct formulation in terms of Wannier functions, namely they should form a suitable basis that is capable of capturing most of the spectral weight near the Fermi level. The systems in question are typically characterised by rather localised d-orbitals (for instance), which are similar to the original atomic wave functions. Such atomic-like wave functions are contained in almost every state-of-the-art basis set for the Kohn-Sham wave functions. Here, the choices that are actually used for this work shall be presented, namely for the PAW and the MBPP formalisms. To begin with, the unnormalised projection matrices (2.92) can be written as follows in the PAW formalism by

inserting into (2.26):

$$\tilde{P}_{m\nu}(\underline{k}) = \langle \chi_m | \psi_{\underline{k}\nu} \rangle = \langle \chi_m | \tilde{\psi}_{\underline{k}\nu} \rangle + \sum_i \left(\langle \chi_m | \phi_i \rangle - \langle \chi_m | \tilde{\phi}_i \rangle \right) \langle \tilde{p}_i | \tilde{\psi} \rangle \tag{2.105}$$

A first assumption that one can make is that the functions $|\chi_m\rangle$ are localised entirely inside the augmentation spheres, which is motivated by current implementations of the LDA+U method [BABH00,AJT08]. Therefore, inserting (2.25) yields the following simplification:

$$\tilde{P}_{m\nu}(\underline{k}) = \sum_i \langle \chi_m | \phi_i \rangle \langle \tilde{p}_i | \tilde{\psi} \rangle \tag{2.106}$$

Thus, it is a suitable choice to use a linear combination of the partial wave functions $|\phi_i\rangle$ for the functions $|\chi_m\rangle$, since they have the desired properties and the formalism becomes extremely simple with this choice. Which linear combination to choose is, of course, a question of the physical system at hand. In rare occasions, it is already sufficient to use directly a subset of the $|\phi_i\rangle$, for instance those that belong to the bound $l = 2$ states. Alternatively, a rotation thereof can be done, as demonstrated in chapter 5, or even a superposition of different angular momenta, which might be useful e. g. for the description of hybrid orbitals. Furthermore, the matrix elements $\langle \tilde{p}_i | \tilde{\psi} \rangle$ are a quantity that is used frequently in the PAW formalism, for example for the calculation of densities of states, and can thus be obtained very easily.

Choice of $|\chi_{\underline{k}m}\rangle$ for the MBPP formalism

The mixed-basis pseudopotential formalism comprises a mixed basis of plane waves and localised functions, as shown in (2.37), whereas the latter are constructed according to (2.39). Thus, they similarly represent atomic-like orbitals and a linear combination thereof can serve as functions $|\chi_{\underline{k}m}\rangle$. (For the particular choice of the linear combination, the same ideas as for the PAW formalism apply.) With this idea, the

unnormalised projection matrices become a linear combination of the following matrix elements:

$$\tilde{P}_{\{\mu lm\}\nu}(\underline{k}) = \langle \phi^{\underline{k}}_{\mu lm} | \psi_{\underline{k}\nu} \rangle = \sum_{\underline{G}} \psi^{\underline{G}}_{\underline{k}\nu} \langle \phi^{\underline{k}}_{\mu lm} | \underline{k} + \underline{G} \rangle + \beta^{\underline{k}\nu}_{\mu lm} \tag{2.107}$$

The first index thereof is a combined index of atomic index μ and angular momentum and magnetic quantum numbers l and m; the symbol $|\underline{k} + \underline{G}\rangle$ stands for plane waves:

$$\langle \underline{r} | \underline{k} + \underline{G} \rangle = \frac{1}{\sqrt{\Omega_{\mathrm{C}}}} \mathrm{e}^{\mathrm{i}(\underline{k}+\underline{G})\underline{r}} \tag{2.108}$$

The scalar product $\langle \phi^{\underline{k}}_{\mu lm} | \underline{k} + \underline{G} \rangle$ is similarly a quantity that occurs frequently in the formalism and is calculated via a radial integration.

2.3.3 Double Counting

As mentioned, a severe problem of the interface construction between LDA and many-particle methods is that the Kohn-Sham orbitals do, by construction, already take into account a significant part of the electronic correlations that would also result from the explicit many-particle methods. This "double counting" problem should not be underestimated, a recent study thereof [KUW+10] has shown that the different approaches to "solve" the problem can actually lead to qualitatively different results. One could classify the problem as "unsolvable", because a diagrammatic expansion of LDA and thus an exact formulation of which correlations are double-counted does not exist. Anyway, the idea not to use LDA but rely on a formalism of which an exact diagrammatic representation is known, such as Hartree-Fock, shall not be considered, since this would mean to have a much worse description of electronic correlations for the orbitals that are not part of the correlated subspace. More sophisticated approaches, such as GW+DMFT, seem to be promising [TKP+12], but are computationally very demanding.

In the context of double counting, one has to keep in mind that the interaction parameters U and J are only effective parameters. So, apart from screening effects, they differ from the bare Coulomb repulsion of the electrons also due to an implicit double counting correction. In line with that, similar interaction parameters for e. g. a Hartree-Fock+DMFT-based approach would be significantly larger than for LDA+DMFT. Apart from these implicit ideas, state-of-the-art double counting correction approaches basically introduce a shift $\underline{\underline{\Sigma}}^{\mathrm{dc}}$ between the orbitals of the correlated subspace and the remaining orbitals, which can be seen in (2.103). Note that such a shift, assuming $\underline{\underline{\Sigma}}^{\mathrm{dc}}$ to be a multiple of the unity matrix, will merely result in a shift of the chemical potential μ (and in the total energy of the formalism) if an explicit basis like the maximally localised Wannier functions is used or if the projection matrices are quadratic. Some ways to find suitable guesses for $\underline{\underline{\Sigma}}^{\mathrm{dc}}$ are sketched here, following [Lec03].

Fully Localised Limit (FLL)

The fully localised limit (FLL) [ASK+93, CdzS94, SDA94] is the most frequently used double counting correction approach in this work. It has originally been developed for the LDA+U method, which corresponds to the static mean-field solution of the Hubbard model. The idea of the FLL is that the LDA solution corresponds to the fully localised solution of the Hubbard model, i. e. no itinerant contribution to the energy exists. This might, at first glance, sound counter-intuitive, but relies on the observation that the total energy of the atomic limit of a system is usually described by LDA reasonably well. Thus, the FLL is often used for insulating systems close to the atomic limit. As it can easily be checked, this limit has the following energy in the static mean-field solution without non-density-density contributions:

$$E^{\mathrm{FLL}} = \frac{U}{2} \sum_{\mu} n_{\mu} \left(n_{\mu} - 1 \right) - \frac{J}{2} \sum_{\mu\sigma} n_{\mu\sigma} \left(n_{\mu\sigma} - 1 \right) \tag{2.109}$$

In this equation, $n_{\mu\sigma}$ is the sum of the diagonal elements of the orbital (m) occupation number matrix $n^{\mu\sigma}_{mm'}$ per atom μ and spin component σ:

$$n_{\mu\sigma} = \sum_m n^{\mu\sigma}_{mm} \tag{2.110}$$

n_μ is the spin-summed counterpart thereof:

$$n_\mu = \sum_\sigma n_{\mu\sigma} \tag{2.111}$$

Just for clarification, it shall be mentioned that in both cases these are really sums and not averages, so for instance $n_\mu = 2 \cdot n_{\mu\sigma}$ is valid in the paramagnetic case.

So the idea of the double counting correction (in the LDA+U framework) is to substract a suitable potential which reproduces this energy contribution for each atom μ. For LDA+DMFT, this potential is written as the self-energy shift $\underline{\underline{\Sigma}}^{\mathrm{dc}}$ as follows:

$$\Sigma^{\mathrm{FLL}}_{\mu\sigma,mm'} = \delta_{mm'} \left[U \left(n_\mu - \frac{1}{2} \right) - J \left(n_{\mu\sigma} - \frac{1}{2} \right) \right] \tag{2.112}$$

It is important to note that, in DMFT or RISB, E^{FLL} is not exactly the energy shift that one would obtain due to the double counting correction term, this is only valid for the static mean-field case of LDA+U. Therefore, the actual calculation of the double counting correction energy is realised in a different way, as shown in section 4.5.

Around Mean Field (AMF)

A similar idea from the original work about the LDA+U framework [AZA91] has lead to the around mean field (AMF) approximation to the double counting problem. The idea thereof is to stress the mean-field character of LDA by assuming that LDA corresponds to a solution in which the occupation numbers $n^{\mu\sigma}_{mm'}$ are diagonal and completely orbital-independent, thus taking an orbital-averaged value.

This might sound more intuitive than the FLL, but is, of course, still a heavy approximation since LDA does take into account effects like crystal field splitting. According to [CdzS94], this approximation corresponds to the following static mean-field energy, using the definitions from the FLL and assuming a total number of $2l+1$ orbitals per atom:

$$E^{\mathrm{AMF}} = \frac{U}{2} \sum_{\mu} \left(n_{\mu}\right)^2 - \frac{1}{2l+1} \sum_{\mu\sigma} \left(\frac{U}{2} + lJ\right) \left(n_{\mu\sigma}\right)^2 \tag{2.113}$$

This energy is, again not exactly, modeled by the following self energy shift:

$$\Sigma^{\mathrm{AMF}}_{\mu\sigma,mm'} = \delta_{mm'} \left[U n_{\mu} - \frac{1}{2l+1}(U + 2lJ) n_{\mu\sigma} \right] \tag{2.114}$$

So although the initial idea of AMF compared to FLL is completely different, both approaches yield comparable results. The difference of the two self-energy shifts is:

$$\Sigma^{\mathrm{AMF}}_{\mu\sigma,mm'} - \Sigma^{\mathrm{FLL}}_{\mu\sigma,mm'} = \delta_{mm'} \left(U - J\right) \left(\frac{n_{\mu\sigma}}{2l+1} - \frac{1}{2} \right) \tag{2.115}$$

So the difference between AMF and FLL vanishes for half-filled systems and takes its maximum value of $U - J$ for completely filled or completely empty systems.

Fixing local charges

Another double counting correction idea [ALG+08] that does not originate from LDA+U is to assume that correlation effects as described by DMFT do not affect the total occupation of the local impurity Green's function (2.101). For this purpose, one can define the following impurity Green's function of the uncorrelated system by setting the self-energy to zero:

$$G^{\mathrm{loc},0}_{mm'}(\mathrm{i}\omega_n) = \sum_{\underline{k}} \sum_{\nu\nu'} P_{m\nu}(\underline{k}) \cdot \left(\left[(\mathrm{i}\omega_n + \mu) \underline{\underline{1}} - \underline{\underline{\epsilon}}_{\underline{k}} \right]^{-1} \right)_{\nu\nu'} \cdot P^*_{\nu' m'}(\underline{k}) \tag{2.116}$$

The total occupation thereof corresponds to the Matsubara frequency sum of its trace. Therefore, the double-counting correction is realised by ensuring the following condition:

$$\sum_{mn} G^{\mathrm{loc},0}_{mm}(\mathrm{i}\omega_n) = \sum_{mn} G^{\mathrm{loc}}_{mm}(\mathrm{i}\omega_n) \tag{2.117}$$

So the self-energy shift $\underline{\underline{\Sigma}}^{\mathrm{dc}}$ is not calculated directly in this approach, but becomes an additional variational parameter of the DMFT self-consistency loop.

Three

A first materials application: Vanadium Chalcogenides

Before turning to new formal developments, an example kind of problem that can be tackeled with the methods described above shall be investigated in detail. In short, the Vanadium chalcogenides $BaVS_3$ and $BaVSe_3$ are compared. They will be seen to show an overall (surprisingly) similar behaviour. However, the experimentally determined low-temperature ordering, which is attributed to strong electronic correlations, is substantially different. $BaVS_3$ shows a metal-insulator-transition that can be attributed to a charge-density-wave instability, while $BaVSe_3$ remains metallic down to low temperatures. Some subtle differences that may lead to this varying behaviour are shown in the following section. The data shown therein is published in [GBL10].

3.1 Introduction to experimental findings

Barium Vanadium trisulfide ($BaVS_3$) has been subject to several experimental as well as theoretical investigations since its first synthesis, which has been reported in 1969 [GVW69]. It stems from a group of compounds of type ABX_3, thus, its high-temperature arrangement

is isostructural to, e. g., $BaTiS_3$, $BaTiSe_3$, $SrTiS_3$, $BaTaS_3$ and, of course most important for this work, $BaVSe_3$. In the hexagonal high-temperature phase (space group: $P6_3/mmc$), the Vanadium (or, more generally, B) ions form continuous chains along the crystallographic c-direction and are octahedrally encompassed by sulfur (or X) ions. This chain structure, in which the interchain distance is more than twice the intrachain distance, already gives a hint on the manifestly one-dimensional structure of this compound. With decreasing temperature, $BaVS_3$ undergoes several continuous phase transitions. The first one takes place at $T_S \sim 240$ K and is a pure structural transition that slightly distorts the original chain structure in the ab plane to a 'zig-zag' arrangement [SGCM82]. The resulting crystal structure has orthorombic symmetry (space group: $Cmc2_1$). Furthermore, the transition that motivates this work takes place at $T_{MIT} \sim 70$ K. It comprises a metal-insulator transition and an orthorombic-to-monoclinic structural transition with a doubling of the original unit cell and a small discontinuity of the lattice parameters [SGCM82]. The third and last transition that can be observed in this material is a pure magnetic transition to its incommensurate antiferromagnetic (Néel) ground state at $T_N \sim 30$ K [NYG$^+$00].

Although the unusual magnetic ground state has attracted some attention in the past as well, the present comparison focuses on the metal-insulator-transition and all calculations are paramagnetic. The starting point is the work by F. Lechermann and coworkers [LBG05, LGP$^+$06, LBG07], which investigates the different aspects of this transition. Strong evidence exists that the insulating phase results from a charge-density-wave instability [IOK$^+$02, FFLR$^+$03]. In brief, charge-density waves can be thought of as one-dimensional modulations of the electronic charge density which results in the opening of a band gap. Without going too far into details of the mechanism, the principal ingredient that is required for its formation is a suitable Fermi surface structure that allows for the "nesting" of a one-dimensional superstructure commensurate with the original lattice structure (but not necessarily obeying the same symmetry operations). Thus, one has to

find parallel Fermi surface sheets such that a lattice vector has to be an integer multiple of their distance vector. In $BaVS_3$, the nesting condition has been determined experimentally to be [FFLR+03]:

$$2\underline{k}_{\mathrm{F}} = 0.5 \cdot \underline{c}^* \tag{3.1}$$

Here, $\underline{c}^*$ is the reciprocal lattice vector corresponding to the crystallographic c-direction. The charge-density wave is thus realised due to the significant quasi-one-dimensional lattice structure in c-direction and has a periodicity of two original unit cells.

As mentioned, Barium Vanadium triselenide ($BaVSe_3$) has overall very similar properties to the sulfide compound. Its hexagonal high-temperature phase has been found to be isostructural to the sulfide compound on the occasion of its first synthesis in 1979 [KJA+79], including the quasi-one-dimensional Vanadium chain arrangement. Also the small continuous structural distortion towards orthorombic symmetry at $T_{\mathrm{S}} \sim 290$ K has been reported therein. However, the low-temperature ordering is fundamentally different. Especially, no insulating phase and related doubling of the unit cell has been found. In this respect, $BaVSe_3$ appears to be similar to $BaVS_3$ under high pressure, where the CDW onset is equally supressed [FGB+00], thus raising the question whether $BaVSe_3$ can be understood as a high-pressure analogon of $BaVS_3$, which would mean that the selenium atoms (isovalent to, but larger than sulfur) lead to "chemical" pressure. Furthermore, the low-temperature magnetic ordering has been found to be ferromagnetic in $BaVSe_3$ below a transition temperature of $T_{\mathrm{X}} \sim 43$ K [YGNS01].

Since especially the charge-density-wave low-energy ordering of $BaVS_3$ is, of course, related to strong electronic correlations, the focus of this work is the detailed comparison of the two materials in the phase prior to the transition, looking for differences that could give hints about the absence of the CDW onset in $BaVSe_3$. As mentioned, the magnetic ordering is not supposed to be taken into account explicitly due to the significantly increasing complexity. Magnetic ordering tendencies are in this respect believed not to be significant for

the metal-insulator-transition in question, but also give a hint that explicit electronic correlations are mandatory for both systems.

3.2 Density functional theory considerations

Before putting explicit many-body techniques into play, one has to carefully consider what information already "standard" density functional theory can provide. The focus is on the orthorombic $Cmc2_1$ phase prior to the CDW formation, which can be directly compared between the two materials. To begin with, some technical details of these calculations are listed.

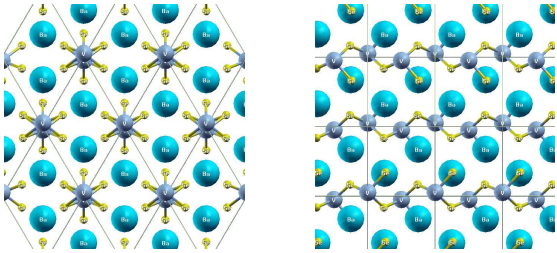

Figure 3.1: Crystal structure of the orthorombic phase of $BaVSe_3$ seen along the z-axis (left), i.e. in Vanadium chain direction, and along the x-axis (right). The zig-zag distortion of the Vanadium chains, the difference of intra-chain and inter-chain Vanadium distance and the coordination of Vanadium atoms by Selenium atoms is visible.

The crystal structure, visualised in figure 3.1, is built from a unit cell containing two formula units of $BaVS_3$ or $BaVSe_3$, respectively. For $BaVS_3$, detailed experimental structural data is known from neutron diffraction or X-ray diffraction studies [GAC+86], whereas the former is used in these calculations. For $BaVSe_3$, the situation turns out not to be as simple, no structural refinement has been found in

	$BaVS_3$	$BaVSe_3$
a	12.77	13.34
b	21.71	22.68
c	10.58	11.06

Table 3.1: Lattice parameters that are used for all calculations of $BaVS_3$ and $BaVSe_3$. All values are given in atomic units.

literature. Therefore lattice parameters that stem from a similar calculation that has been done shortly before this work by Akrap and coworkers [ASacH$^+$08] are used. All lattice parameters are summarised in table 3.1. Also here, note the small values of c (compared to a), again hinting to the quasi-one-dimensionality of the crystal lattice structure. The parameter b given in the table would be $\sqrt{3} \cdot a$ in the hexagonal structure and differs slightly from this value due to the orthorombic distortion. The exact atomic positions (i. e. the ionic displacement due to the zig-zag orthorombic distortion) for $BaVSe_3$ have been found by relaxation within the MBPP code that is used for all further calculations. It turns out that the obtained relative distortion of 0.025 for $BaVSe_3$ is slightly larger than the value of 0.021 for $BaVS_3$ from diffraction experiments, which could be a first hint onto a less-pronounced quasi-one-dimensional behaviour of the selenide compound. However, one could argue that correlation effects might also influence this value, which could be in principle included into the calculation using the methods developed in the later chapters. However, this is not done because of the huge numerical effort that would be required. In total, both numbers are reasonably small and a large influence onto the electronic structure is not expected, and has not been seen from the direct comparison to the hexagonal phase.

All calculations are done using an LDA approximation to DFT parametrised by Perdew and Wang [PW92]. Concerning the k-point grid used to sample the first Brillouin zone, a Monkhorst-Pack grid [MP76] of $7\times7\times7$ points has been found to be sufficient, resulting in 64

k-points in the irreducible wedge of the Brillouin zone (i. e. all other k-points can be found using symmetry operations). The improved tetrahedron method [BJA94] is used for the Brillouin zone integration of the total energy and the occupation numbers. A plane-wave energy cutoff of $E_{\mathrm{PW}} = 20$ Ryd has been chosen and localised functions are used for $l = 0$ and $l = 1$ on each atom and, additionally, $l = 2$ for Vanadium, the latter with a cutoff radius of 2.0 atomic units.

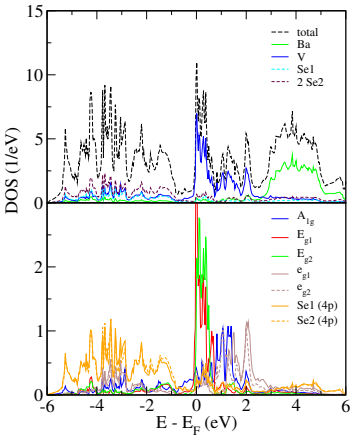

Figure 3.2: LDA density of states of $BaVSe_3$.

As a first DFT result, figure 3.2 shows the density of states of the LDA one-particle wave functions for the selenide compound $BaVSe_3$. The first thing that becomes obvious is that the system is described to be metallic, which also holds true for the sulfide compound. In the upper panel of figure 3.2, besides the total density of states, contributions inside of spheres around the respective atomic positions are depicted. It can be seen that the states at the Fermi level are localised on the Vanadium atoms. This corresponds to simple chemical considerations: Assuming Se^{2-} and Ba^{2+} configurations, the Vanadium atoms would formally be in a V^{4+} state. This corresponds to

one electron in the localised and thus strongly correlated Vanadium 3d-states. Accordingly, the selenium states below the Fermi level are filled and the barium states above are empty. The six selenium atoms per unit cell form shells of two (denominated Se1 in the figure) and four (Se2) atoms which are inequivalent due to the orthorombic distortion. The lower panel of figure 3.2 shows projections of the density of state onto cubic harmonics centred on the respective atomic positions. As expected, the selenium states below the Fermi level stem from 4p orbitals. The 3d contributions of the Vanadium atoms (which are all equivalent by symmetry) are resolved by magnetic quantum number. They show a behaviour that can be observed frequently in transition metal oxides and similar compounds (including sulfides and selenides): The 3d orbitals that would be degenerate for isolated atoms seperate into states that can be named by the Mulliken symmetry labels t_{2g} and e_g due to ligand field splitting, i. e. triply and doubly degenerate states. They can be visualised as pointing towards (e_g) and between (t_{2g}) the neighbouring selenium atoms. It can be seen that only the t_{2g} states carry weight near the Fermi level and thus are responsible for the low-energy physics of the system, while the e_g states are lifted in energy. The t_{2g} states further split into a nondegenerate A_{1g} (pointing in Vanadium chain direction) and a doubly degenerate E_g (perpendicular to the Vanadium chains). The orthorombic distortion leads to a further (small) splitting of the E_g and e_g manifold, since the neighbouring selenium atoms are inequivalent. Therefore, this splitting is not observed in the hexagonal phase. In a slightly sloppy (not Mulliken-like) way, these states are denoted as E_{g1}, E_{g2}, e_{g1} and e_{g2}.

Figure 3.3 contains the comparison of the LDA one-particle band structures of $BaVS_3$ and $BaVSe_3$. The overlap of the respective band wave function with the orbitals from the t_{2g} manifold is shown via the coloured broadening, thus depicting to which orbital character the band in question primarily corresponds. Note that, like in the density-of-states-plot above, A_{1g}, E_{g1} and E_{g2} do not correspond directly to cubic harmonics, but are rotated into a basis that diagonalises their occupation matrix, typically referred to as crystal field basis. The

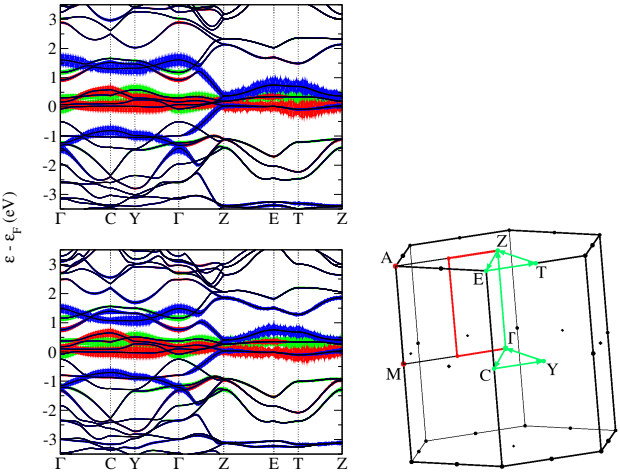

Figure 3.3: Left: LDA band structure of $BaVS_3$ (top) and $BaVSe_3$ (bottom). The weight of the individual orbitals of the t_{2g} manifold on the bands is visualised by the coloured broadening of the bands (blue: A_{1g}, red: E_{g1}, green: E_{g2}). Right (from [LBG07]): Brillouin zone of the orthorhombic structure, visualising the path chosen for the band structure plot in green.

first thing that one gets aware of is the striking similarity of the two materials in this level of comparison. However, a few subtle (but important) differences are immediately obvious. The first one is related to the bandwidth of the set of bands corresponding to the t_{2g} manifold, which is slightly reduced in the selenide (from about 2.7 eV to about 2.4 eV). This effect can principally be attributed to the larger distance between two neighbouring Vanadium atoms in the selenide compound, resulting in a smaller orbital overlap, or, transformed to reciprocal space, in a smaller bandwidth. A second difference is related to the Sulfur/Selenium bands below the t_{2g} manifold, which is smaller in the selenide compound, which can be seen especially at the Γ-point.

This may hint towards a stronger hybridisation of the Vanadium and Selenium bands than of Vanadium and Sulfur. Such a hybridisation typically results in enhanced screening of the bare Coulomb repulsion of the electrons located at the Vanadium atoms, which thus implies a smaller Hubbard model interaction parameter U or, in other words, a more weakly correlated behaviour.

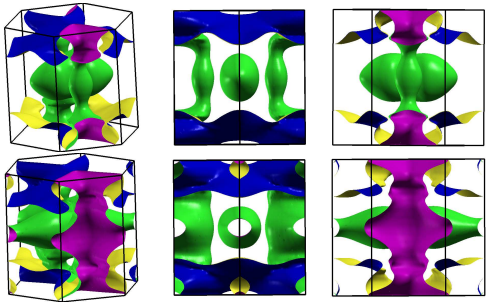

Figure 3.4: LDA Fermi surfaces of $BaVS_3$ (top) and $BaVSe_3$ (bottom) from different perspectives.

As mentioned above, it is essential for the present studies of the possible onset of a charge density wave to look at Fermi surfaces and possible nesting scenarios therein. The LDA one-particle Fermi surfaces of both systems are compared in figure 3.4. It is evident that the nesting condition given in (3.1) cannot be fulfilled for both materials from the LDA viewpoint, hinting towards the importance of strong electronic correlations. However, the surprising result of this consideration is that the selenide compound appears to be even closer to fulfill the nesting condition than the sulfide compound: Looking at the blue moustache-like Fermi sheet structures seen especially in the right column of figure 3.4, one notices that these appear flatter in the selenide compound and have almost the correct distance to each other (half the size of the Brillouin zone). However, this picture will change as more electronic correlations are added.

3.3 Extracting a correlated subspace

The next step that is necessary to be able to do an LDA+DMFT calculation is the extraction of a suitable small correlated subspace. This is done in terms of maximally localised Wannier functions as described in section 2.3.1. Obviously, the correlated subspace shall describe mainly the low-energy physics of the system, which is clearly dominated by the above-mentioned t_{2g} manifold, containing three orbitals per Vanadium atom, thus six per unit cell. Of course, there is no direct way to force the Wannier construction to represent these t_{2g} orbitals; this has to be done implicitly. The first thing to note is that there is no gap between the spectral region corresponding to the t_{2g} manifold and the e_g or Sulfur/Selenium states, the bands are entangled, so that a disentanglement procedure is put into practice. However, an inner ("frozen") window can be used that only contains exactly the six t_{2g}-like bands to be reconstructed, so that the original dispersion is exactly reproduced by the dispersion of the Wannier functions in this window. This inner window ranges from approximately 0.14 eV below to 0.74 eV above the Fermi energy for the selenide compound and from 0.45 eV below to 0.91 eV above the Fermi energy for the sulfide compound (remember the smaller bandwidth and the stronger hybridisation towards the selenium bands). Furthermore, the t_{2g} orbitals are provided as initial guesses for the Wannier functions. In total, 15 bands are used as input for the Wannier construction.

Figure 3.5 shows a visualisation of the three maximally localised Wannier functions that are attributed to the first Vanadium atom by an isosurface representation in which the xz-plane is visible. One can clearly distingiush the A_{1g}-like function pointing towards the neighbouring Vanadium atom from the functions pointing between the neighbouring Selenium atoms. It is obvious that all of the Wannier functions, as expected, do have finite contributions at the neighbouring atoms, thus they cannot be thought of as simple d-like atomic eigenfunctions.

Figure 3.6 shows the dispersion relation of the maximally localised

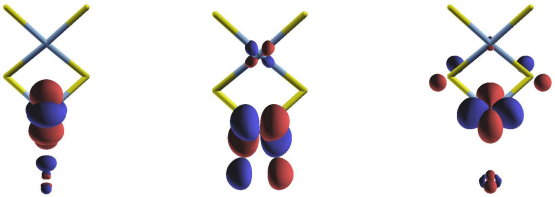

Figure 3.5: Visualisation of three maximally localised Wannier functions obtained for $BaVSe_3$.

Wannier functions that are obtained. Outside the inner window, it can be seen that the Wannier bands extrapolate the original band structure, capturing the jumps of spectral t_{2g} weight from one band to another reasonably well. One can identify four bands with small bandwidth, representing the E_g orbitals from the t_{2g} manifold, and two bands that are dispersive mainly in the Γ-Z path through the Brillouin zone (roughly the Vanadium chain direction), thus representing the quasi-one-dimensional character of the original A_{1g} orbitals. Thus the interplay between itinerant and localised character of the two sub-manifolds as well as the quasi-one-dimensional features of the dispersion relation are well reproduced by this rather simple model construction.

It is important to note that the nesting between Fermi surface sheets does not necessarily take place along a high-symmetry line. For this reason, the low-energy dispersion relation of the Wannier functions along a path containing a line from 'M/2' to 'A/2' (as defined in figure 3.3), which is an appropriate candidate for a possible nesting scenario, is shown in figure 3.7. Although the overall structure again looks very similar for the compounds in question, one can find another important difference: Focusing especially on the band crossing the 'M/2' point around -1.0 eV, one can see that it has large weight on E_{g1} and A_{1g} in the selenide compound, whereas the A_{1g} weight more clearly dominates in the sulfide compound. Such hints also show up

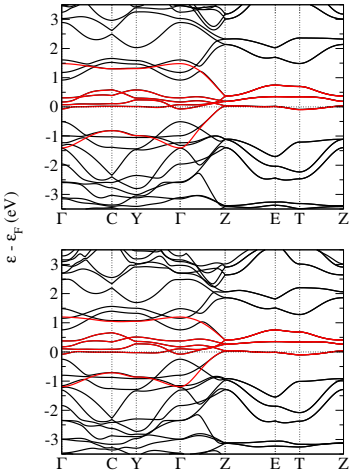

Figure 3.6: Red: Maximally localised Wannier functions dispersion relation obtained for $BaVS_3$ (top) and $BaVSe_3$ (bottom). Black: original LDA band structure.

at other points and can also be found in the band structure plot in figure 3.3. One can conclude that the hybridisation between A_{1g} and E_g is generally larger in the selenide compound, making a clear distinction of the bands as well as the respective Fermi surface sheets difficult. This finding also gives hints on the reduced quasi-one-dimensionality of the selenide.

3.4 Explicit many-body methods

The obtained maximally localised Wannier functions can now be used to express a suitable low-energy kinetic Hamilton operator $\underline{\underline{H}}^{\mathrm{kin}}(\underline{k})$. As a small simplification, this Hamilton operator is rotated (i. e. a unitary transformation is applied) so that the local part (i. e. the k-sum over the whole Brillouin zone) thereof is diagonal. In principle,

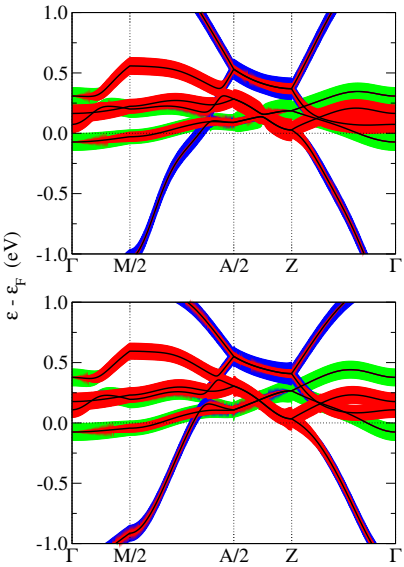

Figure 3.7: Wannier function dispersion relation broadened by the respective orbital overlap for $BaVS_3$ (top) and $BaVSe_3$ (bottom), drawn using a closed path through the first Brillouin zone that incorporates non-high-symmetry lines. The path and the respective points are defined and shown in red in figure 3.3. Color coding: A_{1g} (blue), E_{g1} (red) and E_{g2} (green).

this rotation countermands the maximal localisation slightly, so that, strictly speaking, a rotation of the interaction tensor U would also be in place. However, as the rotation turns out to be small and thus the motivation of the original U is still valid, this has not been done. Note that this rotation does not imply that the resulting many-particle self energies are diagonal, they are seen to have off-diagonal elements. This is a small complication for the many-body methods, as it can be a large numerical simplification if one can show that all self energies are

diagonal by e. g. symmetry arguments. However, this is not done here, and all of the applied many-body formalisms are capable of handling off-diagonal self energy matrix elements properly.

Since $\underline{\underline{H}}^{\mathrm{kin}}(\underline{k})$ still incorporates six bands, which is numerically too demanding to be treated with explicit many-particle methods, a further simplification has to be done: It is known that the two Vanadium atoms at which the orbitals in question are located are equivalent by symmetry. Thus all local quantities concerning these two atoms are equal (the directional dependencies can, of course, be different). In this spirit, the self energy (local due to the DMFT approximation) is only calculated once in a three-band model. The approximation behind this picture is that self-energy terms between the two atoms are neglected. Technically, this is done as follows for DMFT: The inversion shown in (2.55) is done using 6×6 matrices with a block-diagonal (two 3×3 blocks) self energy matrix (note that one-particle contributions between the two Vanadium atoms are thus taken into account explicitly). The construction of $\mathcal{G}_0$ is afterwards done only for a 3×3 matrix that results from averaging over two 3×3 blocks from $\underline{\underline{G}}^{\mathrm{loc}}$, which are identical up to numerical inaccuracies. For RISB, the idea is simply to build all relevant interaction-related matrices (like $\underline{\underline{R}}$ or $\underline{\underline{\Lambda}}$) in a block-diagonal way.

As the most intuitive first observable, figure 3.8 shows the occupation numbers of the correlated orbitals per atom summed over both spin channels from the hybridisation expansion CTQMC solution of DMFT and from RISB, for both the sulfide and the selenide compound. The CTQMC calculations have been done at a temperature of $T \sim 113$ K, or $\beta = (k_{\mathrm{B}}T)^{-1} = 100\ \mathrm{eV}^{-1}$, which is in the temperature range above the actual onset of the CDW in $BaVS_3$. (In its current implementation, RISB has no explicit temperature dependence.) The two-particle Hamilton operator that enters the Hubbard model is, if not stated otherwise, the general Hamilton operator given in (2.50) with the assumptions $U' = U - 2J$ and $J_{\mathrm{C}} = J$. In the bottom row of figure 3.8, the results obtained using this rotationally invariant Hamilton operator for the selenide compound are compared to the version

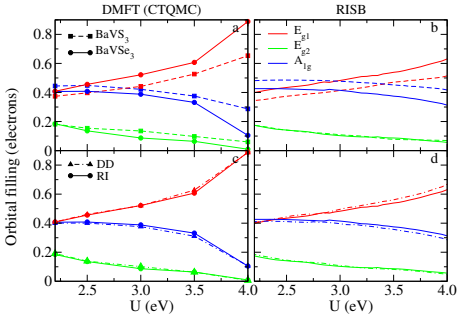

Figure 3.8: Orbital occupations of the effective t_{2g} manifold with increasing U, fixing J at 0.7 eV. The top row (plots (a) and (b)) compares the compounds $BaVS_3$ (dashed/squares) and $BaVSe_3$ (solid/circles). The second row (plots (c) and (d)) compares different types of interacting Hamilton operators for $BaVSe_3$ containing only density-density terms (dash-dotted/triangles) and including spin-flip and pair-hopping terms (solid/circles). Left column ((a) and (c)): CTQMC solution of DMFT; right column ((b) and (d)): RISB solution.

incorporating density-density interactions only, as shown in (2.51). The parameters U and J that appear therein are, of course, a priori unknown. Thus, to begin with and to get a qualitative understanding about the influence thereof, U is varied over a large parameter space, while J is kept fixed at $J = 0.7$ eV. The parameter space for U ranges from $U > 3J$ (to ensure that the electron-electron-interaction is repulsive) to a value slightly below the Mott metal-insulator transition, which is not observed experimentally in both systems. In contrast, a fixed value of J appears to be in order as J is in general less sensitive to the crystal environment.

To start with a more technical analysis, one can state that the qualitative features are equally well described by DMFT with CTQMC solver (left column of figure 3.8) and by RISB (right column), which in

a way justifies the use of RISB as a fast alternative to DMFT for larger phase-space scans. However, as expected, the actual numbers are slightly different. Furthermore, the influence of non-density-density interactions is very small in this paramagnetic setup and leads to a slightly smaller orbital polarisation, equally seen in both formalisms.

The overall evolution of the occupation numbers yields an effective two-orbital system, since the E_{g2} orbital is mostly empty for both systems and in almost the whole parameter range. The comparison of $BaVS_3$ and $BaVSe_3$, is, at first sight, surprising. In [LBG05] it is argued that the occupation inversion, i. e. the depletion of A_{1g} in line with increasing occupation of E_{g1} with increasing U (whereas A_{1g} has the largest occupation in pure LDA) gives a hint about the possible CDW nesting scenario in $BaVS_3$. However, this effect turns out to be even stronger in $BaVSe_3$. In this context, one has to remember the smaller bandwidth of the $BaVSe_3$ t_{2g} manifold. Experimental evidence for this behaviour is lacking, since occupation numbers are difficult to be related to experimentally accessible quantities.

Appropriate values of U and J to describe the physics of the systems at hand could not be determined ab initio in the present study. Instead, they are selected from physical arguments. The value of $U = 3.5$ eV used for $BaVS_3$ has been shown to describe the physics of the system well [LBG05]. As mentioned in section 3.2, a significantly smaller value can be expected for $BaVSe_3$. For this reason, $U = 2.5$ eV is chosen as a reasonable value for the selenide, while for direct comparability, results for $U = 3.5$ eV are also shown if appropriate. $J = 0.7$ eV is kept fixed for both materials, which is in line with the previous studies of $BaVS_3$ and other Vanadium compounds, e. g. [SHT96, BPLG05]. Figure 3.9 shows another output quantity of DMFT, namely the local spectral function for the selected interaction parameters, and its comparison to the one-particle density of states of the original LDA Wannier functions. The local spectral function is proportional to the imaginary part of Green's function for real frequencies. In order to obtain this function from the imaginary (Matsubara) frequency output of DMFT, an analytic continuation of the data has

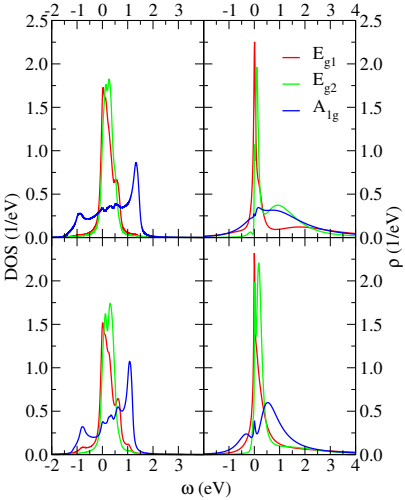

Figure 3.9: Density of states of the LDA Wannier functions (left) compared to local spectral functions from LDA+DMFT (right). Top row: $BaVS_3$ with $U = 3.5$ eV, bottom row: $BaVSe_3$ with $U = 2.5$ eV.

been done via Bryan's maximum entropy method [Bry90].

As mentioned, it is useful to compare the Fermi surfaces of the two materials in question in order to find evidence for a possible nesting scenario. In the context of many-body theories, Fermi surfaces can be understood in the quasi-particle picture. The quasi-particle excitation energies correspond to the poles of Green's functions on (or infinitesimally above) the real frequency axis. Since the low-energy part thereof is relevant to get Fermi surfaces, real frequency self energies are obtained via a Padé fit to the Matsubara self energies and the following linearisation, which is applicable for the low-energy physics of Fermi surfaces in question:

$$\Re\left[\underline{\underline{\Sigma}}(\omega + \mathrm{i}0^+)\right] \doteq \Re\left[\underline{\underline{\Sigma}}(0)\right] + (\underline{\underline{1}} - \underline{\underline{Z}}^{-1}) \cdot \omega \tag{3.2}$$

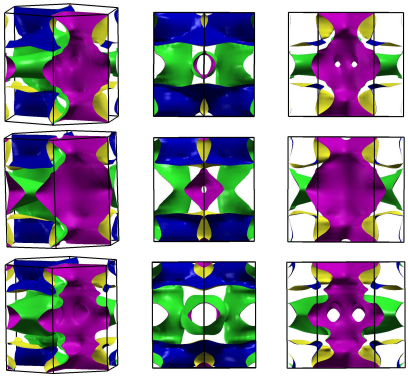

Figure 3.10: Correlated quasi-particle Fermi surfaces of $BaVS_3$ with $U = 3.5$ eV (top) and $BaVSe_3$ with $U = 3.5$ eV (middle) and $U = 2.5$ eV (bottom).

In this equation, $\underline{\underline{Z}}$ denotes the quasi-particle weight, which gives an intuitive measure of the quasi-particle content of the system, and is defined as follows:

$$\underline{\underline{Z}} := \left(\underline{\underline{1}} - \left. \frac{\partial \underline{\underline{\Sigma}}}{\partial \omega} \right|_{\omega=0} \right)^{-1} \tag{3.3}$$

The spectral representation of $\underline{\underline{G}}(\underline{k}, \omega)$ for real frequencies

$$\underline{\underline{G}}(\underline{k}, \omega) = \left[(\omega + \mu)\, \underline{\underline{1}} - \underline{\underline{H}}^{\mathrm{kin}}(\underline{k}) - \underline{\underline{\Sigma}}(\omega) \right]^{-1} \tag{3.4}$$

can be rewritten as follows by inserting (3.2) (assuming that $\underline{\underline{H}}^{\mathrm{kin}}(\underline{k})$ is real):

$$\begin{aligned} \Re \left[\underline{\underline{G}}(\underline{k}, \omega) \right] &\doteq \left[(\omega + \mu)\, \underline{\underline{1}} - \underline{\underline{H}}^{\mathrm{kin}}(\underline{k}) - \Re \left[\underline{\underline{\Sigma}}(0) \right] - (\underline{\underline{1}} - \underline{\underline{Z}}^{-1}) \cdot \omega \right]^{-1} \\ &= \underline{\underline{Z}} \cdot \left[\omega\, \underline{\underline{1}} + \underline{\underline{Z}} \left(\mu\, \underline{\underline{1}} - \underline{\underline{H}}^{\mathrm{kin}}(\underline{k}) - \Re \left[\underline{\underline{\Sigma}}(0) \right] \right) \right]^{-1} \end{aligned} \tag{3.5}$$

Thus, poles of $\Re \left[\underline{\underline{G}}(\underline{k}, \omega) \right]$ can occur for:

$$\det \left(\omega\, \underline{\underline{1}} + \underline{\underline{Z}} \left(\mu\, \underline{\underline{1}} - \underline{\underline{H}}^{\mathrm{kin}}(\underline{k}) - \Re \left[\underline{\underline{\Sigma}}(0) \right] \right) \right) = 0 \tag{3.6}$$

With (3.6), one can define a quasi-particle band structure of the interacting system. Likewise, the quasi-particle Fermi surface displays the features for $\omega = 0$ and can be found as follows:

$$\det\left(\mu\,\underline{\underline{1}} - \underline{\underline{H}}^{\mathrm{kin}}(\underline{k}) - \Re\left[\underline{\underline{\Sigma}}(0)\right]\right) = 0 \tag{3.7}$$

This shows that correlation effects, in this picture, can be understood to introduce an orbital-dependent shift (of magnitude $\Re\left[\underline{\underline{\Sigma}}(0)\right]$) to the original LDA Fermi surface. This answers the question about how an intrinsically k-independent quantity like the DMFT self energy can contribute to an intrinsically k-dependent quantity like the Fermi surface, namely via the k and orbital dependence of the original LDA Hamilton operator.

Figure 3.10 displays the Fermi surfaces of the LDA+DMFT formalism. It can be seen that, for $BaVS_3$ with the interaction parameters of [LBG05], a strong flattening of the Fermi surface sheets that are responsible for fulfilling the nesting condition (3.1) (the blue A_{1g}-related sheets) can be observed, thus making nesting possible, as demonstrated already in [LGP$^+$06]. For $BaVSe_3$, the value of $U = 2.5$ eV, which is believed to be realistic, is compared to $U = 3.5$ eV, as used for $BaVS_3$. It can be seen that, especially for $U = 2.5$ eV, the flattening of the respective Fermi surface sheets appears to be smaller, although it is of course difficult to give a quantitative measure thereof.

Figure 3.11 furthermore shows the renormalised band structure from (3.6) along the non-high-symmetry path shown in figures 3.7 and 3.3. From this plot, it can be seen nicely how the distance of the respective Fermi surface sheets, from the zeroes of the band structure, evolves. While in [LGP$^+$06] it has been shown that this distance nicely corresponds to the nesting condition (3.1) in $BaVS_3$, the qualitative development of this distance is the same in $BaVS_3$ and $BaVSe_3$, so that it is not possible to make a definite statement about which system is more susceptible to the nesting in question from this picture only. Except for the qualitative statements mentioned above, the same applies to the Fermi surface discussion.

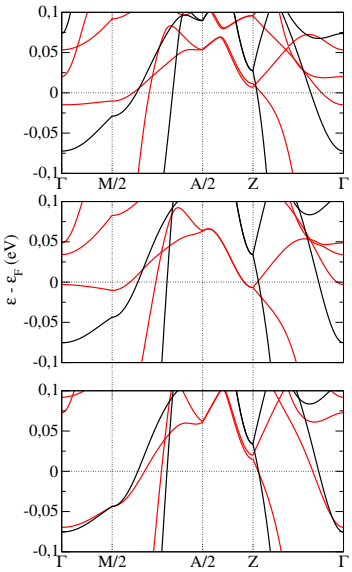

Figure 3.11: Original Wannier band structure (black) and renormalised band structure from LDA+DMFT (red) for $BaVS_3$ (top) and $BaVSe_3$ with U=3.5 eV (middle) and U=2.5 eV (bottom). The closed path including '$M/2$' and '$A/2$' (see figure 3.3) is used.

The last quantities that are supposed to be compared for $BaVS_3$ and $BaVSe_3$ are the magnetic degrees of freedom, which are important for both systems in view of their respective low-temperature magnetic ordering. This is done via local spin correlation functions calculated in RISB, i. e. the expectation value $\langle S_m \cdot S_{m'} \rangle$ of spins S_m with m and m' denoting orbitals from the t_{2g} manifold. They are shown as a function of U in the figures 3.12 (for varying J with $U/J = 5$) and 3.13 (for fixed $J = 0.7$ eV). To begin with, the diagonal spin correlation functions $\langle S_m^2 \rangle$ evolve similarly to the orbital occupation numbers, shown in figure 3.8, as can be expected. So the $\langle S_m^2 \rangle$ value

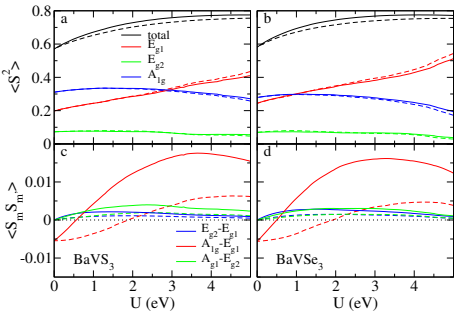

Figure 3.12: Spin correlation functions $\langle S_m \cdot S_{m'} \rangle$ among the t_{2g} manifold of $BaVS_3$ (left) and $BaVSe_3$ (right). Dashed lines: density-density only interactions, solid lines: including also spin-flip and pair-hopping terms. In each U scan a ratio $U/J = 5$ was chosen. Top row: Total and orbital-resolved diagonal spin-spin expectation value. Bottom row: Off diagonal spin-spin correlation between the effective t_{2g} orbitals.

for the E_{g1} orbital exceeds the corresponding value for the A_{1g} orbital in the large U limit. Furthermore, the E_{g1} value becomes larger for the selenide compound than for the sulfide compound, again according to the orbital occupation numbers. The total $\langle S^2 \rangle$ value increases with increasing U (due to the obviously increasing electron localisation) and saturates at a value which is slightly larger than the expected atomic value for a single electron spin-$\frac{1}{2}$-system, which is

$$\langle S^2 \rangle_{\text{at}} = \frac{1}{2}\left(\frac{1}{2} + 1\right) = \frac{3}{4}$$

This is probably due to a possible two electron occupation tolerated by the strong Hund's coupling, which then would lead to an $S = 1$ system.

The off-diagonal parts of the spin correlation functions show a more distinct behaviour. The first thing that is noticeable is that

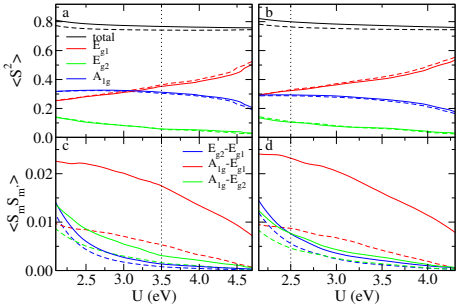

Figure 3.13: Same as figure 3.12, but with Hund's coupling fixed at a value of $J = 0.7$ eV. The vertical dotted lines indicate the expected suitable choice for the Hubbard U of the respective system.

the omission of spin-flip and pair-hopping terms in the interacting Hamilton operator has quite a large influence, up to a factor of two or three in the actual numbers. One can summarise that the influence of spin-flip and pair-hopping is most significant for two-particle related quantities (like susceptibilities), whereas the one-particle related quantities are by far less sensitive. The second remarkable property is that $\langle S_m \cdot S_{m'} \rangle$ eventually becomes negative for small values of U, in violation of Hund's first rule, which suggests a maximal spin value. Finally, for large values of U, all inter-orbital spin-spin correlation functions decay, which corresponds to the limit of the electron in the t_{2g} manifold being localised in one single orbital. This is contrary to what is seen in half-filled Hubbard models.

Coming back to the comparison of the two materials in question, one can see that the overall behaviour of the spin correlation functions is again qualitatively very similar. However, the two significantly different values of U that are expected to govern the physics of the two systems are indicated in the plots in figure 3.13. Especially the A_{1g}-E_{g1} inter-orbital correlation function shows significantly larger values for the selenide than for the sulfide at the highlighted values. This is

again in line with the picture of increased hybridisation between the A_{1g} and the E_{g1} orbital in the selenide.

3.5 Conclusive discussion

Probably the most striking result from the above-mentioned investigations is the similarity of the two systems Barium Vanadium sulfide ($BaVS_3$) and Barium Vanadium selenide ($BaVSe_3$). Basically all qualitative features that occur in the sulfide can also be found in the selenide. The differences that may give hints about the physically observed low-temperature phases that are completely different for the two compounds seem to be exclusively on a rather subtle quantitative level. They start already on the LDA level, where one can observe a smaller bandwidth of the selenide compared to the sulfide, in line with a stronger hybridisation within the t_{2g} manifold as well as of the t_{2g} manifold with the lower-lying sulfur/selenium states. The former indicates that a clear distinction between quasi-one-dimensional itinerant A_{1g} orbitals and more localised E_g orbitals is not as clear in the selenide as it is in the sulfide. One can rather assume a more cooperative behaviour of the orbitals in question in the selenide. The latter gives a clear hint that the effective interaction parameter U is significantly reduced in the selenide compared to the sulfide, thus rendering correlation effects generally reduced, or, in other words, shifting the selenide compound closer towards the LDA limit. On the LDA+DMFT (or LDA+RISB) level, this gives rise to a slightly different renormalisation behaviour of the respective Fermi surface sheets, making a nesting scenario less likely in the selenide compound. However, the distinction of the two compounds on a pure Fermi surface/band renormalisation level is not unambiguous. Note that, in view of the competing ordering mechanisms that are observed (charge-density-wave formation versus magnetic ordering), this does not mean that correlation effects are negligible in the selenide compound. In line with that, local magnetic susceptibilities seem to be larger in the selenide compound. Neverthe-

less, a definite statement about the magnetic ordering would require the calculation of inter-site magnetic susceptibilities, which has not been done here.

In summary, although the clear definite answer about the relevant differences between the two compounds has probably not been found in this investigation, one can say that the applied state-of-the-art LDA+DMFT and LDA+RISB are capable of revealing subtle quantitative differences of surprisingly similar materials, which makes it promising to proceed to the following new formal developments therein.

Four

Charge Self-Consistency

Now that a first application of the state-of-the-art consecutive (or post-processing or single shot) combination of LDA and DMFT as well as LDA and RISB has been presented, the new developments of this work regarding the further entanglement of the two methods shall be considered in detail. As mentioned, the general idea thereof is the charge self-consistency: From the output of the DMFT or RISB calculation, one can construct a correlated charge density which first of all does not correspond to the charge density that emerges from the LDA calculation. However, when putting it back into the LDA Kohn-Sham potentials, a self-consistency cycle can be established, which is presented in this chapter.

In [GPPL12], the implementation of the self-consistency cycle is published in brief, along with the Vanadium sesquioxide results of chapter 5 and a third implementation for the PAW part of the VASP code that was made by Oleg Peil. Similar developments have been made in other groups, which are published as [KSH+06, MCP+05, PABG07, HYK10, APG11, GDT+12, Ama12, ZZD+12].

4.1 The general idea

Up to this point, the sloppy formulation "the charge density of DMFT is put back into the LDA Kohn-Sham potentials" has been used. The Hartree potential (2.14) and the exchange-correlation potential (2.15) depend directly on the electronic charge density. Therefore, if one succeeds in finding a suitable representation of the DMFT charge density as described in section 4.2, one can directly put the DMFT charge density into these potential contributions. However, it is important to keep in mind the next step: The "normal" DFT Kohn-Sham self-consistency cycle would diagonalise the Hamilton operator with the new effective potential (depending on the algorithm in one step or in an iterative scheme) and then build a new charge density from the output of the diagonalisation. So if one would iterate over this cycle, one would obtain the same Kohn-Sham wave functions as before, irrespective of the DMFT input charge density.

The "solution" thereof is, of course, not to start the Kohn-Sham self-consistency cycle again after the Hamilton operator diagonalisation. One has to consider the LDA+DMFT charge self-consistency cycle as a new enlarged cycle in which the charge density that enters the Kohn-Sham Hamilton operator is kept fixed during the Kohn-Sham part. Thus, this part of the enlarged cycle is actually only one matrix diagonalisation that typically consist of only one single Kohn-Sham step, except for iterative diagonalisation algorithms that are also frequently used in present DFT codes. The output of this Kohn-Sham part are the new Kohn-Sham eigenfunctions that afterwards enter the projection onto localised orbitals formalism (alternatively another suitable formalism to construct a basis for the correlated subspace). With this new basis, a new DMFT step (or several thereof, according to convergence considerations) can be done and so a whole new cycle can be iterated over. The charge density $n^{\mathrm{KS}}(\underline{r})$ that one would obtain directly from the new Kohn-Sham eigenfunctions via (2.9) is in principle useless. Thus, it is important to note that this charge density and the charge density that enters the Kohn-Sham po-

tentials do no longer coincide.

So, to give a summary of the whole cycle and an overview of the following sections, the following enumeration lists all of the basic steps of the charge self-consistency cycle in their order of occurence:

1. Do a complete well-converged self-consistent Kohn-Sham LDA calculation as described in section 2.1. The result thereof are Kohn-Sham energy eigenvalues $\epsilon_{\underline{k}\nu}$ and wave functions $|\psi_{\underline{k}\nu}\rangle$.

2. Use $|\psi_{\underline{k}\nu}\rangle$ and a set of localised orbitals $|\chi_{\underline{k}m}\rangle$ (the latter remains fixed throughout the cycle) to compute and normalise projection matrix elements $P_{m\nu}(\underline{k})$ as described in section 2.3.2. In principle, also the maximally localised Wannier construction could be used for this step. However, this is not done in this work, because this basis directly depends on the Kohn-Sham wave functions and thus changes from iteration to iteration. Besides some technical problems thereof, this would add a non-variational degree of freedom into the cycle.

3. Compute the chemical potential μ as described in section 4.3.

4. Do a DMFT calculation with the input of projection matrices $P_{m\nu}(\underline{k})$, energy eigenvalues $\epsilon_{\underline{k}\nu}$ and the chemical potential μ as described in section 2.2.1. DMFT does not have to be converged in each step of the large cycle, typically it is sufficient to do only one DMFT iteration per iteration of the large cycle. For the first iteration, it is sometimes useful but not necessary to have a starting point from a single-shot LDA+DMFT calculation. If RISB is used instead of DMFT, the formalism is typically converged in each cycle iteration.

5. Recalculate μ and calculate the quantity μ^{KS} as described in section 4.3.

6. From the output of the DMFT or RISB calculation, extract the correlated charge density $n^{\mathrm{DMFT}}(\underline{r})$ in virtue of the matrix

$\Delta\underline{\underline{N}}^{(\underline{k})}$. For DMFT, this is described in section 4.2. For RISB, a short overview is given in section 4.6.

7. Insert $n^{\mathrm{DMFT}}(\underline{r})$ into the Kohn-Sham LDA potential to obtain a potential $v^{\mathrm{DMFT}}_{\mathrm{new}}(\underline{r})$.

8. Use a suitable root-finding ("mixing") algorithm to obtain an input potential $v^{\mathrm{DMFT}}(\underline{r})$ to the Kohn-Sham diagonalisation part from $v^{\mathrm{DMFT}}_{\mathrm{new}}(\underline{r})$ and the input potentials of the previous cycle iterations (and, especially in the first iteration, the original LDA potential). For small systems, a linear mixing scheme (forward iteration) with the input potential $v^{\mathrm{DMFT}}_{\mathrm{old}}(\underline{r})$ of the previous iteration is often sufficient:

$$v^{\mathrm{DMFT}}(\underline{r}) = \alpha \cdot v^{\mathrm{DMFT}}_{\mathrm{new}}(\underline{r}) + (1-\alpha) \cdot v^{\mathrm{DMFT}}_{\mathrm{old}}(\underline{r}) \tag{4.1}$$

   α is typically in the range of 0.1. An alternative can be the use of Broyden's method [Bro65] to find a root of the function $v^{\mathrm{DMFT}}_{\mathrm{new}}(\underline{r}) - v^{\mathrm{DMFT}}_{\mathrm{old}}(\underline{r})$ expressed in a suitable basis, although this is numerically difficult because of the noise due to quantum Monte-Carlo.

9. Diagonalise the Kohn-Sham Hamilton operator comprising the new potential $v^{\mathrm{DMFT}}(\underline{r})$ using, depending on the DFT code in question, a direct matrix diagonalisation or an iterative scheme. The results are new energy eigenvalues $\epsilon_{\underline{k}\nu}$ and wave functions $|\psi_{\underline{k}\nu}\rangle$.

10. Calculate total energies of the formalism as described in section 4.5.

11. Close the cycle by inserting the new $\epsilon_{\underline{k}\nu}$ and $|\psi_{\underline{k}\nu}\rangle$ into step 2.

Finally, a suitable criterion about the convergence of the cycle has to be included. It has proven to be practical to watch the following three quantities simultaneously:

- A criterion to judge the convergence of the DMFT part, such as the change of the chemical potential from iteration to iteration or the DMFT self-energy of the first Matsubara frequency.
- The total energy of the formalism.
- The norm of the matrix $\Delta\underline{\underline{N}}^{(\underline{k})}$ that describes the change of the charge density. Note that $\Delta\underline{\underline{N}}^{(\underline{k})}$ does not become zero, but rather approaches a constant value.

4.2 Expressing charge densities

It has been emphasised that probably the key step of the combination of LDA and many-particle methods is to find a suitable expression of the charge density, which is the basic quantity of DFT, in terms of the output basic quantities of the many-particle methods in question. In this section, such an expression shall be presented for DMFT, of which the basic quantities are Green's functions. Although this is not the main topic of this work, a short glance on such an expression for the more Hamilton-operator based RISB technique is given in section 4.6.

This section focuses on the projection onto localised orbitals (PLO) technique presented in section 2.3.2. In principle, similar expressions could be found for other interfacing techniques like the maximally-localised Wannier function construction (see section 2.3.1), putting the ideas presented at the beginning of section 2.3.1 into practise. In the PLO formalism, a direct connection to the LDA output can be made in the "Bloch space" $\mathcal{W}$ in which the k-dependent Bloch Green's function reads as follows (cf. (2.102)):

$$\underline{\underline{G}}^{\mathrm{bl}}(\underline{k}, \mathrm{i}\omega_n) = \left[(\mathrm{i}\omega_n + \mu)\,\underline{\underline{1}} - \underline{\underline{\epsilon}}_{\underline{k}} - \Delta\underline{\underline{\Sigma}}^{\mathrm{bl}}(\underline{k}, \mathrm{i}\omega_n)\right]^{-1} \tag{4.2}$$

In this equation, $\underline{\underline{\epsilon}}_{\underline{k}}$ is simply the diagonal matrix of Kohn-Sham eigenvalues from DFT, $\Delta\underline{\underline{\Sigma}}^{\mathrm{bl}}$ is the double-counting corrected impurity self-

energy from DMFT upfolded to Bloch space (cf. (2.103)):

$$\Delta\underline{\underline{\Sigma}}^{\mathrm{bl}}(\underline{k}, \mathrm{i}\omega_n) = \underline{\underline{P}}^{\dagger}(\underline{k}) \cdot \left(\underline{\underline{\Sigma}}^{\mathrm{imp}}(\mathrm{i}\omega_n) - \underline{\underline{\Sigma}}^{\mathrm{DC}}\right) \cdot \underline{\underline{P}}(\underline{k}) \tag{4.3}$$

The matrices $\underline{\underline{P}}(\underline{k})$ are the projection matrices (the unitarisation of $\tilde{P}_{m\nu}(\underline{k}) \equiv \langle \chi_m | \psi_{\underline{k}\nu} \rangle$, see section 2.3.2) and the calculation and choice of the chemical potential μ is described in section 4.3.

One can define a Green's function $\underline{\underline{G}}^{\mathrm{KS}}$ of a non-interacting system in Bloch space simply by setting $\Delta\underline{\underline{\Sigma}}^{\mathrm{bl}}$ to zero:

$$\underline{\underline{G}}^{\mathrm{KS}}(\underline{k}, \mathrm{i}\omega_n) = \left[(\mathrm{i}\omega_n + \mu^{\mathrm{KS}})\,\underline{\underline{1}} - \underline{\underline{\epsilon}}_{\underline{k}}\right]^{-1} \tag{4.4}$$

Thus, this "Kohn-Sham Green's function" directly corresponds to a Green's function of the pure LDA Kohn-Sham input (that, however, changes in the course of the charge self-consistency cycle). The quantity μ^{KS} that occurs therein should not be understood as a chemical potential, but rather as an auxiliary quantity which is described in detail in section 4.3.1.

These Green's functions can directly be used to construct charge densities. The principal idea to do so is to calculate the (not necessarily diagonal) density matrix $n^{\mathrm{bl}}_{\underline{k}\nu\nu'}$ in the Bloch basis they are written in. Expressed in imaginary time τ, the density matrix corresponds to the value of the respective Green's function for $\tau \to 0^+$:

$$n^{\mathrm{bl}}_{\underline{k}\nu\nu'} = \delta_{\nu\nu'} + G^{\mathrm{bl}}_{\nu\nu'}(\underline{k}, \tau \to 0^+) \tag{4.5}$$

This can easily be seen from the definition of Green's functions for imaginary times as the expectation value of the time-ordered product of an annihilator at time τ and a creator at $\tau = 0$ and one application of their anti-commutation relation. The Fourier transform thereof for $\tau \to 0$ is a Matsubara frequency sum:

$$n^{\mathrm{bl}}_{\underline{k}\nu\nu'} = \frac{1}{\beta} \sum_{n=-\infty}^{\infty} G^{\mathrm{bl}}_{\nu\nu'}(\underline{k}, \mathrm{i}\omega_n) \tag{4.6}$$

β is, as usual, the inverse temperature, which corresponds to half of the length of one period of the Green's function in imaginary time. For the practical evaluation of the Matsubara frequency sum, symmetry properties of the Green's functions can be exploited, which restricts the sum to positive Matsubara frequencies:

$$G^{\mathrm{bl}}_{\nu\nu'}(\underline{k}, -\mathrm{i}\omega_n) = \left(G^{\mathrm{bl}}_{\nu'\nu}(\underline{k}, \mathrm{i}\omega_n)\right)^* \tag{4.7}$$

Since the basis functions of the Bloch basis in real space are known (the Bloch wave functions $\langle \underline{r}|\psi_{\underline{k}\nu}\rangle$ from LDA), one can directly write down the DMFT charge density from this density matrix as follows:

$$\begin{aligned} n^{\mathrm{DMFT}}(\underline{r}) &= \sum_{\underline{k}} \sum_{\nu\nu'} \langle \underline{r}|\psi_{\underline{k}\nu}\rangle \cdot n^{\mathrm{bl}}_{\underline{k}\nu\nu'} \cdot \langle \psi_{\underline{k}\nu'}|\underline{r}\rangle & (4.8) \\ &= \frac{1}{\beta} \sum_{\underline{k}} \sum_{n\nu\nu'} \langle \underline{r}|\psi_{\underline{k}\nu}\rangle \cdot G^{\mathrm{bl}}_{\nu\nu'}(\underline{k}, \mathrm{i}\omega_n) \cdot \langle \psi_{\underline{k}\nu'}|\underline{r}\rangle & (4.9) \end{aligned}$$

At this point, it becomes evident why the definition of the non-interacting Kohn-Sham Green's function is useful: With the help thereof, it is possible to write down a very similar expression for the original charge density $n^{\mathrm{KS}}(\underline{r})$ from LDA:

$$n^{\mathrm{KS}}(\underline{r}) = \frac{1}{\beta} \sum_{\underline{k}} \sum_{n\nu\nu'} \langle \underline{r}|\psi_{\underline{k}\nu}\rangle \cdot G^{\mathrm{KS}}_{\nu\nu'}(\underline{k}, \mathrm{i}\omega_n) \cdot \langle \psi_{\underline{k}\nu'}|\underline{r}\rangle \tag{4.10}$$

Thus, the difference $\Delta n(\underline{r}) = n^{\mathrm{DMFT}}(\underline{r}) - n^{\mathrm{KS}}(\underline{r})$ reads as follows:

$$\Delta n(\underline{r}) = \sum_{\underline{k}} \sum_{\nu\nu'} \underbrace{\langle \underline{r}|\psi_{\underline{k}\nu}\rangle\langle\psi_{\underline{k}\nu'}|\underline{r}\rangle}_{D^{(\underline{k})}_{\nu'\nu}(\underline{r})} \cdot \underbrace{\frac{1}{\beta} \sum_{n} \left(\underline{\underline{G}}^{\mathrm{bl}}(\underline{k}, \mathrm{i}\omega_n) - \underline{\underline{G}}^{\mathrm{KS}}(\underline{k}, \mathrm{i}\omega_n)\right)_{\nu\nu'}}_{\Delta N^{(\underline{k})}_{\nu\nu'}} \tag{4.11}$$

The matrix $\Delta\underline{\underline{N}}^{(\underline{k})}$ defined in (4.11) can be simplified [LGP+06] (the

argument $(\underline{k}, \mathrm{i}\omega_n)$ of the Green's functions is dropped for readability):

$$\begin{aligned} \Delta\underline{\underline{N}}^{(\underline{k})} &= \frac{1}{\beta}\sum_n \left[\underline{\underline{G}}^{\mathrm{KS}} \cdot \left(\underline{\underline{G}}^{\mathrm{KS}}\right)^{-1} \cdot \underline{\underline{G}}^{\mathrm{bl}} - \underline{\underline{G}}^{\mathrm{KS}} \cdot \left(\underline{\underline{G}}^{\mathrm{bl}}\right)^{-1} \cdot \underline{\underline{G}}^{\mathrm{bl}}\right] \\ &= \frac{1}{\beta}\sum_n \left(\underline{\underline{G}}^{\mathrm{KS}} \cdot \left(\left(\underline{\underline{G}}^{\mathrm{KS}}\right)^{-1} - \left(\underline{\underline{G}}^{\mathrm{bl}}\right)^{-1}\right) \cdot \underline{\underline{G}}^{\mathrm{bl}}\right) \end{aligned} \tag{4.12}$$

By comparing the Green's functions' definitions (4.4) and (4.2), one can see that the difference of the inverted Green's functions is the Bloch self-energy $\Delta\underline{\underline{\Sigma}}^{\mathrm{bl}}$ and a shift, depending on the choice of the quantity μ^{KS}:

$$\left(\underline{\underline{G}}^{\mathrm{KS}}\right)^{-1} - \left(\underline{\underline{G}}^{\mathrm{bl}}\right)^{-1} = \Delta\underline{\underline{\Sigma}}^{\mathrm{bl}} - (\mu - \mu^{\mathrm{KS}})\,\underline{\underline{1}} \tag{4.13}$$

Insertion yields:

$$\Delta\underline{\underline{N}}^{(\underline{k})} = \frac{1}{\beta}\sum_n \left(\underline{\underline{G}}^{\mathrm{KS}}(\underline{k}, \mathrm{i}\omega_n)\left(\Delta\underline{\underline{\Sigma}}^{\mathrm{bl}}(\underline{k}, \mathrm{i}\omega_n) - (\mu - \mu^{\mathrm{KS}})\,\underline{\underline{1}}\right)\underline{\underline{G}}^{\mathrm{bl}}(\underline{k}, \mathrm{i}\omega_n)\right) \tag{4.14}$$

This matrix $\Delta\underline{\underline{N}}^{(\underline{k})}$ is the central output quantity of the DMFT part in the charge self-consistent formalism. From this matrix only, all relevant charge densities can be reconstructed in the LDA part of the formalism. From the density matrix $\underline{\underline{D}}^{(\underline{k})}(\underline{r})$ of Kohn-Sham wave functions (defined in (4.11)), the charge density difference can be written as a matrix trace:

$$\Delta n(\underline{r}) = \sum_{\underline{k}} \mathrm{Tr}_\nu \left[\underline{\underline{D}}^{(\underline{k})}(\underline{r}) \cdot \Delta\underline{\underline{N}}^{(\underline{k})}\right] = \sum_{\underline{k}} \sum_{\nu\nu' \in \mathcal{W}} D^{(\underline{k})}_{\nu'\nu}(\underline{r}) \cdot \Delta N^{(\underline{k})}_{\nu\nu'} \tag{4.15}$$

From the usual representation of the Kohn-Sham charge density $n^{\mathrm{KS}}(\underline{r})$ (cf. (2.9)) with suitable occupation numbers $n_{\underline{k}\nu}$

$$n^{\mathrm{KS}}(\underline{r}) = \sum_{\underline{k}} \sum_{\nu} n_{\underline{k}\nu} D^{(\underline{k})}_{\nu\nu}(\underline{r}) \tag{4.16}$$

it is possible to write the entire DMFT charge density from the two matrices only:

$$n^{\mathrm{DMFT}}(\underline{r}) = \sum_{\underline{k}} \left[\sum_{\nu} n_{\underline{k}\nu} D^{(\underline{k})}_{\nu\nu}(\underline{r}) + \sum_{\nu\nu' \in \mathcal{W}} D^{(\underline{k})}_{\nu'\nu}(\underline{r}) \cdot \Delta N^{(\underline{k})}_{\nu\nu'} \right] \tag{4.17}$$

Note that in the first summand, the sum over Bloch bands ν runs over the entire Bloch space, while in the second summand, only the subspace $\mathcal{W}$ is selected. So with the help of this splitting into two charge density contributions, the problem can be solved how a meaningful charge density of the whole Bloch space can be constructed, although the DMFT solution is inherently limited to a tiny subspace thereof. Furthermore, it can be seen that the effect of the strong electronic correlations of DMFT manifests on the charge density by additional off-diagonal occupation matrix elements to the purely diagonal DFT solution. The first summand is basically the normal charge density construction of DFT (with, of course, some assumptions on the quantity μ^{KS} that are described in section 4.3.1). For technical reasons, the matrix $\underline{\underline{D}}^{(\underline{k})}(\underline{r})$ is not saved explicitly on a computer, because this would require very large memory sizes. So the exact technical construction scheme of the charge density $n^{\mathrm{DMFT}}(\underline{r})$ depends on the basis set that is used for DFT and shall be explained in the following subsections for each of the basis sets in question individually.

4.2.1 Projector-augmented wave method

The general concept to calculate charge densities in the PAW method is described in section 2.1.4 according to [BFS03]. The charge self-consistency implementation for PAW is very similar to the one presented in [Ama12]. One can start from the matrix $\underline{\underline{D}}^{(\underline{k})}(\underline{r})$ defined in (4.11):

$$D^{(\underline{k})}_{\nu'\nu}(\underline{r}) = \langle \psi_{\underline{k}\nu'} | \underline{r} \rangle \langle \underline{r} | \psi_{\underline{k}\nu} \rangle \tag{4.18}$$

By inserting the well-known PAW transformation rule (2.26), it becomes:

$$\begin{aligned} D^{(\underline{k})}_{\nu'\nu}(\underline{r}) &= \left[\langle\tilde{\psi}_{\underline{k}\nu'}|\underline{r}\rangle + \sum_i \left(\langle\phi_i|\underline{r}\rangle - \langle\tilde{\phi}_i|\underline{r}\rangle\right)\left(\langle\tilde{p}_i|\psi_{\underline{k}\nu'}\rangle\right)^*\right] \\ &\cdot \left[\langle\underline{r}|\tilde{\psi}_{\underline{k}\nu}\rangle + \sum_j \left(\langle\underline{r}|\phi_j\rangle - \langle\underline{r}|\tilde{\phi}_j\rangle\right)\langle\tilde{p}_j|\tilde{\psi}_{\underline{k}\nu}\rangle\right] \end{aligned} \tag{4.19}$$

Expanding this equation step by step, it becomes:

$$\begin{aligned} D^{(\underline{k})}_{\nu'\nu}(\underline{r}) &= \langle\tilde{\psi}_{\underline{k}\nu'}|\underline{r}\rangle\langle\underline{r}|\tilde{\psi}_{\underline{k}\nu}\rangle \\ &+ \sum_{ij}\langle\phi_i - \tilde{\phi}_i|\underline{r}\rangle\langle\underline{r}|\phi_j - \tilde{\phi}_j\rangle\langle\tilde{\psi}_{\underline{k}\nu'}|\tilde{p}_i\rangle\langle\tilde{p}_j|\tilde{\psi}_{\underline{k}\nu}\rangle \\ &+ \sum_i\langle\phi_i - \tilde{\phi}_i|\underline{r}\rangle\langle\underline{r}|\tilde{\psi}_{\underline{k}\nu}\rangle\langle\tilde{\psi}_{\underline{k}\nu'}|\tilde{p}_i\rangle \\ &+ \sum_j\langle\underline{r}|\phi_j - \tilde{\phi}_j\rangle\langle\tilde{p}_j|\tilde{\psi}_{\underline{k}\nu}\rangle\langle\tilde{\psi}_{\underline{k}\nu'}|\underline{r}\rangle \end{aligned} \tag{4.20}$$

One can make the usual PAW assumption that the partial waves are located entirely inside atomic spheres around the nuclei, so that it shall be assumed that the double sums in the following equations run only over i and j of the same atom μ. With this assumption, one can

add zero in the last two summands:

$$
\begin{aligned}
D^{(\underline{k})}_{\nu'\nu}(\underline{r}) &= \langle\tilde{\psi}_{\underline{k}\nu'}|\underline{r}\rangle\langle\underline{r}|\tilde{\psi}_{\underline{k}\nu}\rangle \\
&+ \sum_{\mu}\sum_{ij\in\mu}\langle\phi_i-\tilde{\phi}_i|\underline{r}\rangle\langle\underline{r}|\phi_j-\tilde{\phi}_j\rangle\langle\tilde{\psi}_{\underline{k}\nu'}|\tilde{p}_i\rangle\langle\tilde{p}_j|\tilde{\psi}_{\underline{k}\nu}\rangle \\
&+ \sum_{\mu}\sum_{ij\in\mu}\langle\phi_i-\tilde{\phi}_i|\underline{r}\rangle\langle\underline{r}|\left(|\tilde{\psi}_{\underline{k}\nu}\rangle-|\tilde{\phi}_j\rangle\langle\tilde{p}_j|\tilde{\psi}_{\underline{k}\nu}\rangle\right)\langle\tilde{\psi}_{\underline{k}\nu'}|\tilde{p}_i\rangle \\
&+ \sum_{\mu}\sum_{ij\in\mu}\langle\phi_i-\tilde{\phi}_i|\underline{r}\rangle\langle\underline{r}|\tilde{\phi}_j\rangle\langle\tilde{p}_j|\tilde{\psi}_{\underline{k}\nu}\rangle\langle\tilde{\psi}_{\underline{k}\nu'}|\tilde{p}_i\rangle \\
&+ \sum_{\mu}\sum_{ij\in\mu}\left(\langle\tilde{\psi}_{\underline{k}\nu'}|-\langle\tilde{\phi}_i|\langle\tilde{\psi}_{\underline{k}\nu'}|\tilde{p}_i\rangle\right)|\underline{r}\rangle\langle\underline{r}|\phi_j-\tilde{\phi}_j\rangle\langle\tilde{p}_j|\tilde{\psi}_{\underline{k}\nu}\rangle \\
&+ \sum_{\mu}\sum_{ij\in\mu}\langle\tilde{\phi}_i|\underline{r}\rangle\langle\underline{r}|\phi_j-\tilde{\phi}_j\rangle\langle\tilde{\psi}_{\underline{k}\nu'}|\tilde{p}_i\rangle\langle\tilde{p}_j|\tilde{\psi}_{\underline{k}\nu}\rangle
\end{aligned}
\tag{4.21}
$$

The terms in brackets in the third and fifth summand thereof vanish due to the definition of the projector functions (2.25). The fourth and sixth summand cancels the mixed terms of the second summand and changes the sign of the pseudopartial-pseudopartial term therein. So the matrix simplifies as follows:

$$
\begin{aligned}
D^{(\underline{k})}_{\nu'\nu}(\underline{r}) &= \langle\tilde{\psi}_{\underline{k}\nu'}|\underline{r}\rangle\langle\underline{r}|\tilde{\psi}_{\underline{k}\nu}\rangle \\
&+ \sum_{\mu}\sum_{ij\in\mu}\langle\phi_i|\underline{r}\rangle\langle\underline{r}|\phi_j\rangle\langle\tilde{\psi}_{\underline{k}\nu'}|\tilde{p}_i\rangle\langle\tilde{p}_j|\tilde{\psi}_{\underline{k}\nu}\rangle \\
&+ \sum_{\mu}\sum_{ij\in\mu}\langle\tilde{\phi}_i|\underline{r}\rangle\langle\underline{r}|\tilde{\phi}_j\rangle\langle\tilde{\psi}_{\underline{k}\nu'}|\tilde{p}_i\rangle\langle\tilde{p}_j|\tilde{\psi}_{\underline{k}\nu}\rangle
\end{aligned}
\tag{4.22}
$$

So it is possible to construct the DMFT charge density according to (4.17) (taking $\Delta\underline{\underline{N}}^{(\underline{k})}$ from the DMFT part) in this representation:

$$
\begin{aligned}
n^{\mathrm{DMFT}}(\underline{r}) &= \sum_{\underline{k}} \sum_{\nu\nu'} D^{(\underline{k})}_{\nu'\nu}(\underline{r}) \cdot \left(\Delta N^{(\underline{k})}_{\nu\nu'} + n_{\underline{k}\nu}\, \delta_{\nu\nu'} \right) && (4.23) \\
&= \sum_{\underline{k}} \sum_{\nu\nu'} \Bigg[\langle \tilde{\psi}_{\underline{k}\nu'} | \underline{r} \rangle \left(\Delta N^{(\underline{k})}_{\nu\nu'} + n_{\underline{k}\nu}\, \delta_{\nu\nu'} \right) \langle \underline{r} | \tilde{\psi}_{\underline{k}\nu} \rangle && (4.24) \\
&+ \sum_{\mu} \sum_{ij\in\mu} \langle \phi_i | \underline{r} \rangle \langle \underline{r} | \phi_j \rangle \langle \tilde{\psi}_{\underline{k}\nu'} | \tilde{p}_i \rangle \left(\Delta N^{(\underline{k})}_{\nu\nu'} + n_{\underline{k}\nu} \delta_{\nu\nu'} \right) \langle \tilde{p}_j | \tilde{\psi}_{\underline{k}\nu} \rangle \\
&+ \sum_{\mu} \sum_{ij\in\mu} \langle \tilde{\phi}_i | \underline{r} \rangle \langle \underline{r} | \tilde{\phi}_j \rangle \langle \tilde{\psi}_{\underline{k}\nu'} | \tilde{p}_i \rangle \langle \tilde{p}_j | \tilde{\psi}_{\underline{k}\nu} \rangle \left(\Delta N^{(\underline{k})}_{\nu\nu'} + n_{\underline{k}\nu} \delta_{\nu\nu'} \right) \Bigg]
\end{aligned}
$$

For simplification of the formula, it is assumed that the matrix $\Delta\underline{\underline{N}}^{(\underline{k})}$ vanishes for $\nu, \nu' \notin \mathcal{W}$. So one can define a DMFT one-centre density matrix $\mathcal{D}^{\mathrm{DMFT}}_{ij}$ as follows:

$$
\mathcal{D}^{\mathrm{DMFT}}_{ij} \equiv \sum_{\underline{k}} \sum_{\nu\nu'} \langle \tilde{p}_i | \tilde{\psi}_{\underline{k}\nu} \rangle \left(\Delta N^{(\underline{k})}_{\nu\nu'} + n_{\underline{k}\nu}\, \delta_{\nu\nu'} \right) \langle \tilde{\psi}_{\underline{k}\nu'} | \tilde{p}_j \rangle \qquad (4.25)
$$

With this definition, one obtains an expression for $n^{\mathrm{DMFT}}(\underline{r})$ that is very similar to the usual PAW charge density calculation (2.30) with the characteristic splitting into a plane wave part and a one-centre part:

$$
\begin{aligned}
n^{\mathrm{DMFT}}(\underline{r}) &= \sum_{\underline{k}} \sum_{\nu\nu'} \tilde{\psi}^*_{\underline{k}\nu'}(\underline{r}) \left(\Delta N^{(\underline{k})}_{\nu\nu'} + n_{\underline{k}\nu}\, \delta_{\nu\nu'} \right) \tilde{\psi}_{\underline{k}\nu}(\underline{r}) && (4.26) \\
&+ \sum_{\mu} \sum_{ij\in\mu} \mathcal{D}^{\mathrm{DMFT}}_{ij} \left(\phi^*_j(\underline{r})\, \phi_i(\underline{r}) - \tilde{\phi}^*_j(\underline{r})\, \tilde{\phi}_i(\underline{r}) \right)
\end{aligned}
$$

So the strategy to construct this DMFT charge density at the beginning of the LDA part of the charge self-consistency cycle is to take the pseudo wave functions $\psi_{\underline{k}\nu}(\underline{r})$ represented in a plane wave basis

as well as the matrix elements $\langle \tilde{p}_i | \tilde{\psi}_{\underline{k}\nu} \rangle$ from the previous cycle iteration. Since the partial waves $\phi_i(\underline{r})$ and $\tilde{\phi}_i(\underline{r})$ remain fixed throughout the calculation, this is sufficient to construct the matrix $\mathcal{D}_{ij}^{\mathrm{DMFT}}$ that enters the usual PAW one-centre density construction as well as to build the plane wave part with additional off-diagonal contributions as usual via a Fourier transformation.

4.2.2 Mixed-basis pseudopotential method

In a pure pseudopotential formulation, the DMFT charge density could readily be calculated from (4.17) without further modifications. However, since a mixed-basis formulation thereof is used in the present work, one again has to ensure that all elements of the mixed basis are treated correctly. It is instructive to start from the charge density difference $\Delta n(\underline{r})$, which can be written explicitly by inserting the mixed-basis wave function representation (2.37):

$$\begin{aligned}
\Delta n(\underline{r}) &= \sum_{\underline{k}} \sum_{\nu\nu' \in \mathcal{W}} \Delta N_{\nu\nu'}^{(\underline{k})} \cdot D_{\nu'\nu}^{(\underline{k})}(\underline{r}) && (4.27)\\
&= \sum_{\underline{k}} \sum_{\nu\nu' \in \mathcal{W}} \Delta N_{\nu\nu'}^{(\underline{k})} \cdot \psi_{\underline{k}\nu'}^{*}(\underline{r})\, \psi_{\underline{k}\nu}(\underline{r}) && (4.28)\\
&= \sum_{\underline{k}} \sum_{\nu\nu'} \Delta N_{\nu\nu'}^{(\underline{k})} \frac{1}{\Omega_{\mathrm{C}}} \sum_{\underline{G}} \left(\psi_{\underline{G}}^{\underline{k}\nu'} \right)^{*} \left(\mathrm{e}^{\mathrm{i}(\underline{k}+\underline{G})\underline{r}} \right)^{*} \sum_{\underline{G}'} \psi_{\underline{G}'}^{\underline{k}\nu}\, \mathrm{e}^{\mathrm{i}(\underline{k}+\underline{G}')\underline{r}}\\
&+ \sum_{\underline{k}} \sum_{\nu\nu'} \Delta N_{\nu\nu'}^{(\underline{k})} \frac{1}{\sqrt{\Omega_{\mathrm{C}}}} \sum_{\underline{G}} \left(\psi_{\underline{G}}^{\underline{k}\nu'} \right)^{*} \left(\mathrm{e}^{\mathrm{i}(\underline{k}+\underline{G})\underline{r}} \right)^{*} \sum_{\mu lm} \beta_{\mu lm}^{\underline{k}\nu} \phi_{\mu lm}^{\underline{k}}(\underline{r})\\
&+ \sum_{\underline{k}} \sum_{\nu\nu'} \Delta N_{\nu\nu'}^{(\underline{k})} \frac{1}{\sqrt{\Omega_{\mathrm{C}}}} \sum_{\underline{G}} \psi_{\underline{G}}^{\underline{k}\nu'}\, \mathrm{e}^{\mathrm{i}(\underline{k}+\underline{G})\underline{r}} \sum_{\mu lm} \left(\beta_{\mu lm}^{\underline{k}\nu} \phi_{\mu lm}^{\underline{k}}(\underline{r}) \right)^{*}\\
&+ \sum_{\underline{k}} \sum_{\nu\nu'} \Delta N_{\nu\nu'}^{(\underline{k})} \sum_{\mu lm} \left(\beta_{\mu lm}^{\underline{k}\nu'} \phi_{\mu lm}^{\underline{k}}(\underline{r}) \right)^{*} \sum_{\mu' l' m'} \beta_{\mu' l' m'}^{\underline{k}\nu} \phi_{\mu' l' m'}^{\underline{k}}(\underline{r})
\end{aligned}$$

As a product of three Hermitian matrices, the matrix $\Delta\underline{\underline{N}}^{(\underline{k})}$ is Hermitian at each $\underline{k}$-point:

$$\Delta N^{(\underline{k})}_{\nu'\nu} = \left(\Delta N^{(\underline{k})}_{\nu\nu'}\right)^*$$

So, the third summand becomes the complex conjugate of the second summand by index renaming. So the sum of the two summands is twice the real part thereof:

$$\begin{aligned}
\Delta n(\underline{r}) &= \sum_{\underline{k}} \sum_{\nu\nu'} \left(\Delta N^{(\underline{k})}_{\nu\nu'} \frac{1}{\Omega_{\mathrm{C}}} \sum_{\underline{G}\underline{G}'} \left(\psi^{\underline{k}\nu'}_{\underline{G}}\right)^* \psi^{\underline{k}\nu}_{\underline{G}'} \, \mathrm{e}^{\mathrm{i}(\underline{G}-\underline{G}')\underline{r}} \right. \\
&+ \frac{2}{\sqrt{\Omega_{\mathrm{C}}}} \Re \left[\Delta N^{(\underline{k})}_{\nu\nu'} \sum_{\underline{G}} \psi^{\underline{k}\nu}_{\underline{G}} \mathrm{e}^{\mathrm{i}(\underline{k}+\underline{G})\underline{r}} \sum_{\mu l m} \left(\beta^{\underline{k}\nu'}_{\mu l m} \phi^{\underline{k}}_{\mu l m}(\underline{r})\right)^* \right] \\
&+ \left. \Delta N^{(\underline{k})}_{\nu\nu'} \sum_{\mu l m} \left(\beta^{\underline{k}\nu'}_{\mu l m} \phi^{\underline{k}}_{\mu l m}(\underline{r})\right)^* \sum_{\mu' l' m'} \beta^{\underline{k}\nu}_{\mu' l' m'} \phi^{\underline{k}}_{\mu' l' m'}(\underline{r}) \right)
\end{aligned} \tag{4.29}$$

Again, this resulting expression is similar to the usual representation of charge densities in the mixed-basis pseudopotential method, which is presented in section 2.1.4. So it is possible to calculate $\Delta n(\underline{r})$ together with the Kohn-Sham part of the charge density:

$$n^{\mathrm{DMFT}}(\underline{r}) = n^{\mathrm{DMFT}}_{(1)}(\underline{r}) + n^{\mathrm{DMFT}}_{(2)}(\underline{r}) + n^{\mathrm{DMFT}}_{(3)}(\underline{r}) \tag{4.30}$$

The ideas for an efficient charge density calculation that are presented in [Mey98] can also be used for $n^{\mathrm{DMFT}}(\underline{r})$. To begin with, the first summand

$$n^{\mathrm{DMFT}}_{(1)}(\underline{r}) = \sum_{\underline{k}} \sum_{\nu\nu'} \left(\Delta N^{(\underline{k})}_{\nu\nu'} + n_{\underline{k}\nu} \, \delta_{\nu\nu'} \right) \frac{1}{\Omega_{\mathrm{C}}} \sum_{\underline{G}\underline{G}'} \left(\psi^{\underline{k}\nu'}_{\underline{G}}\right)^* \psi^{\underline{k}\nu}_{\underline{G}'} \, \mathrm{e}^{\mathrm{i}(\underline{G}-\underline{G}')\underline{r}} \tag{4.31}$$

(again assuming $\Delta N^{(\underline{k})}_{\nu\nu'}$ to vanish for $\nu, \nu' \notin \mathcal{W}$) can, in principle, be evaluated directly from this sum. However, since the last double sum

is a convolution sum, it is numerically more efficient for large numbers of plane wave basis functions to use a fast Fourier transform algorithm to transform $\psi_{\underline{G}}^{\underline{k}\nu}$ to real space, calculate the product and transform the result back to $\underline{G}$-space (where it is finally needed) on a suitably enlarged grid. The second summand

$$n_{(2)}^{\mathrm{DMFT}}(\underline{r}) = \sum_{\underline{k}} \sum_{\nu\nu'} \frac{2}{\sqrt{\Omega_{\mathrm{C}}}} \Re \left[\left(\Delta N_{\nu\nu'}^{(\underline{k})} + n_{\underline{k}\nu}\, \delta_{\nu\nu'} \right) \cdot \sum_{\underline{G}} \psi_{\underline{G}}^{\underline{k}\nu} \mathrm{e}^{\mathrm{i}(\underline{k}+\underline{G})\underline{r}} \sum_{\mu lm} \left(\beta_{\mu lm}^{\underline{k}\nu'} \phi_{\mu lm}^{\underline{k}}(\underline{r}) \right)^* \right] \tag{4.32}$$

only contributes inside the non-overlapping spheres that are selected for the localised functions $\phi_{\mu lm}^{\underline{k}}(\underline{r})$. So it is useful to calculate it as a grid sum over lattice vectors $\underline{T}$ and spheres centred at the atomic positions $\underline{R}_\mu$:

$$n_{(2)}^{\mathrm{DMFT}}(\underline{r}) = \sum_{\underline{T}\mu lm} n_{(2)}^{\mu lm}(|\underline{r}'|)\, \mathrm{K}_{lm}(\widehat{\underline{r}}') \qquad \text{with} \quad \underline{r}' = \underline{r} - \underline{T} - \underline{R}_\mu \tag{4.33}$$

This can be done by expressing plane waves in terms of atom-centred cubic harmonics K_{lm} and spherical Bessel functions j_l via the following expansion theorem [Mey98]:

$$\mathrm{e}^{\mathrm{i}(\underline{k}+\underline{G})\underline{r}} = 4\pi \sum_{lm} \mathrm{i}^l\, \mathrm{j}_l(|\underline{k}+\underline{G}||\underline{r}|)\, \mathrm{K}_{lm}(\widehat{\underline{k}+\underline{G}}) \mathrm{K}_{lm}(\widehat{\underline{r}}) \tag{4.34}$$

Remembering that the localised functions are also written as a product of a radial part $f_{\mu l}$ and a cubic harmonic (2.39), the insertion of (4.34) into (4.32) yields products of two cubic harmonics, which can

be expressed using cubic Gaunt coefficients $g_{l_1,l_2,l}^{m_1,m_2,m}$. The result is:

$$\begin{aligned} n_{(2)}^{\mu lm}(|\underline{r}'|) &= \frac{4\pi}{\sqrt{\Omega_{\mathrm{C}}}} \sum_{l_1 m_1} \sum_{l_2 m_2} g_{l_1,l_2,l}^{m_1,m_2,m} f_{\mu l_1}(|\underline{r}'|) \\ &\cdot \sum_{\underline{k}} \sum_{\underline{G}} \mathrm{K}_{l_2 m_2}(\widehat{\underline{k}+\underline{G}})\, \mathrm{j}_{l_2}(|\underline{k}+\underline{G}||\underline{r}'|) \\ &\cdot 2\Re \left[\mathrm{i}^{l_2-l_1}\, \mathrm{e}^{\mathrm{i}\underline{G}\underline{R}_\mu} \sum_{\nu\nu'} \left(\Delta N_{\nu\nu'}^{(\underline{k})} + n_{\underline{k}\nu}\, \delta_{\nu\nu'} \right) \psi_{\underline{G}}^{\underline{k}\nu} \left(\beta_{\mu lm}^{\underline{k}\nu'} \right)^* \right] \end{aligned} \tag{4.35}$$

This result can finally be Fourier-transformed back to $\underline{G}$-space by another application of the expansion theorem (4.34). The third part of $n^{\mathrm{DMFT}}(\underline{r})$

$$\begin{aligned} n_{(3)}^{\mathrm{DMFT}}(\underline{r}) &= \sum_{\underline{k}} \sum_{\nu\nu'} \left(\Delta N_{\nu\nu'}^{(\underline{k})} + n_{\underline{k}\nu}\, \delta_{\nu\nu'} \right) \\ &\cdot \sum_{\mu lm} \left(\beta_{\mu lm}^{\underline{k}\nu'} \right)^* \left(\phi_{\mu lm}^{\underline{k}}(\underline{r}) \right)^* \sum_{\mu' l' m'} \beta_{\mu' l' m'}^{\underline{k}\nu} \phi_{\mu' l' m'}^{\underline{k}}(\underline{r}) \end{aligned} \tag{4.36}$$

is readily written in an atom-centred basis of cubic harmonics with no contributions for $\mu \neq \mu'$. Therefore a similar expression can be found in a straightforward way:

$$n_{(3)}^{\mathrm{DMFT}}(\underline{r}) = \sum_{\underline{T}\mu lm} n_{(2)}^{\mu lm}(|\underline{r}'|)\, \mathrm{K}_{lm}(\widehat{\underline{r}}') \tag{4.37}$$

$$\text{with} \quad \underline{r}' = \underline{r} - \underline{T} - \underline{R}_\mu$$

$$\begin{aligned} n_{(3)}^{\mu lm}(|\underline{r}'|) &= \sum_{l_1 m_1} \sum_{l_2 m_2} g_{l_1,l_2,l}^{m_1,m_2,m} f_{\mu l_1}(|\underline{r}'|) f_{\mu l_2}(|\underline{r}'|) \mathrm{i}^{l_2-l_1} \\ &\cdot \sum_{\underline{k}} \sum_{\nu\nu'} \left(\Delta N_{\nu\nu'}^{(\underline{k})} + n_{\underline{k}\nu}\, \delta_{\nu\nu'} \right) \left(\beta_{\mu l_1 m_1}^{\underline{k}\nu'} \right)^* \beta_{\mu l_2 m_2}^{\underline{k}\nu} \end{aligned} \tag{4.38}$$

A final note concerns the exploitation of crystal symmetries, which are extensively used in the mixed-basis pseudopotential implementation. Using crystal symmetries, it can be sufficient to calculate wave

functions and energy eigenvalues not for the whole first Brillouin zone, but only in a part thereof, which is named the irreducible Brillouin zone (IBZ) wedge. All N_{sym} crystal symmetries of a system in question form the space group $\{T_\alpha|\underline{t}_\alpha\}$ of point symmetry operations T_α and the corresponding nonprimitive translation vectors $\underline{t}_\alpha$. So all $\underline{k}$-points that can be mapped to each other by one of the T_α (symmetry-equivalent $\underline{k}$-points) have the same energy eigenvalues. Furthermore, the corresponding wave functions can be reconstructed as follows [Mey98]:

$$\psi_{T_\alpha(\underline{k})\,\nu}(\underline{r}) = \psi_{\underline{k}\nu}(T_\alpha^{-1}(\underline{r}-\underline{t}_\alpha)) \tag{4.39}$$

For the charge density difference $\Delta n(\underline{r})$ as given by (4.28), this implies:

$$\Delta n(\underline{r}) = \sum_{\underline{k}\in\mathrm{IBZ}} \sum_{\nu\nu'\in\mathcal{W}} \Delta N_{\nu\nu'}^{(\underline{k})} \frac{w_{\underline{k}}}{N_{\mathrm{sym}}} \sum_{\alpha=1}^{N_{\mathrm{sym}}} \psi^*_{\underline{k}\nu'}(T_\alpha^{-1}(\underline{r}-\underline{t}_\alpha))\, \psi_{\underline{k}\nu}(T_\alpha^{-1}(\underline{r}-\underline{t}_\alpha)) \tag{4.40}$$

The fraction

$$\frac{w_{\underline{k}}}{N_{\mathrm{sym}}}$$

relating the number $w_{\underline{k}}$ of symmetry-equivalent counterparts of each $\underline{k}$-point and the total number of symmetries N_{sym} is not necessarily unity. So for the actual calculation, one can use the following expressions:

$$\Delta n(\underline{r}) = \frac{1}{N_{\mathrm{sym}}} \sum_{\alpha=1}^{N_{\mathrm{sym}}} \Delta\tilde{n}(T_\alpha^{-1}(\underline{r}-\underline{t}_\alpha)) \tag{4.41}$$

$$\Delta\tilde{n}(\underline{r}) = \sum_{\underline{k}\in\mathrm{IBZ}} \sum_{\nu\nu'\in\mathcal{W}} w_{\underline{k}}\, \Delta N_{\nu\nu'}^{(\underline{k})}\, \psi^*_{\underline{k}\nu'}(\underline{r})\, \psi_{\underline{k}\nu}(\underline{r}) \tag{4.42}$$

The same applies to the original charge densities and thus to the whole charge density $n^{\mathrm{DMFT}}(\underline{r})$. So in order to take $\underline{k}$-space symmetries into account, one uses the usual formulas, but replacing $\underline{k}$-space sums by sums over the irreducible wedge only and adding the weight factors $w_{\underline{k}}$ according to (4.42). At the end, one includes a symmetrisation according to (4.41). In the DMFT part of the formalism, symmetries

are less important, since, due to the local nature of DMFT, they have numerical advantages only in the $\underline{k}$-space sums that are done in the beginning according to (2.55). So the matrix $\Delta\underline{\underline{N}}^{(\underline{k})}$ can be provided on the full Brillouin zone, from which only the points in the irreducible wedge are actually used.

4.2.3 A first example

After the theoretical derivation of an exact formulation of the charge density differences, a short interlude about how the charge density differences look in practice is in place. This is done for Lanthanum nickelate ($LaNiO_3$), a cubic perovskite that exhibits features of strong electronic correlations (see e. g. [DFM$^+$12]), while being easy to handle computationally.

Figure 4.1 shows electronic charge density comparisons of the pure LDA charge density, the charge density of the self-consistency cycle and of the post-processing LDA+DMFT scheme without charge self-consistency. For $LaNiO_3$, a two-orbital e_g correlated subspace $\mathcal{C}$ is built, while the subspace $\mathcal{W}$ of the Bloch space that is used for the projections incorporates all five d-orbital related bands of Nickel. The calculation is done with the mixed-basis pseudopotential implementation and with interaction parameters of $U = 5.0$ eV and $J = 1.0$ eV. One can see the expected charge density redistribution features, such as charge transfer from the interstitial region and the Oxygen atoms towards the Nickel atom and a redistribution of the Nickel orbital occupations. These effects are slightly reversed from post-processing to charge self-consistent LDA+DMFT (note the scale that differs almost by one order of magnitude).

4.3 Chemical potential

In section 4.2, it has been left open how exactly the chemical potential μ is adjusted. In principle, the answer is trivial, μ has to be found

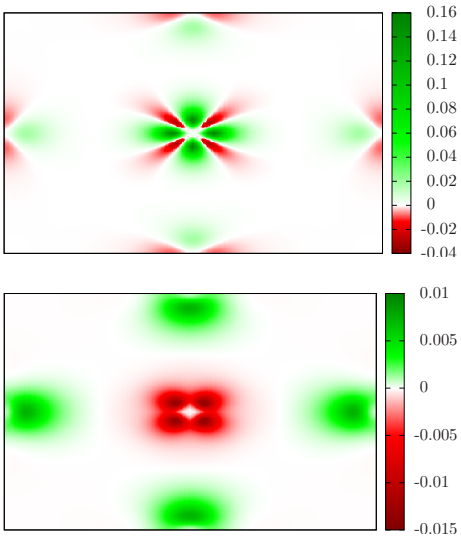

Figure 4.1: Electronic charge density differences for $LaNiO_3$, visualised by cuts through a plane containing one Nickel atom (centre) and the surrounding Oxygen atoms. Top: Difference $n^{\mathrm{CSC}}_{\mathrm{DMFT}}(\underline{r}) - n_{\mathrm{LDA}}(\underline{r})$ of the electronic charge densities of LDA+DMFT with charge self-consistency and of pure LDA. Bottom: Difference $n^{\mathrm{PP}}_{\mathrm{DMFT}}(\underline{r}) - n^{\mathrm{CSC}}_{\mathrm{DMFT}}(\underline{r})$ of the electronic charge densities of post-processing LDA+DMFT and of LDA+DMFT with charge self-consistency.

such that the resulting total DMFT charge density $n^{\mathrm{DMFT}}(\underline{r})$ holds the correct total number of electrons N:

$$\int \mathrm{d}^3 r \, n^{\mathrm{DMFT}}(\underline{r}) = N \tag{4.43}$$

However, in order to find the correct value of μ efficiently and provide a physical interpretation of the quantities that occur in the formalism, numerous reformulations and simplifications can be made, that will be presented in the following section.

To begin with, equation (4.43) can equivalently be written in a Green's function formulation:

$$\frac{1}{\beta}\mathrm{Tr}\left[\sum_{\underline{k}\,n} \underline{\underline{G}}^{\mathrm{full}}(\underline{k}, \mathrm{i}\omega_n)\big|_{\mu}\right] = N \tag{4.44}$$

The dimension of the matrix $\underline{\underline{G}}^{\mathrm{full}}(\underline{k}, \mathrm{i}\omega_n)$ corresponds to all bands that are treated in the DFT part of the formalism. As self-energy effects only affect the limited Bloch space $\mathcal{W}$, the matrix is diagonal except in the block corresponding to $\mathcal{W}$:

$$\left(\underline{\underline{G}}^{\mathrm{full}}(\underline{k}, \mathrm{i}\omega_n)\right)^{-1} = \begin{pmatrix} \mathrm{i}\omega_n + \mu - \epsilon_{\underline{k}\nu} & & 0 \\ & \left(\underline{\underline{G}}^{\mathrm{bl}}(\underline{k}, \mathrm{i}\omega_n)\right)^{-1} & \\ 0 & & \mathrm{i}\omega_n + \mu - \epsilon_{\underline{k}\nu} \end{pmatrix} \tag{4.45}$$

Here, $\underline{\underline{G}}^{\mathrm{bl}}(\underline{k}, \mathrm{i}\omega_n)$ is the Green's function of the Bloch space defined in equation (4.2). The trace of the three blocks can thus be calculated seperately:

$$\begin{aligned} \frac{1}{\beta}\mathrm{Tr}\left[\sum_{\underline{k}\,n} \underline{\underline{G}}^{\mathrm{full}}(\underline{k}, \mathrm{i}\omega_n)\big|_{\mu}\right] &= N_{\mathrm{core}} + \frac{1}{\beta}\mathrm{Tr}\left[\sum_{\underline{k}\,n} \underline{\underline{G}}^{\mathrm{bl}}(\underline{k}, \mathrm{i}\omega_n)\big|_{\mu}\right] + N_{\mathrm{up}} \\ &= N_{\mathrm{core}} + N_{\mathrm{bl}} + N_{\mathrm{up}} \end{aligned} \tag{4.46}$$

The first approximation that can be done is to keep the number of core electrons N_{core} and of electrons in the upper-lying unoccupied bands N_{up} fixed during the calculation and to do the adjustment of the chemical potential μ using $\underline{\underline{G}}^{\mathrm{bl}}(\underline{k}, \mathrm{i}\omega_n)$ only, i. e. within the space $\mathcal{W}$. This procedure has significant numerical advantages, as the dimension of the matrix that has to be inverted repeatedly for each $\underline{k}$-point and each Matsubara frequency ω_n is significantly reduced. Obviously, the chemical potential μ has to be inside the energy range that corresponds to $\mathcal{W}$. As the Matsubara frequency sum of the diagonal blocks simplifies to a Fermi distribution, N_{core} is assumed to be the number

of (fully occupied) bands below $\mathcal{W}$, and N_{up} is assumed to be zero. Note that this assumption can become invalid only due to temperature effects, and is especially reasonable because the space $\mathcal{W}$ is typically chosen in a way that it corresponds to a block of bands seperated by reasonable band gaps. Of course, it has been tested to be a reasonable approximation.

The equation that is (in most cases) finally used in order to find the chemical potential μ is therefore the following:

$$\frac{1}{\beta}\mathrm{Tr}\left[\sum_{\underline{k}\,n}\underline{\underline{G}}^{\mathrm{bl}}(\underline{k},\mathrm{i}\omega_n)\big|_{\mu}\right] = N_{\mathrm{bl}} \tag{4.47}$$

Technically, a dichotomic algorithm is used to find μ based on an initial guess or the value from the previous iteration. In order to avoid inconsistencies, this is done before and after each DMFT step, as mentioned in the introductory overview of the whole cycle.

4.3.1 μ^{KS}

In the above derivations, the choice of a further useful quantity that is denoted μ^{KS} has been left open. As mentioned, this quantity should not be understood as a "second" chemical potential, the chemical potential μ of the system is a unique physical observable. μ^{KS} itself has no physical interpretation, thus it can be thought of as an auxiliary quantity that can in principle be chosen arbitrarily. However, one useful choice is to calculate it using equation (4.47), but substituting $\underline{\underline{G}}^{\mathrm{bl}}(\underline{k},\mathrm{i}\omega_n)$ by $\underline{\underline{G}}^{\mathrm{KS}}(\underline{k},\mathrm{i}\omega_n)$ as defined in equation (4.4):

$$\frac{1}{\beta}\mathrm{Tr}\left[\sum_{\underline{k}\,n}\underline{\underline{G}}^{\mathrm{KS}}(\underline{k},\mathrm{i}\omega_n)\big|_{\mu^{\mathrm{KS}}}\right] = N_{\mathrm{bl}} \tag{4.48}$$

This choice can be used to clarify relations between some of the quantities that occur in the formalism. As $\underline{\underline{G}}^{\mathrm{KS}}(\underline{k},\mathrm{i}\omega_n)$ is defined to be equal

to $\underline{\underline{G}}^{\mathrm{bl}}(\underline{k}, \mathrm{i}\omega_n)$, but without the self-energy term, it is purely diagonal (in band indices) and the corresponding electron density $n^{\mathrm{KS}}(\underline{r})$ is simply expressed in Kohn-Sham wave functions $\psi_{\underline{k}\nu}(\underline{r})$ with occupation numbers corresponding to a Fermi distribution function $f(\epsilon_{\underline{k}\nu} - \mu^{\mathrm{KS}})$:

$$n^{\mathrm{KS}}(\underline{r}) = \sum_{\underline{k}\,\nu} f(\epsilon_{\underline{k}\nu} - \mu^{\mathrm{KS}}) \, |\psi_{\underline{k}\nu}(\underline{r})|^2 \tag{4.49}$$

So, with this choice of μ^{KS}, $n^{\mathrm{KS}}(\underline{r})$ itself is normalised to the total number of electrons N in the system (keeping in mind the approximations listed above):

$$\int \mathrm{d}^3 r \, n^{\mathrm{KS}}(\underline{r}) = N \tag{4.50}$$

So the integral over the charge density difference $\Delta n(\underline{r})$ vanishes:

$$\int \mathrm{d}^3 r \, \Delta n(\underline{r}) = \int \mathrm{d}^3 r \, n^{\mathrm{DMFT}}(\underline{r}) - \int \mathrm{d}^3 r \, n^{\mathrm{KS}}(\underline{r}) = N - N = 0 \tag{4.51}$$

This means that the effect of strong electronic correlations attributed to DMFT is represented as a redistribution of charge density only, which gives an intuitive approach to the charge densities in question. Technically, this choice permits the simplification that $n^{\mathrm{KS}}(\underline{r})$ is exactly the charge density that also the pure DFT part would find, including its normalisation, so no adjustment of the charge density integration thereof has to be made.

A second possible intuitive choice of μ^{KS} would be not to allow for an additional auxiliary quantity in the formalism, so to choose $\mu^{\mathrm{KS}}_{(2)}$ equal to the chemical potential:

$$\mu^{\mathrm{KS}}_{(2)} \equiv \mu \tag{4.52}$$

The advantage of this second choice is that no correction term occurs in the calculation of the matrix $\Delta \underline{\underline{N}}^{(\underline{k})}_{(2)}$:

$$\Delta \underline{\underline{N}}^{(\underline{k})}_{(2)} = \frac{1}{\beta} \sum_n \left(\underline{\underline{G}}^{\mathrm{KS}}_{(2)}(\underline{k}, \mathrm{i}\omega_n) \cdot \Delta \underline{\underline{\Sigma}}^{\mathrm{bl}}(\underline{k}, \mathrm{i}\omega_n) \cdot \underline{\underline{G}}^{\mathrm{bl}}(\underline{k}, \mathrm{i}\omega_n) \right) \tag{4.53}$$

In this equation, the following definition is used:

$$\underline{\underline{G}}^{\mathrm{KS}}_{(2)}(\underline{k}, \mathrm{i}\omega_n) = \left[(\mathrm{i}\omega_n + \mu)\, \underline{\underline{1}} - \underline{\underline{\epsilon}}_{\underline{k}} \right]^{-1} \tag{4.54}$$

By comparison with (4.2), one can directly see the following identity:

$$\left(\underline{\underline{G}}^{\mathrm{KS}}_{(2)}(\underline{k}, \mathrm{i}\omega_n) \right)^{-1} - \left(\underline{\underline{G}}^{\mathrm{bl}}(\underline{k}, \mathrm{i}\omega_n) \right)^{-1} = \Delta \underline{\underline{\Sigma}}^{\mathrm{bl}}(\underline{k}, \mathrm{i}\omega_n) \tag{4.55}$$

So with this choice, $\underline{\underline{G}}^{\mathrm{KS}}_{(2)}$ has some similarities with the DMFT "Weiss field" $\mathcal{G}_0$, although it is still not the same quantity. The matrices $\Delta \underline{\underline{N}}^{(\underline{k})}_{(2)}$ and $\Delta \underline{\underline{N}}^{(\underline{k})}$ differ only by a shift of their diagonal elements and the resulting charge densities $n^{\mathrm{DMFT}}(\underline{r})$ are, of course, identical for both choices. However, with the second choice, one has to pay attention that all charge density integrations, especially in the DFT part, are made with the chemical potential μ. This has been checked to work equally well, but usually the first choice is preferred in this work for technical reasons.

4.4 Spectral density functional theory

It is justified to ask the question whether at all the charge self-consistency cycle converges and whether the solution is unique or depends on the input quantities that are used. In order to approach an answer to this question, it is instructive to look at the spectral density functional theory by Savrasov and Kotliar [SK04, SHK06], which is based on a Baym-Kadanoff functional [BK61, Bay62]. It uses the following functional Ω [PABG07] that depends on the fundamental quantities of both parts of the formalism, namely the impurity Green's function $\underline{\underline{G}}^{\mathrm{imp}}$ and the charge density n of the self-consistency cycle, as well as the "sources" v_{eff}, which is the effective Kohn-Sham potential, and the double-counting corrected impu-

rity self-energy $\Delta\underline{\underline{\Sigma}}^{\mathrm{imp}}(\mathrm{i}\omega_n) = \underline{\underline{\Sigma}}^{\mathrm{imp}}(\mathrm{i}\omega_n) - \underline{\underline{\Sigma}}^{\mathrm{dc}}$:

$$\begin{aligned}\Omega(\underline{\underline{G}}^{\mathrm{imp}}, n; v_{\mathrm{eff}}, \Delta\underline{\underline{\Sigma}}^{\mathrm{imp}}) &= \mathrm{Tr}\ln\left(\mathrm{i}\omega_n + \mu - \hat{T}_{\mathrm{S}} - v_{\mathrm{eff}}(\underline{r}) - \Delta\underline{\underline{\Sigma}}^{\mathrm{bl}}\right) \\ &- \int \mathrm{d}^3 r\ \left(v_{\mathrm{eff}}(\underline{r}) - v(\underline{r})\right) n(\underline{r}) \\ &- \mathrm{Tr}\left[\Delta\underline{\underline{\Sigma}}^{\mathrm{imp}}(\mathrm{i}\omega_n) \cdot \underline{\underline{G}}^{\mathrm{imp}}(\mathrm{i}\omega_n)\right] \\ &+ E_{\mathrm{H}}[n(\underline{r})] + E_{\mathrm{XC}}[n(\underline{r})] \\ &+ \Phi_{\mathrm{DMFT}}[\underline{\underline{G}}^{\mathrm{imp}}(\mathrm{i}\omega_n)] - \Phi_{\mathrm{dc}}[\underline{\underline{G}}^{\mathrm{imp}}(\mathrm{i}\omega_n)]\end{aligned} \tag{4.56}$$

In this equation, $\hat{T}_{\mathrm{S}}$ is the kinetic part of the DFT Kohn-Sham Hamilton operator, and $v(\underline{r})$ is the external potential (due to the nuclei, which, of course, remain fixed). The Hartee and exchange-correlation energies E_{H} and E_{XC} are defined in (2.11) and (2.12). Φ_{DMFT} is the generating functional of DMFT, which is known to exist via the sum of all local two-particle irreducible skeleton diagrams, but is practically not useful. Likewise, Φ_{dc} creates the double-counting correction.

First of all, minimisation with respect to the source terms does reveal that the charge density n becomes the charge density n^{DMFT} defined by (4.9) for the charge self-consistency cycle and that the impurity Green's function $\underline{\underline{G}}^{\mathrm{imp}}$ becomes the projected local Green's function (2.101). So a new functional Γ can be defined, in which the source terms are Lagrange multiplier functions of the other variational parameters to ensure these two findings. Concretely, the double-counting corrected self-energy $\Delta\underline{\underline{\Sigma}}^{\mathrm{imp}}$ directly depends on the impurity Green's function $\underline{\underline{G}}^{\mathrm{imp}}$ and the DFT potentials $v_{\mathrm{eff}}(\underline{r})$ and $v(\underline{r})$ depend on the charge density n^{DMFT}:

$$\Gamma(\underline{\underline{G}}^{\mathrm{imp}}, n^{\mathrm{DMFT}}) \equiv \Omega(\underline{\underline{G}}^{\mathrm{imp}}, n^{\mathrm{DMFT}}; v_{\mathrm{eff}}[n^{\mathrm{DMFT}}], \Delta\underline{\underline{\Sigma}}^{\mathrm{imp}}[\underline{\underline{G}}^{\mathrm{imp}}]) \tag{4.57}$$

So the result of the minimisation of the functional Γ with respect to the impurity Green's function $\underline{\underline{G}}^{\mathrm{imp}}$ is:

$$\underline{\underline{\Sigma}}^{\mathrm{imp}}(\mathrm{i}\omega_n) - \underline{\underline{\Sigma}}^{\mathrm{dc}} = \frac{\delta\,\Phi_{\mathrm{DMFT}}[\underline{\underline{G}}^{\mathrm{imp}}(\mathrm{i}\omega_n)]}{\delta\underline{\underline{G}}^{\mathrm{imp}}(\mathrm{i}\omega_n)} - \frac{\delta\,\Phi_{\mathrm{dc}}[\underline{\underline{G}}^{\mathrm{imp}}(\mathrm{i}\omega_n)]}{\delta\underline{\underline{G}}^{\mathrm{imp}}(\mathrm{i}\omega_n)} \tag{4.58}$$

This is exactly the DMFT self-consistency condition written via the generating functionals. Minimisation with respect to n^{DMFT} yields:

$$v_{\mathrm{eff}}(\underline{r}) - v(\underline{r}) = \frac{\delta E_{\mathrm{H}}[n^{\mathrm{DMFT}}(\underline{r})]}{\delta n^{\mathrm{DMFT}}(\underline{r})} + \frac{\delta E_{\mathrm{XC}}[n^{\mathrm{DMFT}}(\underline{r})]}{\delta n^{\mathrm{DMFT}}(\underline{r})} \tag{4.59}$$

This is exactly the definition (2.14) and (2.15) of the Hartree and exchange-correlation potential of the DFT self-consistency cycle. So the minimisation of Ω does produce the described fully self-consistent cycle. Of course, the existence of a generating functional does not guarantee the existence and uniqueness of its solution. In contrast, in chapter 5 some cases in which several minima for the same problem (close to a phase transition) exist. However, this generating functional can be thought of as a further justification thereof.

4.5 Energetics of LDA+DMFT

The true strength of the functional Γ given in the previous section is that from its minimised value it becomes possible to define a total energy functional of the charge self-consistency cycle. It can be derived from (4.57) as [PABG07]:

$$\begin{aligned} E_{\mathrm{LDA+DMFT}} &= \sum_{\underline{k}} \sum_{\nu\nu'} \epsilon_{\underline{k}\nu} \delta_{\nu\nu'} \, n^{\mathrm{bl}}_{\underline{k}\nu\nu'} \\ &- \int \mathrm{d}^3 r \, \left(v_{\mathrm{eff}}(\underline{r}) - v(\underline{r}) \right) n^{\mathrm{DMFT}}(\underline{r}) \\ &+ E_{\mathrm{H}}[n^{\mathrm{DMFT}}(\underline{r})] + E_{\mathrm{XC}}[n^{\mathrm{DMFT}}(\underline{r})] \\ &+ \langle \hat{H}^{\mathrm{int}} \rangle - E_{\mathrm{dc}} \end{aligned} \tag{4.60}$$

This representation makes use of the Bloch basis in which the kinetic Hamilton operator consists of the diagonal matrix of Kohn-Sham energy eigenvalues $\epsilon_{\underline{k}\nu}$. Since the first four terms are nothing else than the evaluation of the standard DFT functional at the self-consistently determined charge density $n^{\mathrm{DMFT}}(\underline{r})$, the practical calculation of the

total energy becomes very simple:

$$E_{\mathrm{LDA+DMFT}} = E_{\mathrm{LDA}}[n^{\mathrm{DMFT}}(\underline{r})] + \sum_{\underline{k}} \sum_{\nu \in \mathcal{W}} \epsilon_{\underline{k}\nu} \, \Delta N_{\nu\nu}^{(\underline{k})} + \langle \hat{H}^{\mathrm{int}} \rangle - E_{\mathrm{dc}} \tag{4.61}$$

So it can be seen that the second term therein (the band energy correction term) addresses the band energy term of DFT, in which one has to pay attention that its calculation uses the correct occupation numbers of the Kohn-Sham states. These occupation number corrections exactly correspond to the matrix $\Delta \underline{\underline{N}}^{(\underline{k})}$. Again due to the Bloch basis, only the diagonal terms thereof are needed.

The third term is the expectation value of the interacting Hamilton operator used in DMFT. It arises from Γ via the use of the Galitskii-Migdal formula [GM58] (see [FW71] for a derivation):

$$\langle \hat{H}^{\mathrm{int}} \rangle = \frac{1}{2} \sum_{n} \mathrm{Tr} \left[\underline{\underline{\Sigma}}^{\mathrm{imp}}(\mathrm{i}\omega_n) \cdot \underline{\underline{G}}^{\mathrm{imp}}(\mathrm{i}\omega_n) \right] \tag{4.62}$$

So this expectation value is evaluated entirely in the (small) impurity space. However, as one can easily see, an equivalent (but numerically less efficient) formulation thereof in Bloch space is possible, since the trace operator is invariant under cyclic permutations, also for matrices that are not quadratic:

$$\begin{aligned} \langle \hat{H}^{\mathrm{int}} \rangle &= \frac{1}{2} \sum_{n\,\underline{k}} \mathrm{Tr} \left[\underline{\underline{\Sigma}}^{\mathrm{imp}}(\mathrm{i}\omega_n) \cdot \underline{\underline{P}}(\underline{k}) \, \underline{\underline{G}}^{\mathrm{bl}}(\underline{k}, \mathrm{i}\omega_n) \, \underline{\underline{P}}^{\dagger}(\underline{k}) \right] \\ &= \frac{1}{2} \sum_{n\,\underline{k}} \mathrm{Tr} \left[\underline{\underline{P}}^{\dagger}(\underline{k}) \, \underline{\underline{\Sigma}}^{\mathrm{imp}}(\mathrm{i}\omega_n) \, \underline{\underline{P}}(\underline{k}) \cdot \underline{\underline{G}}^{\mathrm{bl}}(\underline{k}, \mathrm{i}\omega_n) \right] \\ &= \frac{1}{2} \sum_{n\,\underline{k}} \mathrm{Tr} \left[\underline{\underline{\Sigma}}^{\mathrm{bl}}(\underline{k}, \mathrm{i}\omega_n) \cdot \underline{\underline{G}}^{\mathrm{bl}}(\underline{k}, \mathrm{i}\omega_n) \right] \end{aligned} \tag{4.63}$$

Apart from the Galitskii-Migdal formula, several other techniques to evaluate this expectation value exist. Especially in the quantum Monte-Carlo technique that is used frequently in this work, it is possible to measure expectation values of operators directly in the Monte-Carlo process. Furthermore, especially for simple interacting Hamilton

operators, a connection to the high Matsubara frequency development of the Green's functions can often be made. However, these techniques are not used in the work at hand, since a qualitative difference to the simple Galitskii-Migdal evolution cannot be expected.

Finally, the fourth term is the usual double-counting correction term. This term can equally be calculated with the Galitskii-Migdal formula:

$$E_{\mathrm{dc}} = \frac{1}{2} \sum_{n} \mathrm{Tr} \left[\underline{\underline{\Sigma}}^{\mathrm{dc}} \cdot \underline{\underline{G}}^{\mathrm{imp}}(\mathrm{i}\omega_n) \right] \tag{4.64}$$

Practically, the third and the fourth term are not calculated independently, but the Galitskii-Migdal formula is simply evaluated at a shifted self-energy.

4.6 CSC scheme in RISB

The general approach to combine DFT with explicit many-particle methods in a charge-self-consistent way is not limited to the DMFT formalism. Especially the RISB formalism is suitable for reasonably fast investigations of e. g. large parameter sets. In principle, RISB can be written as an impurity solver for DMFT, which would make it possible to reuse the entire formalism as given above. However, to put a lattice implementation of RISB into play, a direct connection of RISB observables and the charge density can be made, while retaining the overall ideas of the charge-self-consistency cycle. This work has principally been done by Christoph Piefke, who will show all details thereof in his PhD thesis, while only a short summary is shown here.

To begin with, the projection onto localised orbitals formalism shown in section 2.3.2 has to be adapted slightly, because RISB is entirely written in terms of Hamilton operators. Although it would be possible to rewrite the formalism in terms of Greens's functions, this approach is not used because it would significantly increase the numerical requirements. For instance, the calculation of the chemical potential, which is done in each step of the minimisation process,

would require matrix inversions for each Matsubara frequency instead of only for one Hamilton operator. Therefore a Hamilton operator $\underline{\underline{H}}^{\mathrm{bl}}(\underline{k})$ is constructed from the projection matrices for each point in $\underline{k}$-space:

$$\underline{\underline{H}}^{\mathrm{bl}}(\underline{k}) = \underline{\underline{\epsilon}}_{\underline{k}} - \underline{\underline{P}}^{\dagger}(\underline{k})\,\underline{\underline{H}}^{\mathrm{kin}}(\underline{k})\,\underline{\underline{P}}(\underline{k}) + \underline{\underline{P}}^{\dagger}(\underline{k})\,\underline{\underline{H}}^{\mathrm{C}}\,\underline{\underline{P}}(\underline{k}) \tag{4.65}$$

(4.65) is written in the unprojected Bloch space. Thus, $\underline{\underline{\epsilon}}_{\underline{k}}$ denotes the diagonal unrenormalised Hamilton operator in Bloch space. Since the renormalised quantities in the smaller projected space cannot be upfolded directly, the idea is to substract the downfolded unrenormalised Hamilton operator $\underline{\underline{H}}^{\mathrm{kin}}(\underline{k})$ and "replace" its contributions by the renormalised Hamilton operator. Thus, $\underline{\underline{H}}^{\mathrm{kin}}(\underline{k})$ is defined as follows:

$$\underline{\underline{H}}^{\mathrm{kin}}(\underline{k}) = \underline{\underline{P}}(\underline{k})\,\underline{\underline{\epsilon}}_{\underline{k}}\,\underline{\underline{P}}^{\dagger}(\underline{k}) \tag{4.66}$$

Consequently, $\underline{\underline{H}}^{\mathrm{C}}$ stands for the renormalised (correlated) free Hamilton operator that enters the minimisation process of RISB (see (2.81)). In the limit of quadratic projections (the Bloch space has the same size as the projected space), the projection matrices are unitary ($\underline{\underline{P}}^{\dagger}(\underline{k}) \cdot \underline{\underline{P}}(\underline{k}) = \underline{\underline{P}}(\underline{k}) \cdot \underline{\underline{P}}^{\dagger}(\underline{k}) = \underline{\underline{1}}$) and this formulation correctly uses directly the upfolded renormalised Hamilton operator.

The charge self-consistent formalism can be formulated using the same matrices $\Delta\underline{\underline{N}}^{(\underline{k})}$ as in DMFT. However, they are not calculated in terms of Green's functions and self-energies, but of equivalent expressions intrinsic to the RISB formalism. For this purpose, one can recall the original definition of $\Delta\underline{\underline{N}}^{(\underline{k})}$ in terms of occupation numbers as given in (4.8). As it can easily be verified, occupation numbers can be projected in the same way as the original Hamilton operator they stem from:

$$\underline{\underline{n}}_{\underline{k}} = \underline{\underline{n}}_{\underline{k}}^{\mathrm{KS}} - \underline{\underline{P}}^{\dagger}(\underline{k})\underline{\underline{P}}(\underline{k})\,\underline{\underline{n}}_{\underline{k}}^{\mathrm{KS}}\,\underline{\underline{P}}^{\dagger}(\underline{k})\underline{\underline{P}}(\underline{k}) + \underline{\underline{P}}^{\dagger}(\underline{k})\,\underline{\underline{n}}_{\underline{k}}^{\mathrm{C}}\,\underline{\underline{P}}(\underline{k}) \tag{4.67}$$

The "easy verification" is that the natural way to calculate occupation numbers is to fill up occupied states (according to an appropriate

smearing function) of the diagonalised Hamilton operator and then rotate them back into the original basis. These operations commute with the projection of the Hamilton operators, provided that the correct chemical potential is used in each term. In (4.67), the correlated occupation numbers $\underline{\underline{n}}^{\mathrm{C}}_{\underline{k}}$ are direct output quantities of RISB, whereas the other terms are calculated with the mentioned diagonalisation-rotation-scheme. The matrices $\Delta\underline{\underline{N}}^{(\underline{k})}$ are easily constructed from the occupation numbers by omission of the uncorrelated Bloch space occupations $\underline{\underline{n}}^{\mathrm{KS}}_{\underline{k}}$, again taking care of the usage of the correct chemical potential:

$$\Delta\underline{\underline{N}}^{(\underline{k})} = \underline{\underline{P}}^{\dagger}(\underline{k})\,\underline{\underline{n}}^{\mathrm{C}}_{\underline{k}}\,\underline{\underline{P}}(\underline{k}) - \underline{\underline{P}}^{\dagger}(\underline{k})\underline{\underline{P}}(\underline{k})\,\underline{\underline{n}}^{\mathrm{KS}}_{\underline{k}}\,\underline{\underline{P}}^{\dagger}(\underline{k})\underline{\underline{P}}(\underline{k}) \tag{4.68}$$

These can be used to build up the same cycle as in the self-consistent LDA+DMFT scheme.

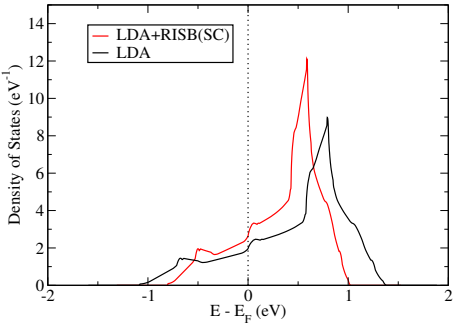

Figure 4.2: Comparison of the total RISB Bloch space quasi-particle density of states in the charge self-consistent cycle (red) with the original LDA quasi-particle density of states (black) for Strontium Vanadate ($SrVO_3$). The energies are given with respect to the Fermi energy obtained in each method.

As a first result, figure 4.2 shows the total RISB Bloch space quasi-particle density of states in the charge self-consistent cycle with the

MBPP code compared to the original LDA quasi-particle density of states for Strontium Vanadate ($SrVO_3$). This is a prototypical example for calculational techniques for strongly correlated electrons, because a well-defined correlated subspace can be extracted from three well-separated degenerate bands at the Fermi level, corresponding to d_{xz}, d_{yz} and d_{xy} orbitals. Furthermore, cubic symmetry prevents off-diagonal elements of its Green's function or renormalisation matrices. The most simple case of quadratic projection matrices is shown; the interaction parameters are chosen as $U = 4.0$ eV and $J = 0.65$ eV. One can recognise the expected features of RISB, especially the renormalisation of the band width and a small shift thereof. Due to the saddle-point approximation in the RISB formalism, Hubbard bands cannot be seen with this approach.

Five

Phase transitions in Vanadium Sesquioxide

Vanadium sesquioxide (V_2O_3) has been subject to numerous experimental and theoretical studies in the past, investigating its strongly correlated nature. Although it shows several interesting phase transitions, both temperature and (negative) pressure driven, the reason for its popularity is mainly the metal-insulator transition with (negative) pressure, which can be thought of as archetypical for the Mott metal-insulator transition. This transition is also the main topic of the work shown in this section, which has been published in [GPPL12]. The intrinsic temperature dependence of the charge self-consistency formalism and the possibility to calculate total energies for the first time allow for the (close to) ab-initio description of the complete pressure and temperature dependence of this phase transition, including its characterisation as a first-order transition.

5.1 Introduction to experimental findings

The experimental phase diagram that is the basis of the work shown here as well as of numerous other theoretical studies of this material has been published already in 1971 and 1973 [MRR$^+$71, MMR$^+$73] and is shown in figure 5.1. At ambient temperature and pressure, V_2O_3

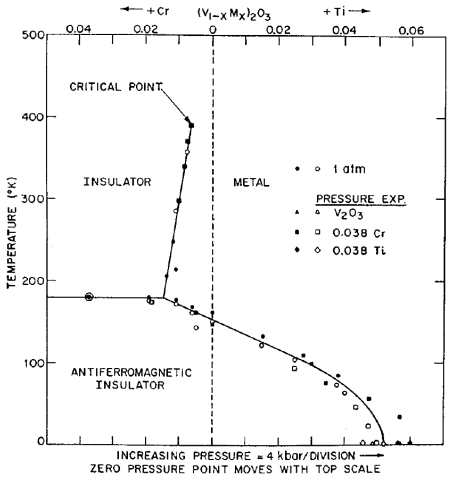

Figure 5.1: Experimental phase diagram of V_2O_3 taken from [MRR$^+$71, MMR$^+$73].

is a paramagnetic metal. With decreasing temperature, a sharp first order transition to an antiferromagnetic insulating solution occurs at $T_C \sim 150$ K - 162 K. These findings can be included in a more general two-dimensional phase diagram with temperature and pressure, for which an empirical relation between pressure and doping ("chemical pressure") is assumed (one percent of doping corresponds to a pressure change of 4 kbar). The Vanadium substituents that are used for this purpose are typically Titanium for "positive" pressure and Chromium for (experimentally not directly feasible) "negative" pressure, but also elements like Zirconium, Magnesium or Iron have been used for comparison. One has to note that these substituents are not isovalent to Vanadium, thus, one can assume that it is not only the steric effect of a smaller/larger ionic radius that plays a role for the phase transitions in question. While the effect of positive pressure/Titanium doping is basically to lower the transition temperature towards the antiferromag-

netic insulating ground state until it is completely suppressed at about five percent of doping, the negative pressure/Chromium doping regime incorporates a new paramagnetic insulating phase, characterised as a Mott insulator. The first order phase transition from the paramagnetic metallic to the paramagnetic insulating phase shows a characteristic slope; larger doping (higher negative pressure) is required for smaller temperatures, so that one could realise an insulator-metal-transition with temperature at a fixed doping. A critical end point of the metal-insulator transition is reached at about 380 K. The antiferromagnetic insulating phase remains the ground state and the transition temperature from the paramagnetic insulating phase is roughly pressure independent. A further phase not displayed in the phase diagram has been reported for the Vanadium-deficient $V_{2-y}O_3$ compound, which undergoes a spin density wave ordering below a Néel temperature of $T_N \sim 9$ K with an incommensurate wave vector of $q \sim 1.7c^*$ [BBC+93].

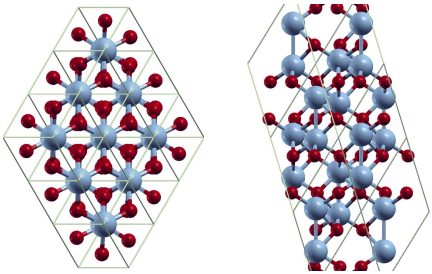

Figure 5.2: Crystal structure of paramagnetic V_2O_3 seen along the z-axis (left) and along the y-axis (right). The larger blue spheres symbolise Vanadium, the smaller red spheres symbolise Oxygen atoms.

Vanadium sesquioxide crystallises in the corundum (Al_2O_3) structure, which has trigonal (rhombohedral) symmetry with the space group $R\overline{3}c$. The structure can be characterised by almost hexagonally closed packed oxygen atoms, in which the Vanadium atoms occupy $\frac{2}{3}$

of the octahedral sites [DM70]. This leads to Vanadium honeycomb lattice planes perpendicular to the z axis and Vanadium dimers in z-direction, as can be seen in figure 5.2. The paramagnetic metallic and insulating phases are isostructural, but discontinuous jumps of the unit cell volume as well as a (comparatively high) ratio of the lattice parameters $\frac{c}{a}$ have been reported [Der70, MR70, RRS+11]. In contrast, the low-temperature antiferromagnetic ordering incorporates a structural transition to a monoclinic structure with space group $I2/a$ and a doubling of the unit cell [War60].

In principle, the aim of this work is to reproduce all qualitative features of the phase diagram shown in figure 5.1. To begin with, the focus is on the paramagnetic Mott metal-insulator transition. The motivation for this course of action is that the remaining antiferromagnetic phase is the ground state of pure LDA calculations already and appears to be closely connected to the structural transition and additional orbital ordering, as comparisons with the spin-density wave ground state suggest [BBA+97]. On the other hand, the Mott transition seems to be more closely related to strong electronic correlations and thus will be more appealing for the methods of this work. The investigation of the antiferromagnetic ground state is therefore postponed to later studies.

5.2 The density functional theory picture

First of all, the best approach to choose for the description of the phase diagram in question is not as clear as, for instance, for the Vanadium chalcogenide comparison of chapter 3. Concerning the temperature axis, density functional theory, as a ground state theory, is not expected to provide significant information, although a (formal) temperature dependence can be included via Mermin theory [Mer65]. Therefore the temperature dependence is completely postponed to the DMFT description and its charge self-consistent formulation.

The more delicate question is how the doping/pressure axis can be modeled. Since the transition line appears similar to the corresponding metal-insulator transition in the U versus temperature phase diagram of the simple Hubbard model (see e. g. [GKKR96, JO01]), some previous studies (e. g. [HKE$^+$01, PTB$^+$07]) neglected the pressure/doping influence completely in the underlying density functional theory calculations and empirically attributed the pressure/doping influence to a higher effective value of U. However, this approach does not seem to be justified for a comprehensive description, since the effective U value can be understood as an overlap integral of on-site orbitals modulated by screening effects and thus, at first glance, is not expected to be significantly modified by e. g. substitution of neighbouring atoms. Furthermore, a recent photoemission study [FSM$^+$11] could confirm a constant value of U across the metal-insulator transition. The physically most accurate description of doping would be to use large supercells for all density functional theory calculations, large enough to be able to substitute the correct part of Vanadium atoms by Chromium atoms. This approach still does not take into account effects like clustering of the Chromium atoms, and it is computationally already very demanding, as a typical density functional theory calculation can be estimated to scale cubically with the system size. Furthermore, this significantly increases the calculation time needed for the follow-up DMFT investigations, since the Vanadium atoms of these large supercells are, by construction, no longer equivalent by symmetry and thus almost all of them have to be treated individually. For this reason, the empirical relation between pressure and doping will be exploited. Pressure can be modeled in a straightforward way in density functional theory by altering (i. e. enlarging, because of negative pressure) the unit cell volume. Of course, this simple model does not provide measurable values for the applied pressure, unless experimentally determined elasticity constants exist. However, this approach is believed to provide a good ab-initio qualitative description of all physically relevant features. One could argue that an enlargement of the lattice constant in turn implies an increase of the effective U because of the

reduction of screening effects. However, such effects are believed to be taken into account, at least as a first approximation, by the charge self-consistent reaction to correlation effects.

The starting structure that is assumed to describe the equilibrium pressure case is constructed from data determined experimentally in [Der70] for undoped V_2O_3. The corundum structure is constructed using the hexagonal lattice constants $a_0 = 4.9515$ Å and $c_0 = 14.003$ Å, resulting in the comparably high $\frac{c}{a}$ ratio of approximately 2.8281 (note that in the ideal case of a hexagonally closed packed crystal, one would obtain a ratio of $\sqrt{\frac{8}{3}} \approx 1.63$). The other necessary structural parameters are a relative z component of the Vanadium atoms (0.3463) and a relative x component of the oxygen atoms (0.31164). If a hexagonal structure was used, one unit cell would contain six formula units of V_2O_3. To reduce the computational effort, an equivalent rhombohedral structure with two formula units (i. e. four Vanadium atoms that are all equivalent by symmetry) per unit cell is used. The lattice vectors of this structure read as follows:

$$\underline{T}_1 = \begin{pmatrix} -\frac{\sqrt{3}}{6}a \\ \frac{1}{2}a \\ \frac{1}{3}c \end{pmatrix} \qquad \underline{T}_2 = \begin{pmatrix} -\frac{\sqrt{3}}{6}a \\ -\frac{1}{2}a \\ \frac{1}{3}c \end{pmatrix} \qquad \underline{T}_3 = \begin{pmatrix} \frac{\sqrt{3}}{3}a \\ 0 \\ \frac{1}{3}c \end{pmatrix} \tag{5.1}$$

In order to simulate pressure, the first possible approach is to enlarge the unit cell volume isostructurally, i. e. enlarge both lattice parameters a and c, while keeping their ratio fixed. This simple approach neglects influences like the observed discontinuous jump of the $\frac{c}{a}$ ratio at the metal-insulator transition [MRR69, Der70, RHR+10, RRS+11] as well as the reported increasing $\frac{c}{a}$ ratio with large positive pressure [FH80]. These influences will, at least partially, be taken into account explicitly later in this chapter.

The following DFT calculations are done with the mixed-basis pseudopotential implementation with an exchange-correlation functional of LDA type using the parametrisation of Perdew and Wang [PW92]. Monkhorst-Pack k-point meshes [MP76] with $13 \times 13 \times 13$ k-points are used, corresponding to 231 k-points in the irreducible wedge

of the Brillouin zone, and integration is carried out by means of the improved tetrahedron integration scheme [BJA94]. A plane-wave cut-off energy of $E_{\mathrm{PW}} = 20$ Ryd is chosen and localised functions are used for Oxygen s and p states as well as Vanadium s, p and d states, while a cut-off for the latter at a radius of 2.0 atomic units is introduced via multiplication with a suitable function.

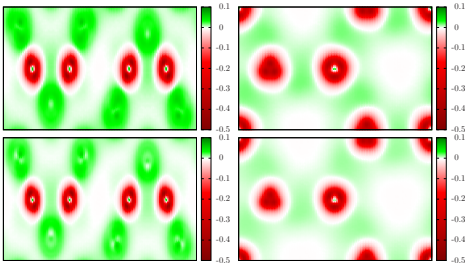

Figure 5.3: Bond charge densities $n(\underline{r}) - n^{\mathrm{atomic}}(\underline{r})$ from LDA of V_2O_3 at the experimentally determined equilibrium lattice constant (top) and at a lattice constant enlarged by a factor of 1.1 (bottom). The left row shows an xz plane cut (Vanadium dimers), the right row an xy-plane cut (honeycomb lattice).

Before starting to discuss the one-particle related output quantities, a short glance on what is actually the basic output of DFT is in order, especially in view of the interrelation between charge self-consistency of DFT and DMFT. So, figure 5.3 shows the bond charge density, i. e. the difference $n(\underline{r}) - n^{\mathrm{atomic}}(\underline{r})$ between the resulting LDA charge density and a mere superposition of atomic charge densities, for two different lattice constants, namely the above-mentioned equilibrium lattice constant a_0 and an enlarged lattice constant of $1.1 \cdot a_0$ (and fixed $\frac{c}{a}$), which will be shown to be in the insulating regime. The bonding charge density, as opposed to the mere (crystal) charge density, has a very intuitive chemical interpretation, as it nicely highlights the charge transfer from the Vanadium atoms (thus showing

as red circles) to the oxygen atoms (thus green), which leads to the formal V^{3+} valency. Furthermore, charge is accumulated in the interstitial region (in between the ions), which can be interpreted as the bonding charge. In the right column of figure 5.3, the Vanadium atoms look different. This is, however, not a sign of broken symmetry, the two visible Vanadium atoms are merely not exactly in one plane, so that only the Vanadium atom directly in the middle of the picuture (or equivalently those in the corners) are precisely in the cut plane. The plots look very similar for the two lattice constants in question (note that the plots always refer to one unit cell, so that the plots for the larger lattice constant are, in principle, rescaled to have the same size as the smaller lattice constant), no qualitiative differences occur, especially, as expected, no signs of a possible metal-insulator transition.

Figure 5.4 shows sample band structures from calculations at the two different lattice constants mentioned above. The equilibrium lattice constant data agrees well with previously published data, e. g. [Mat94]. The overall band structure is similar for both lattice constants and, like for $BaVSe_3$ discussed in chapter 3, resembles the typical band structure of transition metal oxides. The block below -2 eV is created by the ligand valence states, which are 18 oxygen 2p states (from the six ligand atoms per unit cell) here. The 20 Vanadium 3d bands above the oxygen bands (from the four Vanadium atoms per unit cell) show ligand field splitting into an unoccupied block of 8 orbitals pointing towards the oxygen atoms, which is labeled e_g, and a partially occupied block of orbitals pointing towards the oxygen atoms, which is labeled t_{2g}. As opposed to the situation discussed in chapter 3, these three blocks are clearly separated from each other, an observation which makes it easy to motivate the use of a low-energy correlated subspace only. As expected, the one-particle band structure looks metallic for both lattice constants, since a Mott insulating solution cannot be seen therein. The main difference of the two lattice constants is the reduced bandwidth seen in each of the blocks (from about 2.0 eV for the t_{2g} block with experimental lattice constant to

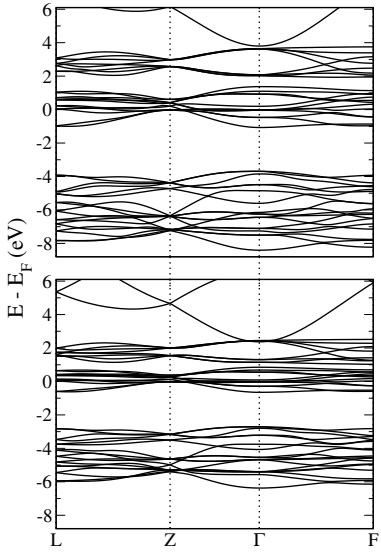

Figure 5.4: One-particle band structure from LDA of V_2O_3 at the experimentally determined equilibrium lattice constant (top) and at a lattice constant enlarged by a factor of 1.1 (bottom).

about 1.5 eV with the enlarged lattice constant), in line with smaller gaps between the blocks. This is again the expected behaviour; in a simple picture, the larger inter-atomic distances correspond to a less itinerant behaviour of the valence electrons or, Fourier transformed, to a smaller bandwidth. This is already the motivation for the over-simplified assumption that the value of U could be increased in the Mott insulating phase, since for pure model studies, a decreased bandwidth happens to be equivalent to a larger value of U.

The LDA one-particle density of states is shown in figure 5.5. The question arises how to find a suitable basis for a correlated subspace that describes the low-energy physics of the system, which is governed by the t_{2g} states. The direct use of cubic harmonics is not sufficient,

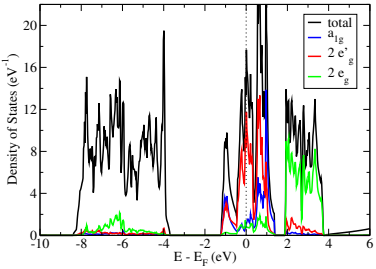

Figure 5.5: Total one-particle density of states of V_2O_3 from LDA at the equilibrium volume and local density of states of Vanadium (cutoff radius r_c=2.0 atomic units) projected onto symmetry-adapted $l = 2$ cubic harmonics (see text for an exact definition).

as all of them (except $d_{3z^2-r^2}$) have weight both on the t_{2g} and on the e_g block. However, one can show [CNR78, SDAN+09] that in the case of the rhombohedral cell used here the following linear combinations thereof transform like the t_{2g} representation of the symmetry group:

$$\begin{aligned} t^1_{2g} = d_{3z^2-r^2} \qquad t^2_{2g} &= \sqrt{\frac{2}{3}} d_{xy} + \frac{\sqrt{3}}{3} d_{xz} \\ t^3_{2g} &= -\sqrt{\frac{2}{3}} d_{x^2-y^2} - \frac{\sqrt{3}}{3} d_{yz} \end{aligned} \tag{5.2}$$

Instead of this symmetry-related basis, a very similar basis is used in this study and is shown in figure 5.5. It is obtained numerically by diagonalisation of the density matrix of the d orbitals and reads as follows:

$$\begin{aligned} t^1_{2g} = d_{3z^2-r^2} \qquad t^2_{2g} &= 0.741282 \cdot d_{xy} + 0.670417 \cdot d_{xz} \\ t^3_{2g} &= -0.741282 \cdot d_{x^2-y^2} - 0.670417 \cdot d_{yz} \end{aligned} \tag{5.3}$$

This basis is typically refered to as crystal field basis. Note that the adaption to the four symmetry-equivalent Vanadium atoms per unit

cell requires a proper choice of the sign of each coefficient for each atom. In order not to introduce an additional degree of freedom, this basis remains fixed throughout the subsequent LDA calculations. This is justified because all subsequent structural variations do not change the symmetry group of the crystal. From figure 5.5, it can be seen that this basis is indeed applicable to capture the low-energy density of states sufficiently well. Furthermore, the $t_{2g}^1 = d_{3z^2-r^2}$ state is indeed nondegenerate with (and higher in energy than) t_{2g}^2 and t_{2g}^3 due to the trigonal field splitting of the not perfectly octahedral environment of oxygen atoms. Therefore, the $t_{2g}^1 = d_{3z^2-r^2}$ state is denoted as a_{1g} and the remaining degenerate t_{2g}^2 and t_{2g}^3 states as e_g' from here on.

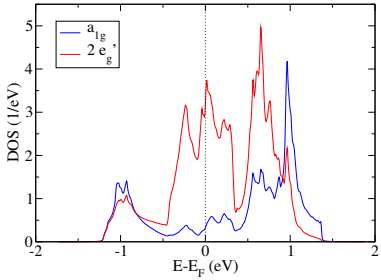

Figure 5.6: LDA density of states of a_{1g} and e_g' of equilibrium-volume V_2O_3 on the basis of the orthonormalized projected local orbitals with a cutoff radius of r_c=2.0 atomic units.

A suitable basis for a correlated subspace is found by means of projections onto localised orbitals (PLO), see section 2.3.2 for details about the method. The localised orbitals (subspace $\mathcal{C}$) are the a_{1g} and e_g' atomic orbitals with a cutoff radius of r_c=2.0 atomic units. The subspace $\mathcal{W}$ of bands used for projection is restricted to the twelve bands of the block surrounding the Fermi level, which is believed to be sufficient since they are clearly separated by a gap from the other blocks and the hybridisation of the orbitals projected onto with the other blocks can be seen to be small from figure 5.5. From the real-

frequency part of the (non-interacting) Green's function that emerges from the projection (after proper normalisation), one can immediately obtain the (non-interacting) density of states thereof, shown in figure 5.6. In addition to a mere consistency check that shows that the features in question from the LDA DOS are reproduced in this minimal basis, this allows for some physical insights into the minimal problem in question. For instance, one can identify the a_{1g} orbital to have the typical DOS of a bonding-antibonding orbital. The occupation numbers of the orbitals in question are approximately 0.57 for the a_{1g} orbital and 0.72 for each of the degenerate e'_g orbitals.

5.3 Unleashing electronic correlations

In order to take into account electronic correlations explicitly, the charge self-consistent combination of the MBPP code and DMFT with the hybridisation-expansion continuous-time quantum Monte Carlo impurity solver is put into play. As motivated above, the interaction parameters U and J are kept fixed at the values used in an older published study [HKE+01], namely $U = 5.0$ eV and $J = 0.93$ eV. As the correlated orbitals are localised on four symmetry-equivalent Vanadium atoms, only one three-orbital impurity model is constructed. The resulting self-energy is symmetrised to all four Vanadium atoms using the ideas presented in section 3.4, thus neglecting inter-atomic self-energy effects. The two-particle part of the Hamilton operator used for the Hubbard model is again the rotationally invariant version (2.50). A double counting correction is in order, which is done in the fully localised limit (2.112). Since a projection scheme in which $\mathcal{W}$ and $\mathcal{C}$ have the same dimension is used, this double counting correction does not have an effect onto spectral properties (it is, in this formulation, merely a shift of the chemical potential), but has an effect onto the values of the total energy of the formalism.

5.3.1 Modelling negative pressure

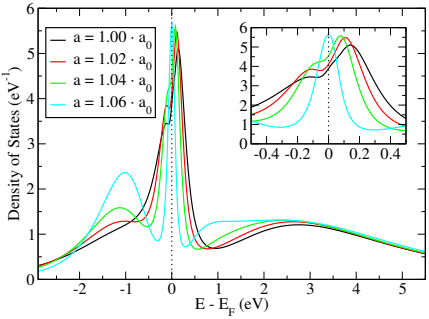

Figure 5.7: The local spectral function of V_2O_3 in the metallic regime with increasing lattice constant (i. e. negative pressure) for a temperature of $T = 387$ K. The inset is an enlargement to show features around the Fermi level more clearly.

The first question that arises is whether an insulating phase can be seen in the charge self-consistent DMFT cycle if one simply enlarges the lattice constant, and whether this phase is a Mott insulator. The first hint is given in figure 5.7, where the local spectral function of DMFT can be seen if the lattice constant is increased gradually at fixed temperature ($T \sim 387$ K or $\beta = (k_B T)^{-1} = 30$ eV^{-1}). It is overall similar to the Vanadium-localised part of experimentally determined photoemission spectra, see e. g. [MDK+03]. The series is stopped before the metal-insulator transition, but one can see the typical features of the Mott transition as described by increasing interaction strength in DMFT, namely the formation of Hubbard bands above and below the Fermi energy and (approximately) the pinning of the quasi-particle peak at the Fermi energy. Thus, one can indeed observe a Mott metal-insulator transition with this approach.

One can now go deeper into the insulating phase and investigate the exact shape of the transition line and particularly its slope with

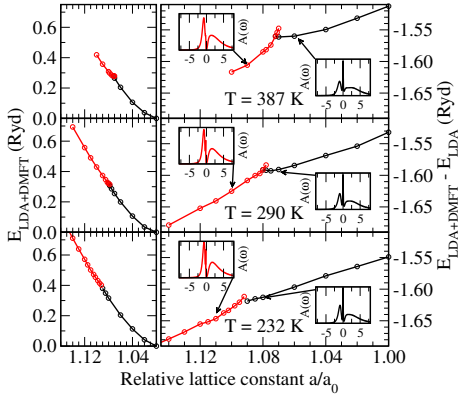

Figure 5.8: Left column: Total energies $E_{\mathrm{LDA+DMFT}}$ of LDA+DMFT as a function of pressure, i. e. lattice constant, for various temperatures. The values are normalised to the value at the experimentally determined lattice constant a_0. Right column: Difference of $E_{\mathrm{LDA+DMFT}}$ and the pure LDA energy E_{LDA} for each lattice constant. Red lines depict insulating solutions, black lines metallic solutions. The insets show local spectral functions for some points at each side of the metal-insulator transition.

negative pressure, which is done in figure 5.8. For this plot, only the lattice constant is varied, all other structural parameters, including the ratio $\frac{c}{a}$, are kept fixed. Thus, the red and black lines in the figure differ only by the respective outcome of the LDA+DMFT calculation, no other assumptions have been made. In order to improve visibility, not only the LDA+DMFT energies are shown, but also their difference from the original pure LDA energies, so that deviations from LDA are easily seen. One can clearly see two total energy parabolas, which is the expected behaviour for a first-order phase transition. From the local spectral functions which are shown at both sides of the transition, one can see that this first-order phase transition is really the

expected metal-insulator transition. The enlargement of the lattice constant that is required for the metal-insulator transition turns out to be relatively large, for the lowest temperature that is displayed, the insulating unit cell is almost 30 % larger than the equilibrium one. However, this behaviour is merely a consequence of the value of U that is only estimated. One could easily find a (larger) value of U which yields smaller deviations from the equilibrium volume. This is not done here in order to preserve comparability to previous studies. Furthermore, one could investigate if the experimental equilibrium volume corresponds to the equilibrium volume of the formalism, so that a further shift could have been introduced.

From figure 5.8, one can immediately see that the qualitative trend, i. e. the slope of the transition line, is reproduced correctly. This is believed to be one of the most striking results from the present study. One could scrutinise if the pressure at the transition point really depends linearly on temperature, which is expected experimentally, but rather unlikely in view of the pure Hubbard model studies.

It is important to note that the above study is completely devoted to total energies, although strictly speaking the free energy, which also includes entropy contributions, would be the quantity of choice to investigate phase stabilities. First of all, the additional entropy terms would not effect the occurence and the exact position of the metal-insulator transition, as it could already be seen from the local spectral function only. In this respect, the total energy is only used for better visibility. But, of course, one has to keep this in mind if observables are calculated directly from the total energy, such as bulk moduli.

Calculating a parabolic fit of the data for the LDA+DMFT total energies, one can make a Maxwell construction, i. e. find a common tangent line of the two total energy parabolas. This is shown in figure 5.9. The physical interpretation thereof is the determination of the coexistence region of the two phases. The application of increasing pressure would thus mean that a “jump” at constant pressure through the coexistence region could be observed. This typical behaviour of a

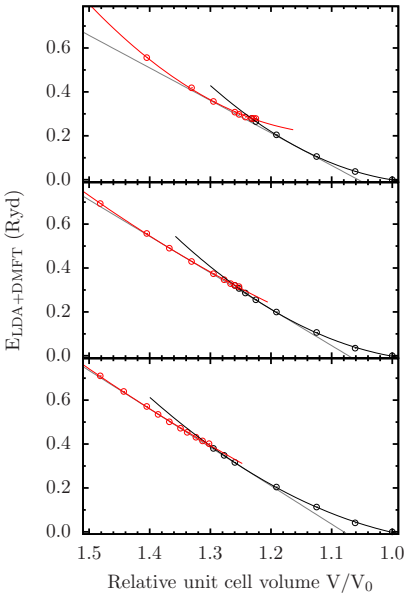

Figure 5.9: Parabolic fit of the total energies from LDA+DMFT for each phase and a Maxwell construction for the first-order metal-insulator transition as a function of the unit cell volume for $T = 387$ K, 290 K, 232 K (from top to bottom). The end of the coexistence region is further indicated by the endpoint of the respective parabola.

first-order phase transition is indeed observed in V_2O_3 as a unit cell volume jump at the metal-insulator transition [MR70].

From the intersection point of the two parabolas, one can quite accurately estimate numbers for the volume at which the metal-insulator transition takes place (if this is at all possible in view of the coexistence region). The numbers obtained for the three temperatures shown in the figure are given in table 5.1. Of course, these numbers cannot directly be related to a physical (negative) pressure, but one could at

T	$\beta = (k_\mathrm{B}T)^{-1}$	$\frac{V}{V_0}$
387 K	30 eV^{-1}	1.2319
290 K	40 eV^{-1}	1.2597
232 K	50 eV^{-1}	1.2950

Table 5.1: Unit cell volumes V at which the metal-insulator transition of V_2O_3 is estimated to take place, in units of the experimental unit cell volume V_0, as a function of temperature T or inverse temperature β.

least get a rough estimate about such a relation via the bulk modulus B:

$$\frac{\partial T}{\partial p} = -\frac{1}{B}\frac{\partial T}{\partial V} \qquad \text{with} \qquad B = \frac{\partial^2 E}{\partial V^2} \tag{5.4}$$

The most reliable number to compare with is probably the pressure difference of the highest and lowest available temperature. From the experimental phase diagram (figure 5.1), one can estimate a pressure difference of about one scale division for the whole temperature range of about 200 K for which the metal-insulator transition can be seen, which is claimed to correspond to about 4 kbar. This would correspond to a slope of about:

$$\frac{\Delta T}{\Delta p} \approx 5 \cdot 10^{-7} \frac{\mathrm{K}}{\mathrm{Pa}} \tag{5.5}$$

However, from the estimation (5.4), one would obtain a slope of:

$$\frac{\partial T}{\partial p} \approx 5.9 \cdot 10^{-8} \frac{\mathrm{K}}{\mathrm{Pa}} \tag{5.6}$$

Note that an averaged value of the bulk modulus B is used for this number, neglecting that it also changes with temperature and whether it is calculated in the metallic or insulating regime. Anyway, the calculated slope appears to differ from the experimental results by a factor of 9, almost one order of magnitude, so that the reaction to temperature changes seems to be significantly larger in the calculation

than seen experimentally. This deviating behaviour may primarily be attributed to the fact that all entropy contributions are neglected in this approach, which is probably crucial for the bulk modulus, as mentioned above. Furthermore, the experimental scaling division seems to be only a rough estimate that is directly measurable in the positive pressure region only, which is qualitatively different insofar as it corresponds to different dopants. Finally, at least to some extent, one has to keep in mind that the value of U is merely estimated and that also the overall LDA+DMFT formalism introduces certain approximations, such as the neglect of non-local correlations and phononic entropy contributions.

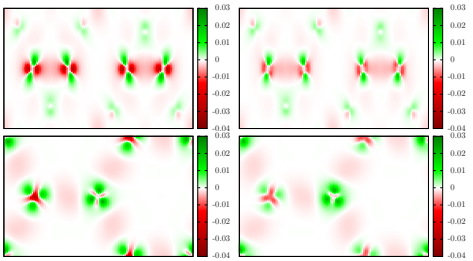

Figure 5.10: Difference $n_{\mathrm{DMFT}}(\underline{r}) - n_{\mathrm{LDA}}(\underline{r})$ of the electronic charge densities of LDA+DMFT and of pure LDA at $T = 387$ K at the equilibrium lattice constant $a = a_0$, i. e. in the metallic regime (left) and at the enlarged lattice constant with $a = 1.1 \cdot a_0$ in the insulating regime (right). The top row shows a cut in the xz-plane, the bottom row in the xy-plane.

Coming back to the basic quantity of the LDA formalism, the charge self-consistency cycle makes it possible to visualise the DMFT contributions to the electronic charge density directly. For this purpose, the difference of the self-consistent LDA+DMFT charge density and the pure LDA charge density is displayed in figure 5.10. The results are very intuitive, one can directly see the charge transfer from

the region between the atoms (interstitial region) towards the atomic (especially Vanadium) regions. This effect turns out to be particularly strong for the Vanadium dimers in the xz-plane. Furthermore, it can be seen that the occupation of the Vanadium 3d orbitals changes due to DMFT and strong electronic correlations.

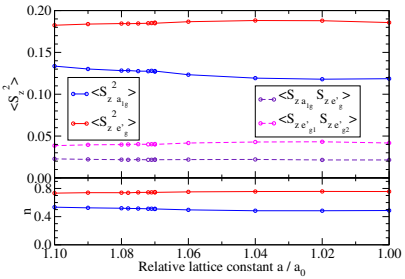

Figure 5.11: Top: Spin-spin correlation functions $\langle S_{z\,m} \cdot S_{z\,m'} \rangle$ per orbital m, m' of the t_{2g} manifold as a function of the lattice constant, i. e. negative pressure, for a fixed temperature of $T = 387$ K. Bottom: Occupation number n per t_{2g} orbital.

These occupation changes can, of course, be measured directly and are shown in figure 5.11, together with the respective spin-spin correlation functions. The most immediate observation is that both quantities are almost featureless. For the occupation numbers, one can verify a ratio of 3:1 of the a_{1g} and the two e'_g orbital occupations in the metallic regime, as it was measured in [PTT$^+$00]. The value is expectedly larger, i. e. orbital polarisation increases, compared to the pure LDA description, where a ratio of about 2.5:1 can be observed. However, instead of a stronger orbital polarisation, one can observe a slight balancing (in the order of few percent) of the occupation numbers per orbital in the insulating regime. This, at first sight, seems to contradict the data of [PTT$^+$00] (where stronger orbital polarisation is measured) and the results of previous LDA+DMFT studies in which the Mott insulating phase is modeled simply by an increase of

the interaction parameter U [HKE+01, PTB+07]. So, at this point, the modeling by negative pressure does not seem to be equivalent to a description of the doping-induced insulating phase. Contrariwise, it is possible to experimentally set up insulating doped V_2O_3 and, as it is typical for Mott insulators, find a phase transition back to a metallic phase by applying positive external pressure. This approach appears to be a very direct realisation of the modeling that is done in this study and has also been found to show almost no change in the Vanadium orbital occupation at the metal-insulator transition [RHR+10, RRS+11].

The on-site spin-spin correlation functions principally evolve according to the occupation numbers and thus are also almost featureless at the metal-insulator transition. Their values seem to hint at a $S = 1$ system, but this discussion is not supposed to be a central point of the present investigation.

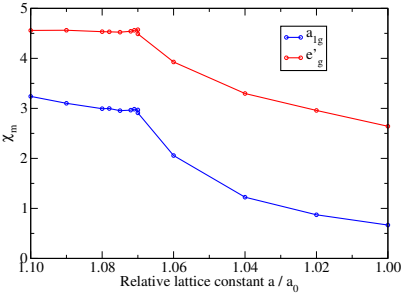

Figure 5.12: Local spin susceptibilities χ_m per orbital m of the t_{2g} manifold as a function of the lattice constant, i. e. negative pressure, for a fixed temperature of $T = 387$ K.

In order to describe the magnetic response of the material in question, it is possible to calculate local spin susceptibilities χ_m per orbital m from the QMC measured spin-spin correlation functions at imagi-

nary times τ via:

$$\begin{aligned} \chi_m &= \frac{1}{4}\int \mathrm{d}\tau \, \langle S_{z\,m}(\tau) \cdot S_{z\,m}(0) \rangle \\ &= \frac{1}{4}\int \mathrm{d}\tau \, \langle (n_{m\uparrow}(\tau) - n_{m\downarrow}(\tau)) \cdot (n_{m\uparrow}(0) - n_{m\downarrow}(0)) \rangle \end{aligned} \tag{5.7}$$

The result for a constant temperature of $T = 387$ K is shown in figure 5.12. One can clearly see the Mott metal-insulator transition, at which the increasing magnetic response turns into the expected almost constant susceptibility with increasing negative pressure.

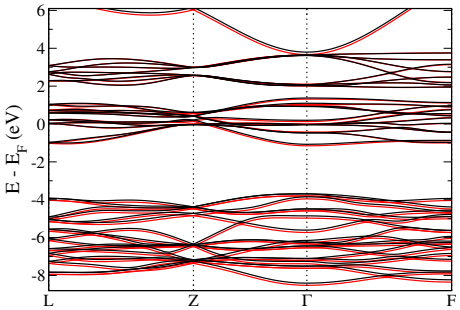

Figure 5.13: Original LDA quasi-particle band structure of V_2O_3 at its experimental lattice constant (black) and the Kohn-Sham eigenvalues $\epsilon_{\underline{k}\nu}$ that evolve in the course of the charge self-consistency cycle (red). Note that this is not a renormalised band structure as shown e. g. in the $BaVSe_3$ chapter (3.6), but only shows the influence of the CSC cycle onto the LDA part.

Another important question in the context of charge self-consistency is, of course, how far the results are actually affected by the self-consistency cycle and if they are equally reproduced in the post-processing (or single-shot) scheme. This is not the main point of interest of the current study, but also V_2O_3 seems to follow the general

trend that the effects of charge self-consistency are actually small, especially in the case of the minimal (quadratic) projection scheme that is used here. To furnish evidence for this statement, it is instructive to look at the Kohn-Sham energy eigenvalues $\epsilon_{\underline{k}\nu}$ before (i. e. in pure LDA) and after the charge self-consistency cycle (filled up to μ_{KS}). This is done in figure 5.13. It should not be confused with a renormalised band structure as it was shown in the $BaVSe_3$ chapter and defined in (3.6). Furthermore, it is the author's belief that the quantities that are shown in there should not be looked at except for technical questions, since they do not have a physical interpretation at all. Small shifts of the energy eigenvalues occur mainly in the Oxygen-related bands. These shifts are primarily not a double-counting related phenomenon, because an applied double-counting correction cancels in the quadratic projection scheme. Of course, for non-quadratic projections, the results would be different, since here the double-counting correction would play a central role and larger effects can be expected for all bands in question. Anyway, it is not impossible that small shifts of the band structure can lead to comparatively large differences when applying explicit electronic correlations, as it can also be seen in the $BaVSe_3$ chapter, where a small degeneracy between two bands leads to one filled and one empty correlated orbital.

5.3.2 Temperature scans

Of course, it is also possible to calculate phase diagram scans for other directions than pressure. Figure 5.14 shows the LDA+DMFT total energy at fixed lattice constant and structural parameters, but with varying temperature. The fixed lattice constant $a = 1.08 \cdot a_0$ is chosen such that the expected insulator-metal transition with temperature becomes visible. In this context, there is no need to substract a (constant) pure LDA value. The energy differences that occur here are seen to be significantly smaller than in the pressure scan, so that one can expect significantly more noise due to the Monte Carlo process. The observed transition temperature is in good agreement with experimen-

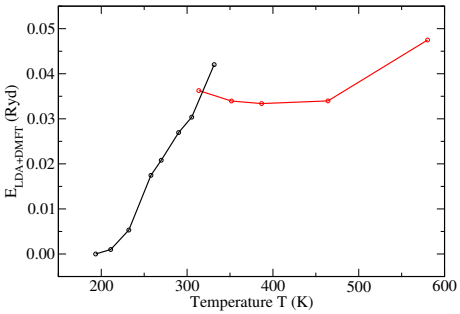

Figure 5.14: LDA+DMFT total energy at finite negative pressure, i. e. at a lattice constant of $a = 1.08 \cdot a_0$, as a function of temperature. The values are normalised to the lowest temperature that is visible.

tal data from the above phase diagram, although a direct comparison of numbers is again not possible. Of course, one would typically expect a larger transition temperature from DMFT than from experiment due to the mean-field character of DMFT. Interestingly, the slope of the energy as a function of temperature seems to be larger in the metallic than in the insulating regime, with an almost flat curve in the insulating phase up to the critical end-point.

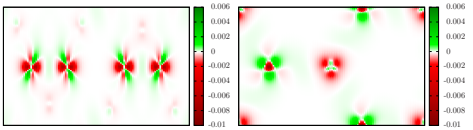

Figure 5.15: Difference $n_{\mathrm{DMFT}}^{\mathrm{metallic}}(\underline{r}) - n_{\mathrm{DMFT}}^{\mathrm{insulating}}(\underline{r})$ of the electronic charge densities of LDA+DMFT at two different temperatures, namely in the metallic regime (T=232 K) and in the insulating regime (T=387 K) for a lattice constant $a = 1.08 \cdot a_0$. The left plot is a cut within the xz-plane, the right plot within the xy-plane.

Evaluated at different temperatures, it is directly possible to com-

pare charge densitites from LDA+DMFT in the metallic and the insulating regime, which is done in figure 5.15 for T=232 K (metallic) and T=387 K (insulating). The effects are, as expected, very small, but once again the typical behaviour of a Mott insulator can be observed, especially the localisation of charge near the (Vanadium) nuclei. Also here, a change in the orbital occupations is evident.

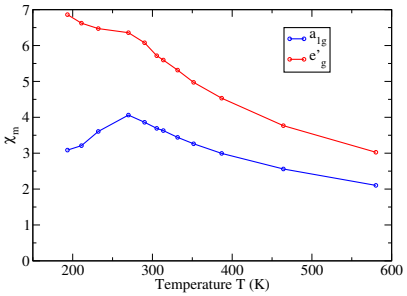

Figure 5.16: Local spin susceptibilities χ_m per orbital m of the t_{2g} manifold as a function of temperature at fixed lattice constant $a = 1.08 \cdot a_0$.

It is furthermore interesting to calculate the magnetic response in terms of the orbital-resolved local spin susceptibilites χ_m using (5.7) as a function of temperature. The high-temperature part is overall in good agreement with the data shown in [PTB+07], with the limitation that the a_{1g} orbital of the basis used there is significantly stronger depleted and therefore the response of the a_{1g} seen there is much weaker. Interestingly, the metal-insulator transition is less obvious in this scan than in the magnetic response with pressure. Deviations from the ideal Curie-Weiss behaviour ($\chi \propto (T - T_C)^{-1}$) of a paramagnetic metal are observed below $T \approx 280$ K. The strong orbital-dependent response might already be a hint onto orbital selective scenarios in the low-temperature antiferromagnetically ordered phase, which is, of course, known to be accompanied by a structural transition.

5.3.3 Relaxing the ratio $\frac{c}{a}$

Up to now, all calculations have been done with fixed structural parameters; only the total unit cell volume, or equivalently, the lattice constant at fixed ratio $\frac{c}{a}$ of the crystallographic parameters, has been modified. This is only partially justified, since a small but discontinuous shift of the ratio $\frac{c}{a}$ has been observed experimentally at the metal-insulator transition [MRR69, RHR+10, RRS+11]. In order to find out whether this discontinuous shift can be described within the model for V_2O_3 used in this study, the total energies of the LDA+DMFT formalism can be used. For this purpose, calculations are made for several selected values of $\frac{c}{a}$ at fixed unit cell volume (note that this is in this case not equivalent to a fixed lattice constant a). The resulting total energy values are interpolated by a simple parabolic function, so that a relaxed minimum energy value is found.

First of all, the same relaxation can of course also be done with pure LDA total energies. The resulting values for $\frac{c}{a}$ turn out to be slightly larger than the experimental values, in the range of 2.9. Of course, no features can be observed at the metal-insulator transition.

Figure 5.17 shows the relaxed values for $\frac{c}{a}$ from LDA+DMFT. One can see that the correction of the values due to LDA+DMFT gives qualitatively the right tendency, the values become slightly smaller and range from about 2.7 to 2.8, in reasonable agreement with the experimental values of 2.8281 (in the metallic phase) and 2.7832 (in the insulating phase) [Der70]. For several reasons, the values are relatively noisy, namely because of the quantum Monte Carlo noise (the actual energy differences are comparably small, in the range of 10^{-3} eV) and because the minimum of the energy parabola is relatively flat, so that already small fluctuations in energy and small variations of the fitting procedure can result in comparably large deviations of the relaxed $\frac{c}{a}$ value. Due to the latter, it is difficult to estimate the appropriate size of error bars in a reliable way. The ratio $\frac{c}{a}$ apparently turns out to be minimal right at the intersection point of the total energy parabolas of the two phases. Having in mind that this point is not

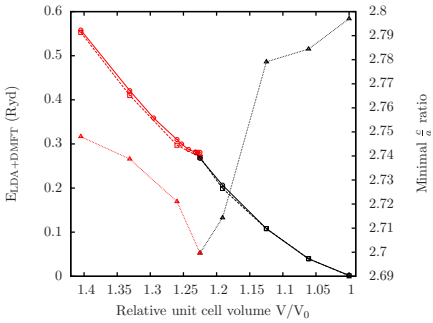

Figure 5.17: Solid lines: LDA+DMFT total enery as a function of unit cell volume for the $\frac{c}{a}$ ratio fixed at its metallic value. Dashed lines: same for the relaxed $\frac{c}{a}$ value. Dotted lines: Relaxed $\frac{c}{a}$ values as a function of unit cell volume. Black lines mark the metallic solution, red lines the insulating one. All values are calculated for $T = 387$ K.

directly accessible experimentally because of the phase coexistence region, one can guess a discontinuous behaviour at the end-points of the coexistence region.

As mentioned, the relaxed values for $\frac{c}{a}$ are overall smaller than the experimental ones. This, in turn, means that if one simply compares the energy values of the two $\frac{c}{a}$ ratios found experimentally, one would find that the experimental insulating $\frac{c}{a}$ ratio is lower in energy than the experimental metallic $\frac{c}{a}$ ratio for a large parameter range. (Note that a pure LDA comparison would give the opposite result.) So this approach is, of course, too simplified and therefore does not yield the correct results.

Another comparison that can be seen in figure 5.17 deals with the energy values at fixed (metallic) ratio $\frac{c}{a}$ that have been used throughout this chapter and the energies at relaxed $\frac{c}{a}$ ratio. One can see that both curves are very similar, all qualitative features, especially the exact position of the metal-insulator transition, remain unaltered. This observation serves as a motivation that all previously shown data

at fixed ratio $\frac{c}{a}$ remains valid despite the neglected small structural change. The relaxed energy values are only minimally smaller, reasonably, the difference seems a little larger in the insulating regime than in the metallic regime (since the metallic $\frac{c}{a}$ ratio has been used for the fixed $\frac{c}{a}$ calculations).

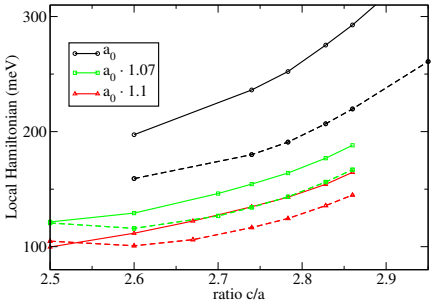

Figure 5.18: Local Hamilton operator to enter the DMFT calculations as defined by (5.8) for a_{1g} (solid) and e'_g (dashed) orbitals with varying $\frac{c}{a}$ ratio at constant unit cell volume. All values are calculated for $T = 387$ K.

One of the main effects that the variation of $\frac{c}{a}$ can be expected to have is related to the trigonal crystal field splitting between the a_{1g} and e'_g orbitals of V_2O_3. In order to observe such features, one can investigate the local Hamilton operator that enters the DMFT formalism by means of the projection formalism:

$$\underline{\underline{H}}^{\mathrm{loc}} \equiv \sum_{\underline{k}} \underline{\underline{\bar{P}}}(\underline{k}) \cdot \underline{\underline{\epsilon}}^{\mathrm{KS}}_{\underline{k}} \cdot \underline{\underline{\bar{P}}}^{\dagger}(\underline{k}) \tag{5.8}$$

It is shown in figure 5.18. Note that it is not a pure LDA quantity, since the DMFT charge density does enter the LDA part through the charge self-consistency scheme. In principle, one could add the real part of the self-energy at $\omega = 0$ to obtain an effective crystal field splitting including electronic correlations, but this has shown not to

reveal large differences to the picture. One can clearly observe an increase of the trigonal crystal field splitting with increasing ratio $\frac{c}{a}$, which is expected since the increase of $\frac{c}{a}$ results in an increase of the distortion of the VO_6 octahedra from which the trigonal crystal field splitting originates.

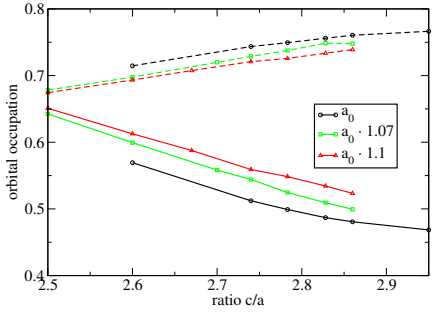

Figure 5.19: Occupation numbers for the a_{1g} (solid) and e'_g (dashed) orbitals with varying $\frac{c}{a}$ ratio at constant unit cell volume. All values are calculated for $T = 387$ K.

As a direct consequence of the increasing crystal field splitting, the occupation numbers provided in figure 5.19 show increasing orbital polarisation with increasing ratio $\frac{c}{a}$. It has been argued that a possible increased orbital polarisation in the insulating phase is, at least partially, the consequence of the small jump in the ratio $\frac{c}{a}$ at the metal-insulator transition. This does not seem to be likely in this picture, the jump in the ratio $\frac{c}{a}$ would rather lead to a further orbital balancing. But note that this effect would be very small.

This short study of the relaxation of $\frac{c}{a}$ is, of course, mainly intended as a brief outlook. It could be continued in several different directions, for instance the temperature dependence of the structural change or the small effects on the metal-insulator transition that this small structural distortion might have could be investigated. However, due to the large numerical demands that these calculations have at the

present stage of development, these questions are left for future studies and the present work is left as a proof of principle that it is worth investigating structural distortions with LDA+DMFT total energies.

5.4 Conclusive discussion

The present charge self-consistent LDA+DMFT investigation of the strongly correlated V_2O_3 compound provides a quite detailed overview about how accurately its physical properties can be captured by the LDA+DMFT approach and to what extent the simple mapping of doping onto pressure holds. To begin with, the principal description of the metal-insulator transition with pressure is correct concerning its existence and the qualitative slope of the transition line with temperature. One can argue that quantitatively, the value that can be estimate for the slope appears to be too large, but, as mentioned, this can be related to the neglection of entropy effects, the choice of the interaction parameters U and J and of course to an uncertainty about the underlying experimental pressure estimate. Similarly, the overall enlargement of the unit cell that is required to drive the metal-insulator transition appears to be large, since values of up to 30 % can be needed here. Of course, this is, to a large extent, the consequence of the choice of the interaction parameters U and J, which are not determined from ab initio in this study, but are rather estimated in view of previously published studies [HKE$^+$01].

One could argue that the parameters are relatively large, as later studies, such as [PTB$^+$07], have used smaller values around 4.2 eV or 4.4 eV to drive the Mott transition by U only. Here, it has to be kept in mind that, firstly, the applied basis is minimal and thus not maximally localised. Secondly, this appears to be a more or less general feature of the charge self-consistency scheme. As screening effects enter the self-consistency cycle explicitly, one can expect that larger interaction parameters are required to see the same effect, or, equivalently, the charge self-consistency results in slightly less prominent electronic

correlation features. To use a very simplified argument, this is expected since the charge self-consistent solution has to lie somewhere between the pure LDA solution and the post-processing one. Similar arguments apply for observables like occupation numbers or the crystal field splitting; one can expect that, for instance, the occupation polarisation is slightly smaller in the charge self-consistent description than in post-processing DMFT.

Some debate might arise about the change in occupation numbers at the metal-insulator transition, especially that one does not observe a stronger polarisation in the insulating phase in this study. Previous studies that simply assumed a larger value of U in that phase naturally find a stronger orbital polarisation therein, which is not done here and, as mentioned, seems to be in line with recent experiments. However, such an effect has been confirmed in doped insulating V_2O_3 [PTT$^+$00] and thus it should be possible to reproduce the effect in simulations. The first idea might be simply to look for more suitable interaction parameters that lead to different effects with respect to occupation numbers; especially the parameter J can, of course, influence occupation numbers very directly. However, this has been tried for a small set of parameters, and no combination that is qualitatively significantly different has been found. Of course, this does not mean that the existence of a suitable set is impossible. Anyway, since also the ratio $\frac{c}{a}$ of the lattice parameters has been shown not to produce the "correct" orbital polarisation, one has to admit that the pressure picture of doping in V_2O_3 has reached its limits. The full ab-initio approach of doping of V_2O_3 in terms of supercells for the LDA calculations, seems to be in place here. This is in principle feasible with the current implementations, but is postponed to later studies due to the enormous computational demand of such calculations.

In order to have a complete description of the entire phase diagram of V_2O_3, which should be the final goal of the LDA+DMFT calculations, it would be necessary to do calculations for the antiferromagnetic insulating low-temperature phase. This phase is probably not the direct consequence of strong electronic correlations, however

the present LDA+DMFT methodology should be capable of giving hints about that phase transition as well, at least due to its intrinsic temperature dependence. Furthermore, the Mott metal-insulator transition has a critical end-point above which the first order transition turns into a crossover, which also deserves some LDA+DMFT investigation. These two projects form a short outlook on possible further calculations about the interesting and multifaceted material V_2O_3.

In the end, the present study has shown that the LDA+DMFT method with charge self-consistency and its energetics are a suitable and well-motivated method to describe strong electronic correlations that would otherwise not be accessible by calculational techniques. Furthermore, the possibility to calculate total energies allows for the calculation of even subtle effects, as demonstrated for the ratio $\frac{c}{a}$.

Six

Concluding Remarks

The present thesis aims to describe and judge the current state of the art of the charge self-consistency for the LDA+DMFT method to describe strong electronic correlations explicitly in real materials. It shows applications of the "classical" method (like the compound Barium Vanadium triselenide), but puts emphasis on the new developments and implementations in the context of charge self-consistency, focusing on the MBPP methodology, but also describing an implementation in the PAW framework. The successful application onto Vanadium sesquioxide aims to prove the success of the methodology and its evaluation of total energies.

Of course, this work is not the end of the whole story of strong electronic correlations in materials in general and LDA+DMFT in special. On the implementation side, several topics closely related to the topics presented here are worth investigating, such as the calculation of free energies that has shown to be, at least, worth investigating in the V_2O_3 part, or a more efficient and rather automated way to obtain a basis for the correlated subspace, or a true ab-initio scheme to obtain interaction parameters U or J in a reliable way. However, it appears reasonable to say that the LDA+DMFT methodology seems to "converge" to a scheme that is useful and reliable for a large class of materials. So a lot of work is left on the applicative side, in order to fully exploit this "large class" in near future. The present the-

sis is quite limited in this direction, it only presents the work that has lead to peer-reviewed publications, while almost completely ignoring the results for other materials that have been found alongside. Just to name a few, the investigation of the spectral properties of the (nameless) heavy-fermion compound LiV_2O_4 and its Zink-doped versions, the phase stability of the charge-ordered compound $LuNiO_3$, the structural transitions and lattice constant enlargements in the pure transition metals Iron and Manganese and also some features of the heavily discussed Sodium-doped cobaltates are not even mentioned in this thesis, although still providing a large playground for further investigations. Also a more detailed comparison to the LDA+RISB methodology is definitely worth looking at in view of some of the above-mentioned materials.

To conclude, it can be said that, with the charge self-consistent LDA+DMFT methodology, a successful route has been started that deserves to be followed further.

One

Example of a working TRIQS input file

The following input file is taken from the Vanadium Sesquioxide work documented in chapter 5. To begin with, a working python input file for TRIQS [FP] could look like this:

```
####################################
#
#  Variables
#
####################################

Beta = 50.00
Reasonable_U = 5.00
Reasonable_J = 0.93
Density_Required = 8.0
LDA_Chemical_potential  = 8.0
Chemical_potential_init = 3.0
Charge_Self_Consistency = True

####################################
#
#  Solver
#
####################################

from Solver_RI import Solver_2_or_3_bands_Hubbard_RI
import pytriqs.Base.Utility.MPI as MPI
```

```
S = Solver_2_or_3_bands_Hubbard_RI(Beta = Beta, Norb = 3,
                                   U_interact = Reasonable_U,
                                   J_Hund = Reasonable_J,
                                   J_C = Reasonable_J)
S.N_Cycles  = 10000000/MPI.size
S.N_Frequencies_Accumulated = 70
S.Fitting_Frequency_Start = 35
S.N_Time_Slices_Delta = 10000
S.N_Time_Slices_Gtau = 10000
S.Length_Cycle       = 500
S.N_Legendre_Coeffs = 52
S.Record_Statistics_Configurations = False
S.Nmax_Matrix = 500
S.Time_Accumulation = True
S.Legendre_Accumulation = False

####################################
#
#  SumK
#
####################################

from pytriqs.CSC.SumK_From_LDA_Projections_mbpp import *
SK = SumK_From_LDA_Projections_mbpp (Substract_Fermi_energy = False)

from pytriqs.CSC.DFT_step import DFT_step
dftstep = DFT_step(Code="mbpp")

####################################
#
#  N-Matrix
#
####################################

import pytriqs.CSC.Nmatrix

Nm = pytriqs.CSC.Nmatrix.DeltaN(N_kpts=SK.Hopping.shape[0],
                                Bloch_Indices=SK.GFBlocBlochIndices,
                                Hopping=SK.Hopping,
```

```
                                    Projection=SK.Projection, Copy=False)

####################################
#
#  Green's functions
#
####################################

from pytriqs.Base.GF_Local import *
G = GF(Name_Block_Generator = [
        (s, GFBloc_ImFreq(Indices=SK.GFBlocIndices,
                          Mesh = S.G.mesh))
        for s in ['up','down'] ], Copy = False)
Gbl = GF(Name_Block_Generator = [
        (s, GFBloc_ImFreq(Indices=SK.GFBlocBlochIndices,
                          Mesh = S.G.mesh))
        for s in ['up','down'] ], Copy = False)
Gbltau = GF(Name_Block_Generator = [
        (s, GFBloc_ImTime(Indices=SK.GFBlocBlochIndices,
                          Beta=Beta, NTimeSlices=500))
        for s in ['up','down'] ], Copy = False)
Sigma = G.copy()
Sigma_zero = G.copy()
Sigma_zero.zero()
DC = G.copy()
Gu_imp = S.G.copy()
DC_imp = S.G.copy()

####################################
#
#  Embedding/Extraction
#
####################################

from pytriqs.Base.DMFT.Loop_Generic import *
import pytriqs.Base.Utility.Dichotomy as Dichotomy

class myloop (DMFT_Loop_Generic) :

   def Self_Consistency(self):
```

```
# Computation of the Sum over k to get LDA occupation numbers
F0 = lambda mu: SK(mu=mu, Sigma=Sigma_zero,
                   Project=False).total_density()
global LDA_Chemical_potential, DC

if ((self.Iteration_Number <= 1) or Charge_Self_Consistency):
   if Density_Required and (self.Iteration_Number > 0):
      LDA_Chemical_potential = \
          Dichotomy.Dichotomy(Function = F0,
                              xinit = LDA_Chemical_potential,
                              yvalue = Density_Required,
                              Precision_on_y = 0.0001,
                              Delta_x=0.5, MaxNbreLoop=10000,
                              xname="LDA_Chemical_Potential",
                              yname= "Total Density",
                              verbosity = 3)[0]
   else:
      MPI.report("No adjustment of LDA chemical potential.")
      MPI.report("Total density = %.3f" \
                     %F0(LDA_Chemical_potential))

   MPI.report("Total density of LDA GF = %.3f" \
                  %SK(mu = LDA_Chemical_potential,
                      Sigma = Sigma_zero, DoubleCounting = None,
                      Res = G, Project = True).total_density())

   # Calculation of Double Counting correction

   for s in ['up', 'down']:
       for i in range(3):
           for j in range(3):
               Gu_imp[s][i, j] = G[s][i, j]

   SK.FLL(U_interact = Reasonable_U, J_Hund = Reasonable_J,
          LDA_Occupations = Gu_imp.density(), Res = DC_imp)

   for k in range(4):   # Number of impurities
      for s in ['up', 'down']:
         for i in range(3):
            for j in range(3):
```

```
                DC[s][3*k+i, 3*k+j] = DC_imp[s][i,j]

#Embedding(self):
for k in [ 0, 3, 6, 9 ]:
   for i in range(3):
      for j in range(3):
         for s in [ 'up', 'down' ]:
            Sigma[s][i+k,j+k] = 0.5 * (S.Sigma['up'][i,j] + \
                                       S.Sigma['down'][i,j])

if Charge_Self_Consistency:
   # Compute the SumK for the determination of the NMatrix
   Fbl = lambda mu : SK(mu = mu, Sigma = Sigma,
                        DoubleCounting = DC, Res = Gbl,
                        Project = False).total_density()

   if Density_Required and (self.Iteration_Number > 0):
      self.Chemical_potential = \
         Dichotomy.Dichotomy(Function = Fbl,
                             xinit = self.Chemical_potential,
                             yvalue = Density_Required,
                             Precision_on_y = 0.0001,
                             Delta_x=0.5, MaxNbreLoop = 10000,
                             xname="Nmatrix_Chemical_Potential",
                             yname= "Total Density",
                             verbosity = 3)[0]
   else:
       MPI.report("No adjustment of Nmatrix chemical potential")
       MPI.report("Total density = %.3f" \
                       %Fbl(self.Chemical_potential))

   Nm(mu = self.Chemical_potential, SelectedBlock = 'up',
      mu_KS =  LDA_Chemical_potential, Sigma = Sigma,
      DoubleCounting = DC, Hopping = SK.Hopping,
      Projection = SK.Projection, Normalize = False)
   Nm.save("NMATRIX", False)
   MPI.report("Norm of Nmatrix: %f"%(Nm.norm()))

   #DFT:
   dftstep(G = G, Sigma = Sigma - DC)
```

```
   SK.reread()

# Compute the SumK, possibly fixing mu by dichotomy
Fbl = lambda mu : SK(mu = mu, Sigma = Sigma,
                     DoubleCounting = DC, Res = Gbl,
                     Project = False).total_density()

if Density_Required and (self.Iteration_Number > 0):
   self.Chemical_potential = \
       Dichotomy.Dichotomy(Function = Fbl,
                           xinit = self.Chemical_potential,
                           yvalue = Density_Required,
                           Precision_on_y = 0.0001,
                           Delta_x=0.5, MaxNbreLoop=10000,
                           xname="Chemical_Potential",
                           yname= "Total Density",
                           verbosity = 3)[0]
else:
   MPI.report("No adjustment of chemical potential")
   MPI.report("Total density = %.3f" \
                  %Fbl(self.Chemical_potential))

MPI.report("Total density of projected (impurity) GF = %.3f" \
              %SK(mu = self.Chemical_potential,
                  Sigma = Sigma, DoubleCounting = DC,
                  Res = G, Project = True).total_density())

MPI.report('Occupation matrix')
MPI.report(G['up'].density().real )
MPI.report(G['down'].density().real)

for ind, Gbli in Gbl:
   Gbltau[ind].setFromInverseFourierOf(Gbli)

dftstep.calculate_two_particle_energy(G = G, Sigma = Sigma - DC)

#Extraction(self):
for i in range(3):
   for j in range(3):
      for s in [ 'up', 'down' ]:
```

```
            S.G[s][i,j]     = 0.125 * (G['up'][i,j] +
                                       G['up'][3+i,3+j] +
                                       G['up'][6+i,6+j] +
                                       G['up'][9+i,9+j] +
                                       G['down'][i,j] +
                                       G['down'][3+i,3+j] +
                                       G['down'][6+i,6+j] +
                                       G['down'][9+i,9+j])
            S.Sigma[s][i,j] = 0.125 * (Sigma['up'][i,j] +
                                       Sigma['up'][3+i,3+j] +
                                       Sigma['up'][6+i,6+j] +
                                       Sigma['up'][9+i,9+j] +
                                       Sigma['down'][i,j] +
                                       Sigma['down'][3+i,3+j] +
                                       Sigma['down'][6+i,6+j] +
                                       Sigma['down'][9+i,9+j])

     S.G0 = inverse(S.Sigma + inverse(S.G))   # Finally get S.G0

     if MPI.IS_MASTER_NODE():
        G.save("GC", Accumulate = False)
        Sigma.save("Sigma", Accumulate = False)
#       S.G0.save("G0S", Accumulate = False)
        Gbltau.save("Gbl_t", Accumulate = False)

   def PostSolver(self):
     if MPI.IS_MASTER_NODE():
#       S.G_tau.save("GCS_t", Accumulate = False)
#       S.Delta_tau.save("Delta_t", Accumulate = False)
        S.Sigma.save('Sigma_next', Accumulate = False)
#       S.G_Legendre.save("GS_l", Accumulate = True)

####################################
#
#  Load previous result
#
####################################

S.Sigma.load('Sigma_next', NoException = False)
for i in range(3):
```

```
   for j in range(3):
      S.Sigma['up'][i,j]   = 0.5 * (S.Sigma['up'][i,j] +
                                    S.Sigma['down'][i,j])
      S.Sigma['down'][i,j] = 1.0 *  S.Sigma['up'][i,j]

####################################
#
#  Start calculation
#
####################################

myloop(Solver_List = S,
       Chemical_potential = Chemical_potential_init).run(
    N_Loops = 3, Mixing_Coefficient = 0.5)

if MPI.IS_MASTER_NODE():
   S.Sigma.save('Sigma_next', Accumulate = False)
```

The overall structure thereof is very similar to an "ordinary" input file for TRIQS. So only the main differences shall be named shortly in the following:

First of all, the interfacing in the projection onto localised orbitals formalism is done in the `SumK_From_LDA_Projections_mbpp` object, which reads in eigenvalues (from a file `BAND.dat`) and projection matrices (from `PMAT.PROJ`). The version without the ending `_mbpp` also exists for the PAW interface. Both also provide the usual double-counting correction schemes.

The main quantity for the charge self-consistency is the matrix $\Delta\underline{\underline{N}}^{(\underline{k})}$. It is calculated via the `DeltaN` objects before each DFT step. Before its calculation and after the DFT step, an adjustment of the chemical potential is required, $\Delta\underline{\underline{N}}^{(\underline{k})}$ also requires the correct adjustment of μ^{KS}.

Finally, the connection to the MBPP code [MELFed] is done via a call thereof in the `DFT_step` object. MBPP requires a separate input file `INP`, similar to the following for the equilibrium lattice constant V_2O_3:

```
V2O3   Corundum   R-3c
```

```
! Reference: P. D. Dernier, J. Phys. Chem. Solids 31, 2569 (1970)
#define VERSION1.0
!#define MB_TIMING
#define MB_TINY_TOL
#define PRT_SYM_R
#define PRT_CRYSTDAT
!#define PRT_SYM_G
!#define DIAG_NV
#define PRT_ATOM_SHELLS
!#define SYS_CHECK
!#define READ_MIX_MAT
#define READ_EV
#define PLT_FBD_LM
!#define NO_TIMEREVERS
!#define LDA_U
#define LDA_DMFT_SC
10
   ntype=2    natomax=6   struc=coru
    natom=4   name=V
   0.34630      0.34630      0.34630
  -0.34630     -0.34630     -0.34630
   0.84630      0.84630      0.84630
  -0.84630     -0.84630     -0.84630
    natom=6   name=O
  -0.06164      0.56164      0.25
   0.06164     -0.56164     -0.25
   0.56164      0.25        -0.06164
  -0.56164     -0.25         0.06164
   0.25        -0.06164      0.56164
  -0.25         0.06164     -0.56164
  alat=1.0
      -2.70112848     4.67849176     8.82061500
      -2.70112848    -4.67849176     8.82061500
       5.40225696     0.00000000     8.82061500
 symop=gen
20
  emax=20 emax_init=12  gmax=30.0  corr=pw  dcu=amf
   nloc=5
   itype=1   l=0  fctyp=11 gamma=1.0 rcut=1.6
   itype=1   l=1  fctyp=15 rcut=1.6
```

```
   itype=1   l=2  fctyp=11 gamma=1.00 rcut=2.0
   itype=2   l=0  fctyp=11 gamma=1.0 rcut=1.5
   itype=2   l=1  fctyp=15 rcut=1.5
  ngauss=300
   atom=V  s=lo 3100 0.01  p=nl 310 0.02 d=nl 310 0.02 znuc=23.0 &
   u=0.0 j=0.95 fratio=0.625 rcut=2.0 nl=300 0.02 ngauss=150
   atom=O  s=lo 3100 0.01  p=nl 310 0.02 d=nl 310 0.02 znuc=8.0
30
   kpmeth=mp
   nband=80  ifmax=50   nkxyz=13 13 13  shift=0.0 0.0 0.0
31
  passbands=40 actbands=12 alpha=0.1
40
  niter=1   scr=dm   ifmet=yes intmeth=tetra
  broy=yes   ekmix=32.0 ! spec=dp nitdp=10 alph=0.2
82
   nproj=4 norb=3 passbands=40 actbands=12 lgreen=yes
   kmesh=13 13 13
   nrtyp=1 nrat=1
   0 0 0 0   1.0       0.0       0.0       0.0       0.0
   0 0 0 0   0.0       0.670417  0.0       0.0       0.741282
   0 0 0 0   0.0       0.0       0.670417  0.741282  0.0
   nrtyp=1 nrat=2
   0 0 0 0   1.0       0.0       0.0       0.0       0.0
   0 0 0 0   0.0       0.670417  0.0       0.0       0.741282
   0 0 0 0   0.0       0.0       0.670417  0.741282  0.0
   nrtyp=1 nrat=3
   0 0 0 0   1.0       0.0       0.0       0.0       0.0
   0 0 0 0   0.0       0.670417  0.0       0.0      -0.741282
   0 0 0 0   0.0       0.0      -0.670417  0.741282  0.0
   nrtyp=1 nrat=4
   0 0 0 0   1.0       0.0       0.0       0.0       0.0
   0 0 0 0   0.0       0.670417  0.0       0.0      -0.741282
   0 0 0 0   0.0       0.0      -0.670417  0.741282  0.0
00
```

The main differences to a standard MBPP input file are the new `#define LDA_DMFT_SC` tag set in the beginning and the new block `31` to set a suitable window for the subspace $\mathcal{W}$ and a linear mixing factor. Since only a single Hamilton operator diagonalisation is done in the

DFT step, the number of iterations is set to 1 and a DMFT-related screening potential (`dm`) is used. The eigenvectors of the previous step are required to be read for the construction of the sreening potential.

A short note about the compilation process: The CSC module can be compiled like an ordinary TRIQS module. It requires a static library version of the MBPP code (currently `libcmb24.a`). The path thereof, together with the (optional) `wannier90` library, currently has to be given explicitly in the configuration file `FindMBPP.cmake`:

```
link_libraries(/path/to/libcmb24.a
/path/to/libwannier.a
-limf -lifport -lifcore -lsvml -lmpi_f77)
```

List of Tables

List of Figures

List of Publications

Refereed publications discussed in this thesis

1. D. Grieger, L. Boehnke, and F. Lechermann.
   Electronic correlations in vanadium chalcogenides: $BaVSe_3$ versus $BaVS_3$.
   J. Phys.: Condens. Matter, 22:275601, 2010.

2. D. Grieger, C. Piefke, O. E. Peil, and F. Lechermann.
   Approaching finite-temperature phase diagrams of strongly correlated materials: a case study for V_2O_3.
   Phys. Rev. B, 86:155121, 2012 (Editors' Suggestion).

Unrelated work

1. S. Schuwalow, D. Grieger and F. Lechermann.
   Realistic modeling of the electronic structure and the effect of correlations for Sn/Si(111) and Sn/Ge(111) surfaces.
   Phys. Rev. B, 82:035116, 2010.

Bibliography

[AJT08] B. Amadon, F. Jollet, and M. Torrent. γ and β cerium: LDA + U calculations of ground-state parameters. *Phys. Rev. B*, 77:155104, 2008.

[ALG+08] B. Amadon, F. Lechermann, A. Georges, F. Jollet, T. O. Wehling, and A. I. Lichtenstein. Plane-wave based electronic structure calculations for correlated materials using dynamical mean-field theory and projected local orbitals. *Phys. Rev. B*, 77:205112, 2008.

[AM76] N. W. Ashcroft and N. D. Mermin. *Solid State Physics*. Holt, Rinehart and Winston, 1976.

[Ama12] B. Amadon. A self-consistent DFT + DMFT scheme in the projector augmented wave method: applications to cerium, Ce_2O_3 and Pu_2O_3 with the Hubbard I solver and comparison to DFT + U. *J. Phys.: Condens. Matter*, 24:075604, 2012.

[Ant59] E. Antončík. Approximate formulation of the orthogonalized plane-wave method. *J. Phys. Chem. Solids*, 10:314, 1959.

[APG11] M. Aichhorn, L. Pourovskii, and A. Georges. Importance of electronic correlations for structural and magnetic properties of the iron pnictide superconductor LaFeAsO. *Phys. Rev. B*, 84:054529, 2011.

[ASacH+08] A. Akrap, V. Stevanović, M. Herak, M. Miljak, N. Barišić, H. Berger, and L. Forró. Transport and magnetic properties of $BaVSe_3$. *Phys. Rev. B*, 78:235111, 2008.

[ASK+93] V. I. Anisimov, I. V. Solovyev, M. A. Korotin, M. T. Czyżyk, and G. A. Sawatzky. Density-functional theory and NiO photoemission spectra. *Phys. Rev. B*, 48:16929, 1993.

[AZA91] V. I. Anisimov, J. Zaanen, and O. K. Andersen. Band theory and Mott insulators: Hubbard U instead of Stoner *I. Phys. Rev. B*, 44:943, 1991.

[BABH00] O. Bengone, M. Alouani, P. Blöchl, and J. Hugel. Implementation of the projector augmented-wave LDA+U method: Application to the electronic structure of NiO. *Phys. Rev. B*, 62:16392, 2000.

[Bay62] G. Baym. Self-consistent approximations in many-body systems. *Phys. Rev.*, 127:1391, 1962.

[BBA+97] W. Bao, C. Broholm, G. Aeppli, P. Dai, J. M. Honig, and P. Metcalf. Dramatic switching of magnetic exchange in a classic transition metal oxide: Evidence for orbital ordering. *Phys. Rev. Lett.*, 78:507, 1997.

[BBC+93] W. Bao, C. Broholm, S. A. Carter, T. F. Rosenbaum, G. Aeppli, S. F. Trevino, P. Metcalf, J. M. Honig, and J. Spalek. Incommensurate spin density wave in metallic $V_{2-y}O_3$. *Phys. Rev. Lett.*, 71:766, 1993.

[Bec93] A. D. Becke. Density-functional thermochemistry. III. The role of exact exchange. *J. Chem. Phys.*, 98:5648, 1993.

[BFS03] P. E. Blöchl, C. J. Först, and J. Schimpl. Projector augmented wave method: *ab initio* molecular dynamics with full wave functions. *Bull. Mater. Sci.*, 26:33, 2003.

[BJA94] P. E. Blöchl, O. Jepsen, and O. K. Andersen. Improved tetrahedron method for Brillouin-zone integrations. *Phys. Rev. B*, 49:16223, 1994.

[BK61] G. Baym and L. P. Kadanoff. Conservation laws and correlation functions. *Phys. Rev.*, 124:287, 1961.

[Blö94] P. E. Blöchl. Projector augmented-wave method. *Phys. Rev. B*, 50:17953, 1994.

[BO27] M. Born and R. Oppenheimer. Zur Quantentheorie der Molekeln. *Annalen der Physik*, 389:457, 1927.

[Boy66] S. F. Boys. Localized orbitals and localized adjustment functions. In P.-O. Löwdin, editor, *Quantum Theory of Atoms, Molecules and the Solid State*, pages 253–262. Academic Press Inc., 1966.

[BPLG05] S. Biermann, A. Poteryaev, A. I. Lichtenstein, and A. Georges. Dynamical singlets and correlation-assisted Peierls transition in VO_2. *Phys. Rev. Lett.*, 94:026404, 2005.

[Bra77] B. H. Brandow. Electronic structure of Mott insulators. *Adv. Phys.*, 26:651, 1977.

[Bro65] C. G. Broyden. A class of methods for solving nonlinear simultaneous equations. *Math. Comp.*, 19:577, 1965.

[Bry90] R. Bryan. Maximum entropy analysis of oversampled data problems. *Eur. Biophys. J.*, 18:165, 1990.

[CA80] D. M. Ceperley and B. J. Alder. Ground state of the electron gas by a stochastic method. *Phys. Rev. Lett.*, 45:566, 1980.

[CdzS94] M. T. Czyżyk and G. A. Sawatzky. Local-density functional and on-site correlations: The electronic structure of La_2CuO_4 and $LaCuO_3$. *Phys. Rev. B*, 49:14211, 1994.

[CNR78] C. Castellani, C. R. Natoli, and J. Ranninger. Magnetic structure of V_2O_3 in the insulating phase. *Phys. Rev. B*, 18:4945, 1978.

[Der70] P. D. Dernier. The crystal structure of V_2O_3 and $(V_{0.962}Cr_{0.038})_2O_3$ near the metal-insulator transition. *J. Phys. Chem. Solids*, 31:2569, 1970.

[DFM+12] X. Deng, M. Ferrero, J. Mravlje, M. Aichhorn, and A. Georges. Hallmark of strong electronic correlations in $LaNiO_3$: Photoemission kink and broadening of fully occupied bands. *Phys. Rev. B*, 85:125137, 2012.

[DM70] P. D. Dernier and M. Marezio. Crystal structure of the low-temperature antiferromagnetic phase of V_2O_3. *Phys. Rev. B*, 2:3771, 1970.

[ETH+90] C. Elsässer, N. Takeuchi, K. M. Ho, C. T. Chan, P. Braun, and M. Fähnle. Relativistic effects on ground state properties of 4d and 5d transition metals. *J. Phys.: Condens. Matter*, 2:4371, 1990.

[FB60] J. M. Foster and S. F. Boys. Canonical configurational interaction procedure. *Rev. Mod. Phys.*, 32:300, 1960.

[FFLR+03] S. Fagot, P. Foury-Leylekian, S. Ravy, J.-P. Pouget, and H. Berger. One-dimensional instability in $BaVS_3$. *Phys. Rev. Lett.*, 90:196401, 2003.

[FGB+00] L. Forró, R. Gaál, H. Berger, P. Fazekas, K. Penc, I. Kézsmárki, and G. Mihály. Pressure induced quantum critical point and non-fermi-liquid behavior in $BaVS_3$. *Phys. Rev. Lett.*, 85:1938, 2000.

[FH80] L. W. Finger and R. M. Hazen. Crystal structure and isothermal compression of Fe_2O_3, Cr_2O_3, and V_2O_3 to 50 kbars. *J. Appl. Phys.*, 51:5362, 1980.

[FH83] C.-L. Fu and K.-M. Ho. First-principles calculation of the equilibrium ground-state properties of transition metals: Applications to Nb and Mo. *Phys. Rev. B*, 28:5480, 1983.

[FP] M. Ferrero and O. Parcollet. TRIQS: a Toolbox for Research in Interacting Quantum Systems.

[FSM+11] H. Fujiwara, A. Sekiyama, S.-K. Mo, J. W. Allen, J. Yamaguchi, G. Funabashi, S. Imada, P. Metcalf, A. Higashiya, M. Yabashi, K. Tamasaku, T. Ishikawa, and S. Suga. Evidence for the constancy of U in the Mott transition of V_2O_3. *Phys. Rev. B*, 84:075117, 2011.

[FW71] A. L. Fetter and J. D. Walecka. *Quantum theory of many-particle systems*. New York, NY: McGraw-Hill, 1971.

[GAC+86] M. Ghedira, M. Anne, J. Chenavas, M. Marezio, and F. Sayetat. Powder neutron diffraction studies for the low-temperature phase transitions in stoichiometric $BaVS_3$. *J. Phys. C: Solid State Phys.*, 19:6489, 1986.

[GBL10] D. Grieger, L. Boehnke, and F. Lechermann. Electronic correlations in vanadium chalcogenides: $BaVSe_3$ versus $BaVS_3$. *J. Phys.: Condens. Matter*, 22:275601, 2010.

[GDT+12] O. Grånäs, I. Di Marco, P. Thunström, L. Nordström, O. Eriksson, T. Björkman, and J. M. Wills. Charge self-consistent dynamical mean-field theory based on the full-potential linear muffin-tin orbital method: methodology and applications. *Comp. Mater. Sci.*, 55:295, 2012.

[GK92] A. Georges and G. Kotliar. Hubbard model in infinite dimensions. *Phys. Rev. B*, 45:6479, 1992.

[GKKR96] A. Georges, G. Kotliar, W. Krauth, and M. J. Rozenberg. Dynamical mean-field theory of strongly correlated fermion systems and the limit of infinite dimensions. *Rev. Mod. Phys.*, 68:13, 1996.

[GM58] V. M. Galitskii and A. B. Migdal. *Sov. Phys. JETP*, 139:96, 1958.

[GML+11] E. Gull, A. J. Millis, A. I. Lichtenstein, A. N. Rubtsov, M. Troyer, and P. Werner. Continuous-time Monte Carlo methods for quantum impurity models. *Rev. Mod. Phys.*, 83:349, 2011.

[GPPL12] D. Grieger, C. Piefke, O. E. Peil, and F. Lechermann. Approaching finite-temperature phase diagrams of strongly correlated materials: a case study for V_2O_3. *Phys. Rev. B*, 86:155121, 2012.

[GVW69] R. A. Gardner, M. Vlasse, and A. Wold. Preparation, properties and crystal structure of barium vanadium sulfide, $BaVS_3$. *Acta Cryst. B*, 25:781, 1969.

[Has70] W. K. Hastings. Monte Carlo sampling methods using Markov chains and their applications. *Biometrika*, 57:97, 1970.

[Hau07] K. Haule. Quantum Monte Carlo impurity solver for cluster dynamical mean-field theory and electronic structure calculations with adjustable cluster base. *Phys. Rev. B*, 75:155113, 2007.

[HK64] P. Hohenberg and W. Kohn. Inhomogeneous electron gas. *Phys. Rev.*, 136:B864, 1964.

[HKE+01] K. Held, G. Keller, V. Eyert, D. Vollhardt, and V. I. Anisimov. Mott-Hubbard metal-insulator transition in paramagnetic V_2O_3: An LDA+DMFT(QMC) study. *Phys. Rev. Lett.*, 86:5345, 2001.

[Hub63] J. Hubbard. Electron correlations in narrow energy bands. *Proc. R. Soc. Lond. A*, 276:238, 1963.

[Hub64a] J. Hubbard. Electron correlations in narrow energy bands. II. The degenerate band case. *Proc. R. Soc. Lond. A*, 277:237, 1964.

[Hub64b] J. Hubbard. Electron correlations in narrow energy bands. III. An improved solution. *Proc. R. Soc. Lond. A*, 281:401, 1964.

[HYK10] K. Haule, C.-H. Yee, and K. Kim. Dynamical mean-field theory within the full-potential methods: Electronic structure of $CeIrIn_5$, $CeCoIn_5$, and $CeRhIn_5$. *Phys. Rev. B*, 81:195107, 2010.

[IOK+02] T. Inami, K. Ohwada, H. Kimura, M. Watanabe, Y. Noda, H. Nakamura, T. Yamasaki, M. Shiga, N. Ikeda, and Y. Murakami. Symmetry breaking in the metal-insulator transition of $BaVS_3$. *Phys. Rev. B*, 66:073108, 2002.

[JO01] J. Joo and V. Oudovenko. Quantum Monte Carlo calculation of the finite temperature Mott-Hubbard transition. *Phys. Rev. B*, 64:193102, 2001.

[Kan63] J. Kanamori. Electron correlation and ferromagnetism of transition metals. *Progress of Theoretical Physics*, 30:275, 1963.

[KJA+79] J. Kelber, A. H. Reis Jr., A. T. Aldred, M. H. Mueller, O. Massenet, G. DePasquali, and G. Stucky. Structural and magnetic properties of one-dimensional barium vanadium triselenide. *J. Solid State Chem.*, 30:357, 1979.

[KP59] L. Kleinman and J. C. Phillips. Crystal potential and energy bands of semiconductors. I. self-consistent calculations for diamond. *Phys. Rev.*, 116:880, 1959.

[KR86] G. Kotliar and A. E. Ruckenstein. New functional integral approach to strongly correlated Fermi systems: The Gutzwiller approximation as a saddle point. *Phys. Rev. Lett.*, 57:1362, 1986.

[KS65] W. Kohn and L. J. Sham. Self-consistent equations including exchange and correlation effects. *Phys. Rev.*, 140:A1133, 1965.

[KSH+06] G. Kotliar, S. Y. Savrasov, K. Haule, V. S. Oudovenko, O. Parcollet, and C. A. Marianetti. Electronic structure calculations with dynamical mean-field theory. *Rev. Mod. Phys.*, 78:865, 2006.

[KUW+10] M. Karolak, G. Ulm, T. Wehling, V. Mazurenko, A. Poteryaev, and A. Lichtenstein. Double counting in LDA + DMFT - The example of NiO. *Journal of Electron Spectroscopy and Related Phenomena*, 181:11, 2010.

[LBG05] F. Lechermann, S. Biermann, and A. Georges. Importance of interorbital charge transfers for the metal-to-insulator transition of $BaVS_3$. *Phys. Rev. Lett.*, 94:166402, 2005.

[LBG07] F. Lechermann, S. Biermann, and A. Georges. Competing itinerant and localized states in strongly correlated $BaVS_3$. *Phys. Rev. B*, 76:085101, 2007.

[Lec03] F. Lechermann. *Ab-initio Betrachtungen zur Elektronenstruktur und Statistischen Mechanik von mehrkomponentigen intermetallischen Systemen am Beispiel Ni-Fe-Al.* PhD thesis, Max-Planck-Institut für Metallforschung Stuttgart, 2003.

[LGKP07] F. Lechermann, A. Georges, G. Kotliar, and O. Parcollet. Rotationally invariant slave-boson formalism and momentum dependence of the quasiparticle weight. *Phys. Rev. B*, 76:155102, 2007.

[LGP+06] F. Lechermann, A. Georges, A. Poteryaev, S. Biermann, M. Posternak, A. Yamasaki, and O. K. Andersen. Dynamical mean-field theory using Wannier functions: A flexible route to electronic structure calculations of strongly correlated materials. *Phys. Rev. B*, 74:125120, 2006.

[LHC79] S. G. Louie, K.-M. Ho, and M. L. Cohen. Self-consistent mixed-basis approach to the electronic structure of solids. *Phys. Rev. B*, 19:1774, 1979.

[LW68] E. H. Lieb and F. Y. Wu. Absence of Mott transition in an exact solution of the short-range, one-band model in one dimension. *Phys. Rev. Lett.*, 20:1445, 1968.

[LW03] Elliott H. Lieb and F.Y. Wu. The one-dimensional Hubbard model: a reminiscence. *Physica A: Statistical Mechanics and its Applications*, 321:1, 2003.

[LWH89] T. Li, P. Wölfle, and P. J. Hirschfeld. Spin-rotation-invariant slave-boson approach to the Hubbard model. *Phys. Rev. B*, 40:6817, 1989.

[Mat76] R. D. Mattuck. *A Guide to Feynman Diagrams in the Many-Body Problem*. New York: McGraw-Hill, 2nd edition, 1976.

[Mat94] L. F. Mattheiss. Band properties of metallic corundum-phase V_2O_3. *J. Phys.: Condens. Matter*, 6:6477, 1994.

[MCP+05] J. Minár, L. Chioncel, A. Perlov, H. Ebert, M. I. Katsnelson, and A. I. Lichtenstein. Multiple-scattering formalism for correlated systems: A KKR-DMFT approach. *Phys. Rev. B*, 72:045125, 2005.

[MDK+03] S.-K. Mo, J. D. Denlinger, H.-D. Kim, J.-H. Park, J. W. Allen, A. Sekiyama, A. Yamasaki, K. Kadono, S. Suga, Y. Saitoh, T. Muro, P. Metcalf, G. Keller, K. Held, V. Eyert, V. I. Anisimov, and D. Vollhardt. Prominent quasiparticle peak in the photoemission spectrum of the metallic phase of V_2O_3. *Phys. Rev. Lett.*, 90:186403, 2003.

[MELFed] B. Meyer, C. Elsässer, F. Lechermann, and M. Fähnle. *FORTRAN 90 Program for Mixed-Basis-Pseudopotential Calculations for Crystals*. Max-Planck-Institut für Metallforschung, Stuttgart, unpublished.

[Mer65] N. D. Mermin. Thermal properties of the inhomogeneous electron gas. *Phys. Rev.*, 137:A1441, 1965.

[Mey98] B. Meyer. *Entwicklung eines neuen ab-initio 'mixed-basis'-Pseudopotentialprogrammes und Untersuchung atomarer Fehlstellen in Molybdän und intermetallischen Verbindungen.* PhD thesis, Universität Stuttgart, 1998.

[MF95] T. Mizokawa and A. Fujimori. Unrestricted Hartree-Fock study of transition-metal oxides: Spin and orbital ordering in perovskite-type lattice. *Phys. Rev. B*, 51:12880, 1995.

[MMR+73] D. B. McWhan, A. Menth, J. P. Remeika, T. M. Rice, and W. F. Brinkman. Metal-insulator transitions in pure and doped V_2O_3. *Phys. Rev. B*, 7:1920, 1973.

[MP76] H. J. Monkhorst and J. D. Pack. Special points for Brillouin-zone integrations. *Phys. Rev. B*, 13:5188, 1976.

[MR70] D. B. McWhan and J. P. Remeika. Metal-insulator transition in $(V_{1-x}Cr_x)_2O_3$. *Phys. Rev. B*, 2:3734, 1970.

[MRR+53] N. Metropolis, A. W. Rosenbluth, M. N. Rosenbluth, A. H. Teller, and E. Teller. Equation of state calculations by fast computing machines. *J. Chem. Phys.*, 21:1087, 1953.

[MRR69] D. B. McWhan, T. M. Rice, and J. B. Remeika. Mott transition in Cr-doped V_2O_3. *Phys. Rev. Lett.*, 23:1384, 1969.

[MRR+71] D. B. McWhan, J. P. Remeika, T. M. Rice, W. F. Brinkman, J. P. Maita, and A. Menth. Electronic specific heat of metallic Ti-doped V_2O_3. *Phys. Rev. Lett.*, 27:941, 1971.

[MV89] W. Metzner and D. Vollhardt. Correlated lattice fermions in $d = \infty$ dimensions. *Phys. Rev. Lett.*, 62:1066, 1989.

[MV97] N. Marzari and D. Vanderbilt. Maximally localized generalized Wannier functions for composite energy bands. *Phys. Rev. B*, 56:12847, 1997.

[MYL+08] A. A. Mostofi, J. R. Yates, Y.-S. Lee, I. Souza, D. Vanderbilt, and N. Marzari. wannier90: A tool for obtaining maximally-localised Wannier functions. *Comp. Phys. Commun.*, 178:685, 2008.

[NO88] J. W. Negele and H. Orland. *Quantum many-particle systems*. Redwood City, Calif.: Addison-Wesley, 1988.

[Nol02] W. Nolting. *Grundkurs Theoretische Physik 7: Viel-Teilchen-Theorie*. Springer-Verlag Berlin Heidelberg, 5th edition, 2002.

[NYG+00] H. Nakamura, T. Yamasaki, S. Giri, H. Imai, M. Shiga, K. Kojima, M. Nishi, K. Kakurai, and N. Metoki. Incommensurate magnetic ordering and spin-liquid-like state in a triangular lattice $BaVS_3$: Neutron diffraction and scattering study. *J. Phys. Soc. Jpn.*, 69:2763, 2000.

[PABG07] L. Pourovskii, B. Amadon, S. Biermann, and A. Georges. Self-consistency over the charge density in dynamical mean-field theory: A linear muffin-tin implementation and some physical implications. *Phys. Rev. B*, 76:235101, 2007.

[PBBS98] H. M. Petrilli, P. E. Blöchl, P. Blaha, and K. Schwarz. Electric-field-gradient calculations using the projector augmented wave method. *Phys. Rev. B*, 57:14690, 1998.

[PBE96] J. P. Perdew, K. Burke, and M. Ernzerhof. Generalized gradient approximation made simple. *Phys. Rev. Lett.*, 77:3865, 1996.

[Pie10] C. Piefke. Rotationally Invariant Slave-Boson Mean-Field formalism (RISB-MF) - extension of the method and application to strongly correlated materials. Diploma thesis, Universität Hamburg, 2010.

[PK59] J. C. Phillips and L. Kleinman. New method for calculating wave functions in crystals and molecules. *Phys. Rev.*, 116:287, 1959.

[PTB+07] A. I. Poteryaev, J. M. Tomczak, S. Biermann, A. Georges, A. I. Lichtenstein, A. N. Rubtsov, T. Saha-Dasgupta, and O. K. Andersen. Enhanced crystal field splitting and orbital selective coherence by strong correlations in V_2O_3. *Phys. Rev. B*, 76:085127, 2007.

[PTT+00] J.-H. Park, L. H. Tjeng, A. Tanaka, J. W. Allen, C. T. Chen, P. Metcalf, J. M. Honig, F. M. F. de Groot, and G. A. Sawatzky. Spin and orbital occupation and phase transitions in V_2O_3. *Phys. Rev. B*, 61:11506, 2000.

[PW92] J. P. Perdew and Y. Wang. Accurate and simple analytic representation of the electron-gas correlation energy. *Phys. Rev. B*, 45:13244, 1992.

[PY89] R. G. Parr and W. Yang. *Density-Functional Theory of Atoms and Molecules*. New York: Oxford University Press, 1989.

[PZ81] J. P. Perdew and A. Zunger. Self-interaction correction to density-functional approximations for many-electron systems. *Phys. Rev. B*, 23:5048, 1981.

[RHR+10] F. Rodolakis, P. Hansmann, J.-P. Rueff, A. Toschi, M. W. Haverkort, G. Sangiovanni, A. Tanaka, T. Saha-Dasgupta, O. K. Andersen, K. Held, M. Sikora, I. Alliot, J.-P. Itié, F. Baudelet, P. Wzietek, P. Metcalf, and

M. Marsi. Inequivalent routes across the Mott transition in V_2O_3 explored by X-ray absorption. *Phys. Rev. Lett.*, 104:047401, 2010.

[RL04] A. N. Rubtsov and A. I. Lichtenstein. Continuous-time quantum Monte-Carlo methods for fermions: Beyond auxiliary field framework. *JETP Lett.*, 80:61, 2004.

[RRS+11] F. Rodolakis, J.-P. Rueff, M. Sikora, I. Alliot, J.-P. Itié, F. Baudelet, S. Ravy, P. Wzietek, P. Hansmann, A. Toschi, M. W. Haverkort, G. Sangiovanni, K. Held, P. Metcalf, and M. Marsi. Evolution of the electronic structure of a Mott system across its phase diagram: X-ray absorption spectroscopy study of $(V_{1-x}Cr_x)_2O_3$. *Phys. Rev. B*, 84:245113, 2011.

[Sch12] S. Schuwalow. *Magnetic adatom structures on semiconductor surfaces in presence of strong electronic correlations.* PhD thesis, Universität Hamburg, 2012.

[SDA94] I. V. Solovyev, P. H. Dederichs, and V. I. Anisimov. Corrected atomic limit in the local-density approximation and the electronic structure of d impurities in Rb. *Phys. Rev. B*, 50:16861, 1994.

[SDAN+09] T. Saha-Dasgupta, O. K. Andersen, J. Nuss, A. I. Poteryaev, A. Georges, and A. I. Lichtenstein. Electronic structure of V_2O_3: Wannier orbitals from LDA-NMTO calculations. *arXiv:0907.2841*, 2009.

[SGCM82] F. Sayetat, M. Ghedira, J. Chenavas, and M. Marezio. Correlations between crystallographic data and physical properties at the 240K and 80K phase transitions in stoichiometric $BaVS_3$. *J. Phys. C: Solid State Phys.*, 15:1627, 1982.

[SHK06] S. Y. Savrasov, K. Haule, and G. Kotliar. Many-body electronic structure of Americium metal. *Phys. Rev. Lett.*, 96:036404, 2006.

[SHT96] I. Solovyev, N. Hamada, and K. Terakura. t_{2g} versus all $3d$ localization in LaMO$_3$ perovskites (M = Ti-Cu): First-principles study. *Phys. Rev. B*, 53:7158, 1996.

[SK04] S. Y. Savrasov and G. Kotliar. Spectral density functionals for electronic structure calculations. *Phys. Rev. B*, 69:245101, 2004.

[SMV01] I. Souza, N. Marzari, and D. Vanderbilt. Maximally localized Wannier functions for entangled energy bands. *Phys. Rev. B*, 65:035109, 2001.

[SPL12] S. Schuwalow, C. Piefke, and F. Lechermann. Impact of the Dzyaloshinskii-Moriya interaction in strongly correlated itinerant systems. *Phys. Rev. B*, 85:205132, 2012.

[SSG+11] H. U. R. Strand, A. Sabashvili, M. Granath, B. Hellsing, and S. Östlund. Dynamical mean field theory phase-space extension and critical properties of the finite temperature Mott transition. *Phys. Rev. B*, 83:205136, 2011.

[TKP+12] C. Taranto, M. Kaltak, N. Parragh, G. Sangiovanni, G. Kresse, A. Toschi, and K. Held. Comparing *GW* + DMFT and LDA + DMFT for the testbed material SrVO$_3$. *arXiv:1211.1324*, 2012.

[Van85] D. Vanderbilt. Optimally smooth norm-conserving pseudopotentials. *Phys. Rev. B*, 32:8412, 1985.

[War60] E. P. Warekois. Low-temperature X-ray diffraction studies on vanadium sesquioxide. *J. Appl. Phys.*, 31:S346, 1960.

[WCdM+06] P. Werner, A. Comanac, L. de' Medici, M. Troyer, and A. J. Millis. Continuous-time solver for quantum impurity models. *Phys. Rev. Lett.*, 97:076405, 2006.

[WM06] P. Werner and A. J. Millis. Hybridization expansion impurity solver: General formulation and application to Kondo lattice and two-orbital models. *Phys. Rev. B*, 74:155107, 2006.

[YGNS01] T. Yamasaki, S. Giri, H. Nakamura, and M. Shiga. Magnetism of $BaVSe_3$. *J. Phys. Soc. Jpn.*, 70:1768, 2001.

[ZZD+12] J.-Z. Zhao, J.-N. Zhuang, X.-Y. Deng, Y. Bi, L.-C. Cai, Z. Fang, and X. Dai. Implementation of LDA+DMFT with the pseudo-potential-plane-wave method. *Chinese Physics B*, 21:057106, 2012.

Danksagungen

Am Schluss der Arbeit möchte ich mich noch bei einigen Personen bedanken, ohne die die Arbeit wahrscheinlich kaum oder gar nicht möglich gewesen wäre und die deshalb nicht unerwähnt bleiben sollen:

- Ich möchte beginnen mit meinem Betreuer Frank Lechermann, der mir jederzeit zu so ziemlich jedem Thema geholfen hat, mir die Möglichkeit zur Promotion gegeben hat (und nicht zuletzt auch die Arbeitsstelle) und schließlich die Begutachtung der Dissertation und Disputation übernommen hat.

- Michael Potthoff danke ich dafür, dass er spontan die Zweitbegutachtung der Dissertation übernommen hat.

- Und Alexander Lichtenstein danke ich dafür, dass er genauso spontan die Zweitbegutachtung der Disputation übernommen hat.

- Michele Fabrizio möchte ich schon einmal dafür danken, dass er mir im Anschluss an meine Promotion eine Stelle angeboten hat und ich so meine begonnene Arbeit fortsetzen kann.

- Spätestens an dieser Stelle stehen meine Kollegen, in keiner ausgezeichneten Reihenfolge. Da wäre Sergej Schuwalow, den ich jederzeit mit jeder noch so dämlichen Frage nerven konnte, und das sogar beim qualitativ hochwertigen Abendessen.

- Lewin Boehnke, der es schafft, über ausnahmslos alles zu meckern, was bei physikalischen Fragestellungen sehr hilfreich sein kann.

- Christoph Piefke, der meistens ausgleichend irgendwo zwischen dem Meckernden und dem Angemeckerten zu finden ist.

- Malte Behrmann, dem diese Diskussion ziemlich egal ist, der aber trotzdem ein sehr angenehmer und netter Bürokollege ist.

- Oleg Peil für die physikalischen Diskussionen, wobei wir meistens festgestellt haben, dass wir vor ein paar Wochen schon beide das gleiche Problem hatten und es unabhängig voneinander auf die gleiche Weise gelöst haben.

- Und noch mal Christoph Piefke, eigentlich noch für so vieles andere, sei es Privatsport, U-Bahnfahrtenunterhaltung oder sehr gute Zusammenarbeit bei allen möglichen Projekten.

- Allen, die die Dissertation ganz oder teilweise Korrektur gelesen haben, vielen Dank dafür. Also insbesondere Sergej Schuwalow für das ausführliche und genaue Korrigieren ganzer Kapitel. Und auch Malte Behrmann, Lewin Boehnke und (jetzt zum dritten mal) Christoph Piefke für die jeweiligen Teile.

- Tim Wehling und Sergej Schuwalow (auch schon zum dritten mal) für die Einblicke in VASP, die zwar nicht direkt in die Dissertation eingeflossen sind, trotzdem sehr hilfreich waren und ohne die ich wohl nur halb so viele Bachelor-Arbeiten hätte betreuen können.

- Oft vergessen, aber dennoch sehr wichtig sind die System-Administratoren, ohne die ich wohl nirgendwo eine Rechnung auch nur hätte starten können. Also Bodo Krause-Kyora vom PHYSnet, Alexander Fitterling vom RRZ, und natürlich auch die Leute vom HLRN und Juropa.

- Nicht zu vergessen sind natürlich meine Eltern, warum, muss ich wohl nicht erst erklären.

- Und zum Schluss einmal pauschal vielen Dank an alle, mit denen ich die letzten fast vier Jahre zusammen gearbeitet habe, auch wenn ich sie hier nicht explizit genannt habe. Es hat mir viel Spaß gemacht!